Gabriel Teófilo Dias Pedrosa

Kondo Effect in Multi-Dirac and Weyl Fermions

Uberlândia, Minas Gerais, Brazil

September 8, 2021

Gabriel Teófilo Dias Pedrosa

Kondo Effect in Multi-Dirac and Weyl Fermions

This is the presentation to the Graduate Program in Physics, at the Federal University of Uberlândia, as a partial requirement to obtain the PhD title in Physics. Major area: Condensed Matter Physics.

Federal University of Uberlândia - UFU

Physics Institute - INFIS

Post-Graduation Program - PPFIS

Supervisor: Prof. Dr. Edson Vernek

Uberlândia, Minas Gerais, Brazil

September 8, 2021

UNIVERSIDADE FEDERAL DE UBERLÂNDIA
Coordenação do Programa de Pós-Graduação em Física
Av. João Naves de Ávila, 2121, Bloco 1A, Sala 213 - Bairro Santa Mônica, Uberlândia-MG, CEP 38400-902
Telefone: (34) 3239-4309 - www.infis.ufu.br - cpgfisica@ufu.br

ATA DE DEFESA - PÓS-GRADUAÇÃO

Programa de Pós-Graduação em:	Física				
Defesa de:	Tese de Doutorado				
Data:	Primeiro de setembro de 2021	Hora de início:	08:46	Hora de encerramento:	13:05
Matrícula do Discente:	11723FIS001				
Nome do Discente:	Gabriel Teófilo Dias Pedrosa				
Título do Trabalho:	*KONDO EFFECT IN MULTI-DIRAC AND WEYL FERMIONS*				
Área de concentração:	Física				
Linha de pesquisa:	Sistemas Fortemente Correlacionados				
Projeto de Pesquisa de vinculação:	Many-body physics in Majorana and Weyl fermion systems (CnPq)				

Reuniu-se por meio de Vídeo conferência a Banca Examinadora, designada pelo Colegiado do Programa de Pós-graduação em Física, assim composta: Professores Doutores: George Balster Martins- INFIS/UFU, Tomé MAuro Schmidt - INFIS/UFU, Antônio Carlos Ferreira Seridônio - UNESP-Ilha Solteira, Diego Paiva Pires - UFMA e Edson Vernek - INFIS/UFU orientador do candidato.

Iniciando os trabalhos o presidente da mesa, Dr. Edson Vernek, apresentou a Comissão Examinadora e o candidato, agradeceu a presença do público, e concedeu ao Discente a palavra para a exposição do seu trabalho. A duração da apresentação do Discente e o tempo de arguição e resposta foram conforme as normas do Programa.

A seguir o senhor(a) presidente concedeu a palavra, pela ordem sucessivamente, aos(às) examinadores(as), que passaram a arguir o(a) candidato(a). Ultimada a arguição, que se desenvolveu dentro dos termos regimentais, a Banca, em sessão secreta, atribuiu o resultado final, considerando o(a) candidato(a):

Aprovado.

Esta defesa faz parte dos requisitos necessários à obtenção do título de Doutor.

O competente diploma será expedido após cumprimento dos demais requisitos, conforme as normas do Programa, a legislação pertinente e a regulamentação interna da UFU.

Nada mais havendo a tratar foram encerrados os trabalhos. Foi lavrada a presente ata que após lida e achada conforme foi assinada pela Banca Examinadora.

Documento assinado eletronicamente por **George Balster Martins**, **Professor(a) do Magistério Superior**, em 01/09/2021, às 15:17, conforme horário oficial de Brasília, com fundamento no art. 6º, § 1º, do Decreto nº 8.539, de 8 de outubro de 2015.

Documento assinado eletronicamente por **ANTONIO CARLOS FERREIRA SERIDONIO**, **Usuário Externo**, em 01/09/2021, às 17:30, conforme horário oficial de Brasília, com fundamento no art. 6º, § 1º, do Decreto nº 8.539, de 8 de outubro de 2015.

Documento assinado eletronicamente por **Edson Vernek**, **Presidente**, em 01/09/2021, às 17:32, conforme horário oficial de Brasília, com fundamento no art. 6º, § 1º, do Decreto nº 8.539, de 8 de outubro de 2015.

Documento assinado eletronicamente por **DIEGO PAIVA PIRES**, **Usuário Externo**, em 01/09/2021, às 18:11, conforme horário oficial de Brasília, com fundamento no art. 6º, § 1º, do Decreto nº 8.539, de 8 de outubro de 2015.

Documento assinado eletronicamente por **Tome Mauro Schmidt**, **Professor(a) do Magistério Superior**, em 02/09/2021, às 08:42, conforme horário oficial de Brasília, com fundamento no art. 6º, § 1º, do Decreto nº 8.539, de 8 de outubro de 2015.

A autenticidade deste documento pode ser conferida no site https://www.sei.ufu.br/sei/controlador_externo.php?acao=documento_conferir&id_orgao_acesso_externo=0, informando o código verificador **3013618** e o código CRC **C67E73E2**.

Referência: Processo nº 23117.058099/2021-60 SEI nº 3013618

Ficha Catalográfica Online do Sistema de Bibliotecas da UFU
com dados informados pelo(a) próprio(a) autor(a).

P372 Pedrosa, Gabriel Teófilo Dias, 1990-
2021 Kondo Effect in multi-Dirac and Weyl Fermions [recurso eletrônico] / Gabriel Teófilo Dias Pedrosa. - 2021.

Orientador: Edson Vernek.
Tese (Doutorado) - Universidade Federal de Uberlândia, Pós-graduação em Física.
Modo de acesso: Internet.
Disponível em: http://doi.org/10.14393/ufu.te.2021.510
Inclui bibliografia.
Inclui ilustrações.

1. Física. I. Vernek, Edson,1973-, (Orient.). II. Universidade Federal de Uberlândia. Pós-graduação em Física. III. Título.

CDU: 53

Bibliotecários responsáveis pela estrutura de acordo com o AACR2:

Gizele Cristine Nunes do Couto - CRB6/2091

I dedicate this work to all those who, without judgment,
support my decisions, no matter how stupid they may seem.

Acknowledgements

First of all, I would like to thank Capes for the scholarship you trusted me with. Without it, it would be impossible for me to accomplish this work, no doubt about it.

I also would like to thank the opportunity Professor Edson Vernek gave me to work beside him, learning how to be a good researcher, learning the state of art of articles and figures in python. I know we talked about aesthetics a lot. You won, I am convinced that beautiful figures and an organized text is an important step to be a good researcher. Not only for that but all your teachings, that extends beyond supervisor-student relation, I am sincerely grateful.

My sincere acknowledgments to a great friend, Dr. Joelson Fernandes, one of the biggest minds I have the privilege to know. I am sure that this work is concluded thanks to his contribution as well. My gratitude for your effort to teach me the Kondo effect and propagators. The valuable lessons I will take with me from our conversations is not about physics only, it is about ethics, morality and the faith in an entity that mysteriously allow you to be a great father and husband, and also a great friend.

I also would like to thank my dear fraternity brothers that are always there for me, creating and discussing nonsense ideas, living together as a family allowing a healthy environment that was crucial for me to write this work. The Saturday afternoon barbecues will be always remembered with a smile in my face.

I would also like to thank my family members, my parents and my two younger brothers. They are always so happy to see me accomplish my goals and cheering for me, motivating me to carry on, no matter how hard life is. It is good to know you have a place to rest your head, a place where you are welcome at any time. I know I can count on each of you guys, thank you very much, I love you all.

A special thanks to the Institute of Physics, PPFIS, and the Federal University of UberLândia, UFU, my Alma Mater. This University is where I consider my second home. The city that welcomed me so well when I arrived in 2009. It was here where I had the honor to live one of the best parts of my life and accomplish my graduation course, my Msc and now the PhD. Thanks to all professors and staff, the guys from the dinning hall and all the mess and yelling we did there. I am sure I will miss the atmosphere of this incredible place. I made good friends and I will take all the knowledge as a gift from the Institute and the University.

At last but not least, a special thanks to the love of my life, the reason for my *will to power*, to quote Nietzsche. She teaches me how to live simple, easy and calm. We talk

about the meaninglessness of life but how we can give meaning when we dream together. If the universe presents us frequencies in order to understand light, she gives me love to see the beauty of colors. Thank you, my darling, for all these years of support, not even once, not even after searching books and philosophies trying to find myself, you gave up on me.

If you gaze long into an abyss,
the abyss will gaze back into you.
–(Friedrich Nietzsche)

Abstract

In the present thesis we study the quantum magnetic impurity inserted in single and multi Dirac and Weyl hosts. We start by reproducing well known cases in literature, such as the Dirac and Weyl semimetals, manipulating the model Hamiltonian to change break symmetries at the emergence of the Kondo effect. By changing symmetries and the chemical potential, we explore various combinations of systems such as Dirac semimetal, Dirac metal, Weyl semimetal and Weyl semimetal for linear ($J = 1$) and non-linear ($J > 1$) behavior in dispersion relation. J is also called topological charge of the system and influence for Kondo to emerge as well as the symmetries we choose to break, such as Time Reversal and Inversion symmetry. We will explore the numerical method that allows us to calculate the Kondo physics properties that emerge in such systems. We also describe the process throughout the work and how we evolved from a simple system to a more complete one. We conclude that for some specific combination of parameters and breaking inversion symmetry of these exotic systems, Kondo physics emerges. We also analyze the behavior of the magnetization in the dispersion relation for Weyl semimetals.

Keywords: Quantum magnetic impurities, Weyl systems, Dirac systems, Kondo effect, NRG.

Resumo

Na presente tese estudamos a impureza magnética quântica inserida em hospedeiros simples e múltiplos de Dirac e Weyl. Começamos reproduzindo casos bem conhecidos na literatura, como os semimetais de Dirac e Weyl, manipulando o modelo hamiltoniano para alterar simetrias de quebra no surgimento do efeito Kondo. Ao alterar as simetrias e o potencial químico, exploramos várias combinações de sistemas, como semimetal de Dirac, metal de Dirac, semimetal de Weyl e semimetal de Weyl para comportamento linear ($J = 1$) e não linear ($J > 1$) na dispersão relação. J também é chamado de carga topológica do sistema e influência para o surgimento de Kondo, bem como as simetrias que escolhemos quebrar, como inversão de tempo e simetria de inversão. Exploraremos o método numérico que nos permite calcular as propriedades físicas de Kondo que surgem em tais sistemas. Também descrevemos o processo ao longo do trabalho e como evoluímos de um sistema simples para um mais completo. Concluímos que para alguma combinação específica de parâmetros e quebra de simetria de inversão desses sistemas exóticos, surge a física Kondo. Analisamos também o comportamento da magnetização na relação de dispersão para semimetais de Weyl.

Palavras-chave: Impurezas magnéticas quânticas, Sistema de Weyl, Sistemas de Dirac, efeito Kondo, NRG.

List of Figures

List of abbreviations and acronyms

SIAM	Single impurity Anderson model
PHS	Particle-hole symmetry
QD	Quantum dot
CB	Coulomb Blockade
TRS	Time-Reversal Symmetry
IS	Inversion Symmetry
WM	Weyl Metal
MWM	Multi-Weyl Metal
WSM	Weyl Semimetal
MWSM	Multi-Weyl Semimetal
DM	Dirac Metal
MDM	Multi Dirac Metal
DSM	Dirac Semimetal
MDSM	Multi-Dirac Semimetal
RG	Renormalization Group
NRG	Numerical Renormalization Group

Contents

1 Introduction

Telling this story is part of the process that brought us here in the first place, and this is how the reader will be part of this journey, in some sort, as we share the narrative of our work. This story started on August 2017, when I entered the ph.D program at the Federal University of Uberlândia, UFU, where I can surely call home. I had just received the Msc degree in Physics at the same institution and I was back in the game for the ph.D. Was it a good choice? I don't know, only time will tell. The Nanoscience group of UFU received me with arms wide open for this new endeavor. My supervisor, at first, would be Professor Dr. Edson Vernek in collaboration with Dr. M. A. Bosseli, who supervised me during my Msc studies, teaching me the art of quantum propagators. However, he could not supervise me for some bureaucratic reasons. This partnership was very productive, I learned a lot from Professor Vernek and his students, mainly Dr. Joelson Fernandes, which deserves very special thanks for being so patient with me, teaching me great things about physics and life in general. At first, we should work on something that both supervisors were familiarized with, however, the new perspectives of science and researches in condensed matter brought us to the so called Weyl solutions to Dirac's Equations, leading to applications that caught our attention and we are going to extensively talk about in this work, a great effort of a prestigious colleagues. For this reason, we were dragged away from the partnership with Boselli, and for that I need to say my sincere apologies to him.

At the same time we were studying the Weyl fermions while Joelson was studying Majorana fermions, also another solution to Dirac's Equations. So we had a good and strong group researching a new class of materials and collaborations between us started strengthening. These solutions for the Dirac's Equations applied to condensed matter were being extensively explored in the scientific community due to a variety of new applications. And this is where we start. We are going to explain the emergence of a quantum mechanical phenomena called Kondo effect when an impurity is embedded in these materials that we call host, which is attracting considerable attention in condensed matter.

It is interesting to know that the very beginning of our study comes from a renowned British physicist, Paul Adrien Maurice Dirac, born in 1902. With 27 years old, he came up with a set of equations, that we will explore in more detail later, that described mathematically new particles in the universe. By bringing up together special relativity and quantum mechanics, he was capable of unifying those two theories and the outcome was a set of equations that describes the physics of anti-particles, a new set of particles in physics. The antimatter, as they are also called, has the same properties as the usual

matter, however the charge has opposite sign and as we are going to see later in this work, this description only applies to half spin particles. For instance, for the electron we have its anti particle, having the same mass but positive charge, also called positron. This new description of reality allowed a better understanding of the universe. It also led new questions to arise like why is there more matter than antimatter in the universe. Moreover, algebraic manipulations of Diracs equations paved the way for new particles like the one we will explore here, the Weyl fermions, in principle they are particles. It is in condensed matter that they emerge as quasiparticles. This study is only possible because a German physicist, Hermann Weyl (1885-1995) proposed, a year after Dirac's work, a different set of solutions for the same set of equations that Dirac described in 1928. He considered the mass of the particle to be zero to solve Dirac's Equations with which he could uncouple them, coming up with massless fermions, also known as weyl fermions. These elementary particles has not yet been found in particle physics, and it is not our intention to discuss them in this context. In fact, we seek to explore their properties in condensed matter physics, where some materials provide us with quasiparticle excitations that behave very much similar to Weyl fermions. There are other interesting outcomes by manipulating the same equations, like Majorana fermions. However, it is not our intention to explore those others because it would take us to different and far away paths (DIRAC; FOWLER, 1928).

To understand where these new physics in the context of Dirac and Weyl fermions come from, we first need to comprehend that topological materials have promoted a colossal excitement in the recent years (ANDO, 2013; KANE; MELE, 2005; BERNEVIG; HUGHES; ZHANG, 2006; FU; KANE, 2007; XIA et al., 2009). The idea behind the characterization of these materials is the use of concepts of topology to classify their electronic band structures. As such, topological phase transition involves changes in some topological index rather than in an order parameter by a broken symmetry (BURKOV; HOOK; BALENTS, 2011; ALEXANDRADINATA; WANG; BERNEVIG, 2016). The best known example of topological materials are topological insulators (BERNEVIG; HUGHES, 2013; HASAN; KANE, 2010; ANDO, 2013) that are bulk insulators, a class of two dimensional materials that exhibit band touching (metallic) edge states that are protected by time reversal symmetry (TRS)(HASAN; KANE, 2010; MOORE, 2010b; KÖNIG et al., 2007; QI; ZHANG, 2011). Analogues of these 2D materials exists in 3D and are generically dubbed Dirac semimetals (YOUNG et al., 2012) found in compounds such as Na_3Bi (LIU et al., 2014) and Cd_3As_2 (BORISENKO et al., 2014; HE et al., 2014). Near the crossing points, the linearly dispersive bands are well described by 3D versions of the Dirac equation. These crossing points are therefore commonly called Dirac nodes and their degeneracy is protected by both TRS and inversion symmetry (IS) of the lattice structure.

An interesting family of topological materials called Weyl semimetals (WSM) emerge from Dirac systems when at least one of the aforementioned symmetries that

protect the degeneracy of the Dirac nodes is broken (ARMITAGE; MELE; VISHWANATH, 2018; ZHONG et al., 2016; FANG et al., 2012; YANG; NAGAOSA, 2014). These systems are recognized by exhibiting peculiar physical properties such as Fermi arcs (WAN et al., 2011; XU et al., 2015a; OJANEN, 2013), chiral anomaly (NANDY et al., 2017; HEIDARI; ASGARI, 2020), affecting drastically their transport properties (KUNDU et al., 2020; LOPEZ; TORRES; NUNEZ, 2018). Later, another variety of WSMs was predicted to exist protected by group symmetry C_n (FANG et al., 2012). These WSMs exhibit topological charge $J > 1$ and appear as a generalization of the first WSM exhibiting $J = 1$, as such they were called multi-Weyl node semimetals (MWSMs) (FANG et al., 2012). This prediction was confirmed for $J = 2$ in $HgCr_2Se_4$ and $SrSi_2$ (XU et al., 2011; FANG et al., 2012; HUANG et al., 2016) while systems in which $J = 3$ have been anticipated to exist in quasi 1D molybdenum monochalcogenide compounds (LIU; ZUNGER, 2017).

With the increasing popularity of these exotic materials and the gain of comprehension on their physical properties, we have witnessed a rising interest in the low-temperature properties of these materials when they host magnetic impurities (PRINCIPI; VIGNALE; ROSSI, 2015; YANAGISAWA, 2015). When an isolated quantum magnetic impurity (also known as Anderson impurity) is inserted in a system of free electrons, such as metals and also these topological materials, their itinerant electrons cooperate to screen the localized moment, a phenomena known as the Kondo effect (ANDERSON, 1961). Although the Kondo effect is more commonly studied in conventional metallic materials (HEWSON, 1993; BULLA; COSTI; PRUSCHKE, 2008), interesting facets of Kondo physics is also found in structured conduction bands near the Fermi level (SILVA et al., 2006; SILVA et al., 2017; GONZALEZ-BUXTON; INGERSENT, 1998; LOGAN; TUCKER; GALPIN, 2014). More recently, the Kondo effect has also been investigated in topological materials such as Dirac and Weyl semimetals in which metallic or pseudo-gap screening regimes have been found (PRINCIPI; VIGNALE; ROSSI, 2015)

In this work we revisit the problem of Kondo screening regimes in the Dirac and Weyl systems (MITCHELL; FRITZ, 2015b), with special attention to the MWSMs, on which a detailed investigation of the Kondo effect is still lacking. We adopt a generic model capable of describing multi-Dirac semimetals (MDSMs) as well MWSMs (LÜ et al., 2019) and employ a numerical renormalization group (NRG) approach (HEWSON, 1993; BULLA; COSTI; PRUSCHKE, 2008) to access the Kondo physics of the system in a systematic manner. Our numerical results show that the Kondo regimes of all MDSM lie on some class of pseudo-gap Kondo effect, in which Kondo screening is possible only at the particle-hole asymmetric situation. In contrast, in IS broken, which can be performed applying strains in host's crystalline structure, MWSM, Kondo screening is possible even in particle-hole symmetric condition. Moreover, rich Kondo regimes emerge as a result of the interplay between the chemical potential μ and inversion symmetry parameter Q_0. We also find that in MWSMs with broken TRS the Kondo screening is affected, albeit weakly,

by magnetic polarization induced at the impurity via hybridization function.

1.1 Motivation

In order to understand what makes us do a certain work like the one we present here, leads us to an ethics problem. There are a lot of motivations for this work, some of them are not the ones intended to be mentioned because we are expected to convince that this writings are useful. Usefulness, what an awkward concept. To prove that the work is worth doing can cause trouble once it is subject, however we can give you some examples of how relevant this work is. In terms of personal motivation, we have a bunch of explanations that brought us here, like something we find interesting studying by some other influence, for example our colleagues or supervisor. Or we just want to look for a subject that is being explored extensively, therefore, increasing the chance of having a higher number of publications that will enhance our career, giving us prestige. Are we looking for recognition, acceptance or maybe we want to be remembered by something we do? Other times we just need a motivation to wake up in the morning and get out of bed.

Without further ado, since it is not a philosophical discussion, we need to convince you, reader, that this work has a major purpose and is worth publishing. To do so we come up with some novel researches and developments in this area of science to convince you, we are going to tell you about the topological properties of these materials and how these properties are innovating in science and leads the scientific community to new discoveries. But before that, however, we have to explain what topology is and then we can understand a little about topological materials and how they are giving us such new possibilities in science.

Topology comes from the Greeks and it means the knowledge of place, region or space. It is a part of science and mathematics that studies the conformation of algebraic and/or geometric spaces. It is a complex and sometimes vague concept, feeling that talking about topology is to say a lot and understand almost nothing. It is not our intention to explain in detail what topology is, however, we have to give you the possibility to comprehend what is being studied in these writings. The seminal studies of Kosterlitz e Thouless (KOSTERLITZ; THOULESS, 2001; THOULESS et al., 1982) and Haldane (HALDANE, 1983) about forty years ago made it possible to classify and study systematically the states of matter based on their topological characteristics (see Ref.(QI; ZHANG, 2011; MOORE, 2010a; FU; KANE; MELE, 2007; FU; KANE, 2007; TOKURA; YASUDA; TSUKAZAKI, 2019; SCHNYDER et al., 2008)). Given the revolutionary implications that the work of these three physicists provided concerning this new type of materials, the so called topological materials, they were awarded with the Nobel Prize in physics of 2016. More recently, we are testifying an increasing interest in these materials and

other properties that emerge from this concept, such as Topological Insulators (TI) and Topological Superconductors (TS), to which topological concepts used to explain these phenomena are justify the term topological phases of matter (YAN; FELSER, 2017; BERNEVIG, 2013). There are plenty of reasons for the interest in these materials. From a theoretical perspective, for example, it is a great opportunity to test the abstract properties of these topological materials in realistic systems. From a practical perspective, the idea of protected topological systems provides us with new possibilities to develop devices for technological applications like spintronics and quantum computation, just to name a few (HE et al., 2021; KUREBAYASHI; NOMURA, 2016; ZHAO et al., 2020; SUN et al., 2016; CHEN; NAZAROV, 2020; YANG, 2016; ŠMEJKAL; JUNGWIRTH; SINOVA, 2017; LI et al., 2018).

The main physical characteristics in topological materials are the bulk, surface and edge states in 3D, 2D and 1D systems, respectively. These states are topologically protected by some sort of symmetry presented in the material under consideration. For example, in traditional TI materials, Time-Reversal Symmetry (TRS) protects those states. On the other hand, the TS edge states are protected by particle-hole (PH) symmetry of Bogoliubov-de Genes Hamiltonian, usually employed to describe these materials. A very interesting property presented in TS materials is the Majorana quasiparticle behavior, a Majorana bound state (MBS) on its edges [commonly called Majorana fermions (MF) (READ; GREEN, 2000; FRANZ, 2010; ALICEA, 2010)]. Like Weyl proposed a solution for Dirac's equation so did Ettore Majorana in 1937 (MAJORANA, 1937). MBS are quasiparticles excitations that correspond to its own antiparticle, occuring always in pairs. A topological superconductor wire, for example, is predicted to exhibit a MBS on its edges. Even more interesting, is the fact that spatially separated MBS can be combined into a conventional non-local fermion. This uncommon non-locality property has great potential in applications in topological quantum computation (PACHOS; SIMON, 2014; SARMA; FREEDMAN; NAYAK, 2015; AKHMEROV, 2010; LAFLAMME et al., 2014; OREG; REFAEL; OPPEN, 2010; NAYAK et al., 2008; LEE et al., 2012).

Let us refocus our attention to the Weyl Semimetals (WSM). Unlike TI, we believe these materials were not explored extensively so far and have promising innovations, becoming a field of interest in the scientific community. The WSMs present a non-trivial topological phase that extends beyond TI. While TI preserve TRS we can break this symmetry in WSMs. We can picture these materials being TI exhibiting surface states with exotic properties. In fact, WSMs are described by Dirac Hamiltonians, exhibiting either broken TRS or broken IS, or both. Known as quasi-particles, these systems exhibits this emergent behavior due to weak interactions that stimulates its appearance (WENG et al., 2015; YANG et al., 2017; XU et al., 2015a; LV et al., 2015; LÜ et al., 2019).

The recent interest in WSMs and their technological applications is motivating

scientific investigations of these materials in a low-energy regime in the presence of magnetic impurities for 3D systems. It has been shown that, when a magnetic impurity is attached to a WSM surface, the Kondo effect (KONDO, 1964a) takes place for these materials (PRINCIPI; VIGNALE; ROSSI, 2015; YANAGISAWA, 2015; MA et al., 2018). In fact, it was shown by Mitchell and Fritz (MITCHELL; FRITZ, 2015a) that different aspects of Kondo effect can be obtained depending on which type of symmetry is being broken, controlling the parameters in the Dirac-like Hamiltonian that describes the model. In this work, we are going to explore a theoretical model capable of describing the Kondo effect in Weyl semimetals with either broken Time-reversal and/or broken Iversion symetry. Despite the recent developments of scientific research in this field, many questions remain to be answered, for example how the Kondo effect depends on the model Hamiltonian, or if there is quantum phase transitions in these kind of systems. We will provide a better understanding of these problems as we progress in the work presented here.

Along this work, we aim at answering these questions and propose future studies. In particular, we are also interested in non-linear anisotropic behavior in the dispersion relation of these materials, in the context of the so called Multi Weyl Semimetals (MWSM). There is a rich variety of combinations of symmetries with the parameters our model provides. For example, we can have either TRS and/or IS combining with metal and/or semimetal case if we change the chemical potential. Also, we have single, 2-Multi or 3-Multi Weyl and the Dirac cases as well.

As a result of these four years of PhD, we were able to develop a profound understanding of the referred topics of this work, more precisely, the Kondo screening of the impurity hosted in multi-Weyl and massless Multi-Dirac systems (PEDROSA; SILVA; VERNEK, 2021). The results presented here are a more detailed presentation of the article alongside with some other results that are not included in the publication, as well as the journey that brought us here. To deserve our effort in developing such study and attract the reader's attention, it is good to emphasize that the contribution of the present work to the scientific community is the description of Kondo physics in a multi-Weyl system by manipulating the topological symmetries of it. And we will prove that it is possible to have Kondo physics even for no chemical potential in Weyl and multi-Weyl systems.

To accomplish our goal, in the next chapter we derive the famous Dirac's Equations 2.1 followed by Weyl's alternative solution in Chapter 2.2. Chapter 3, we present a brief study of the Kondo effect due to impurities 3.1 and quantum dots 3.2. The next chapter is the description and understanding of Weyl 4.1 and Multi-Weyl 4.2 systems, followed by the model description in 4.3. In sequence, we give a description of the steps to perform the calculations that evolved from RG 5.1 to a numerical approach extensively used in this work, NRG 5.2. Finally, the discussion of the results will be presented in Chapter 6.

2 From Dirac to Weyl

In order to understand the strategy through which Hermann Weyl developed his set of equations and came out with massless electrons, it is instructive to derive his equations explicitly. To give a better explanation, we are going to explain each and every step along this process.

Paul Adrien Maurice Dirac (1902-1984) in a brilliant effort to unify the theories of special relativity and quantum mechanics, came up with a set of equations that brought them together. Those equations were proposed in 1928, which became the well known Dirac's Equations, led to the discovery of antimatter. Such description was applied for usual 1/2-spin particles with mass, like electrons. However, this new discovery described the same particles but with opposite charge, also known as the antiparticles. Therefore, the electron's antiparticle is the positron, a spin half particle with positive charge and same mass. Similarly, the proton has a spin half particle with the same mass but with negative charge, which is called the antiproton. This new group of particles allowed us a new description of reality and new questions arise from it. One example is why there is more matter than antimatter in our observable universe? Sometimes I wonder, myself, why do we ask such questions and what is the need to answer so many questions? Is it going to change our lives to know why there is more matter than antimatter in our universe? Anyways, this exotic attempt to understand reality was also found by Carl D. Anderson. Anderson provided major contributions for particle physics when he detected unexpected particle tracks in a cloud chamber, something like a cathodic tube, while he was studying the cosmic background radiation. He confirmed that it was particles with the same mass of electrons but with opposite charge. It was published in 1932 (ANDERSON, 1933) as the first experimental validation of Dirac's theoretical prediction of such particles.

2.1 A derivation of Dirac's Equation

We start with the basic quantum mechanical Hamiltonian describing a free particle

$$\hat{\mathcal{H}} = \frac{\hat{p} \cdot \hat{p}}{2m}, \tag{2.1}$$

in which we define $\hat{p}$ as a three dimensional quantum momentum operator as

$$\hat{p} = -i\hbar\vec{\nabla}. \tag{2.2}$$

As such, the Hamiltonian (2.1) describes just the kinetic energy of the particle.

For 1/2 spin particles in the presence of magnetic field, we have

$$\hat{\mathcal{H}}_{spin} = -\left(\frac{e\hbar}{2mc}\right)\vec{\sigma}.\vec{B}. \tag{2.3}$$

The Pauli matrices form a vector $\vec{\sigma}$, that can be written as

$$\vec{\sigma} = \sigma_x\hat{x} + \sigma_y\hat{y} + \sigma_z\hat{z}, \tag{2.4}$$

where $\hat{x}$, $\hat{y}$ and $\hat{z}$ are the canonical base of $\mathbb{R}^3$, and

$$\sigma_x = \begin{pmatrix} 1 & 0 \\ 0 & 1 \end{pmatrix}; \sigma_y = \begin{pmatrix} 0 & -i \\ i & 0 \end{pmatrix}; \sigma_z = \begin{pmatrix} 1 & 0 \\ 0 & -1 \end{pmatrix}$$

are the Pauli matrices.

From Maxwell's Equations, the magnetic field can be written as

$$\vec{B} = \vec{\nabla} \times \vec{A} \tag{2.5}$$

where $\vec{A}$ is the electromagnetic vector potential.

We introduce a substitution on the quantum momentum operator, that was used by Dirac, in order to establish a relation between quantum mechanics and electromagnetism. The procedure is called the minimum coupling and is introduced even in classical electrodynamics. This is done by replacing the momentum operator with

$$\hat{p} \to \hat{p} - \frac{e\vec{A}}{c}. \tag{2.6}$$

From this rearrangement of the momentum operator, we can rewrite the Hamiltonian as

$$\hat{\mathcal{H}} = \frac{1}{2m}(\vec{\sigma}\cdot\hat{p})(\vec{\sigma}\cdot\hat{p}). \tag{2.7}$$

We should emphasize that this is a non-trivial way of writing the Hamiltonian. Substituting Eq. (2.6) into Eq. (2.7), we can write the Hamiltonian as follows

$$\hat{\mathcal{H}} = \frac{1}{2m}\left[\vec{\sigma}\cdot\left(\hat{p} - \frac{e\vec{A}}{c}\right)\right]\left[\vec{\sigma}\cdot\left(\hat{p} - \frac{e\vec{A}}{c}\right)\right]. \tag{2.8}$$

Using the demonstration in Appendix A, we have the following relation

$$(\vec{\sigma}\cdot\vec{a})(\vec{\sigma}\cdot\vec{b}) = (\vec{a}\cdot\vec{b})\hat{\mathbb{1}} + i\vec{\sigma}\cdot(\vec{a}\times\vec{b}). \tag{2.9}$$

When we apply Eq. (2.9) in Eq. (2.8), we have a simplification of this Hamiltonian. So, Eq. (2.8) can be rewritten as

$$\left[\vec{\sigma}\cdot\left(\hat{p}-\frac{e\vec{A}}{c}\right)\right]\left[\vec{\sigma}\cdot\left(\hat{p}-\frac{e\vec{A}}{c}\right)\right] = \left(\hat{p}-\frac{e\vec{A}}{c}\right)\cdot\left(\hat{p}-\frac{e\vec{A}}{c}\right) \tag{2.10}$$

$$+i\vec{\sigma}\cdot\left[\left(\hat{p}-\frac{e\vec{A}}{c}\right)\times\left(\hat{p}-\frac{e\vec{A}}{c}\right)\right] =$$

$$=\left(\hat{p}-\frac{e\vec{A}}{c}\right)^2+i\vec{\sigma}\cdot\left[\left(\hat{p}-\frac{e\vec{A}}{c}\right)\times\left(\hat{p}-\frac{e\vec{A}}{c}\right)\right] \tag{2.11}$$

From basic vector properties we can write[1]

$$\hat{p}\times\hat{p}=0 \tag{2.12}$$

and

$$\vec{A}\times\vec{A}=0. \tag{2.13}$$

Therefore, the Hamiltonian can be greatly simplified as follows

$$\hat{\mathcal{H}}=\frac{1}{2m}\left(\hat{p}-\frac{e\vec{A}}{c}\right)^2+\frac{i}{2m}\vec{\sigma}\cdot\left(-\frac{e}{c}\hat{p}\times\vec{A}-\frac{e}{c}\vec{A}\times\hat{p}\right) \tag{2.14}$$

or

$$\hat{\mathcal{H}}=\frac{1}{2m}\left(\hat{p}-\frac{e\vec{A}}{c}\right)^2-\frac{ie}{2mc}\vec{\sigma}\cdot\left(\hat{p}\times\vec{A}+\vec{A}\times\vec{p}\right). \tag{2.15}$$

To further simplify this expression, let us manipulate the left hand side of the equation above. We have the relation

$$\begin{aligned}
(\hat{p}\times\vec{A})\,\phi &= (-i\hbar\vec{\nabla}\times\vec{A})\,\phi \\
&= -i\hbar(\vec{\nabla}\times\vec{A})\,\phi \\
&= -i\hbar\left[\vec{\nabla}\times\left(\vec{A}\phi\right)\right] \\
&= -i\hbar\left[\left(\vec{\nabla}\phi\right)\times\vec{A}+\phi\left(\vec{\nabla}\times\vec{A}\right)\right] \\
&= -i\hbar\left[-\vec{A}\times\left(\vec{\nabla}\phi\right)+\phi\vec{B}\right] \\
&= -\vec{A}\times\left(-i\hbar\vec{\nabla}\phi\right)-i\hbar\vec{B}\phi \\
&= \left(-\vec{A}\times\hat{p}-i\hbar\vec{B}\right)\phi.
\end{aligned} \tag{2.16}$$

With this we can write

$$\hat{p}\times\vec{A}=-\vec{A}\times\hat{p}-i\hbar\vec{B}, \tag{2.17}$$

[1] For further proof of the statements about vector properties, follow the notes in Appendix A.

as in a more viable form, we have

$$\boxed{(\hat{p}\times\vec{A})+(\vec{A}\times\hat{p})=-i\hbar\vec{B}}. \tag{2.18}$$

Therefore,

$$\boxed{\hat{\mathcal{H}}=\frac{1}{2m}\left(\hat{p}-\frac{e\vec{A}}{c}\right)^2-\frac{e\hbar}{2mc}\vec{\sigma}\cdot\vec{B}}\rightarrow \text{ Coming from Minimal Coupling.} \tag{2.19}$$

Now, we will bring Special relativity to take part in the Hamiltonian in order to reach Dirac's Equations. The relativistic energy is given by

$$E^2 = p^2c^2+m^2c^4. \tag{2.20}$$

Dividing Eq. (2.20) by c^2, we have

$$\frac{E^2}{c^2} = p^2+m^2c^2$$

or we can simplify a little more to get

$$\frac{E^2}{c^2}-p^2=(mc)^2$$

which can be written as

$$\left[\left(\frac{E}{c}\right)^2-p^2\right] = \left[\left(\frac{E}{c}+p\right)\left(\frac{E}{c}-p\right)\right]=(mc)^2, \tag{2.21}$$

or simply

$$\left(\frac{E}{c}-p\right)\left(\frac{E}{c}+p\right)=(mc)^2. \tag{2.22}$$

We know from the Time-Dependent Schrödinger Equation (TDSE) that

$$i\hbar\frac{\partial}{\partial t}\psi=\hat{\mathcal{H}}\psi=E\psi. \tag{2.23}$$

If we observe the relation above, we can notice that E can be written as

$$E\rightarrow i\hbar\frac{\partial}{\partial t} \tag{2.24}$$

and using the trick introduced by Dirac

$$\hat{p}\rightarrow\vec{\sigma}\cdot\hat{p} \tag{2.25}$$

and substituting in Eq. (2.22)

$$\hat{p}\rightarrow\vec{\sigma}\cdot\left(-i\hbar\vec{\nabla}\right). \tag{2.26}$$

Therefore,

$$\left[\frac{i\hbar}{c}\frac{\partial}{\partial t}+\vec{\sigma}\cdot\left(i\hbar\vec{\nabla}\right)\right]\left[\frac{i\hbar}{c}\frac{\partial}{\partial t}-\vec{\sigma}\cdot\left(i\hbar\vec{\nabla}\right)\right]\phi=(mc)^2\,\phi. \tag{2.27}$$

We also have

$$\left\{i\hbar\left[\frac{\partial}{\partial(ct)}+\vec{\sigma}\cdot\vec{\nabla}\right]i\hbar\left[\frac{\partial}{\partial(ct)}-\vec{\sigma}\cdot\vec{\nabla}\right]\right\}\phi=(mc)^2\phi, \tag{2.28}$$

such that by setting $x_0=ct$, we can write

$$\left(\frac{\partial}{\partial x_0}+\vec{\sigma}\cdot\vec{\nabla}\right)\left(\frac{\partial}{\partial x_0}-\vec{\sigma}\cdot\vec{\nabla}\right)\phi=\left(\frac{mc}{i\hbar}\right)^2\phi. \tag{2.29}$$

Making some simplifications through a substitution for a constant to help us easily carry some terms, we write $\frac{mc}{i\hbar}=g$, [2] we have

$$\left(\frac{\partial}{\partial x_0}+\vec{\sigma}\cdot\vec{\nabla}\right)\left(\frac{\partial}{\partial x_0}-\vec{\sigma}\cdot\vec{\nabla}\right)\phi=g^2\phi. \tag{2.30}$$

We can now introduce two new variables $\phi^{(R)}$ and $\phi^{(L)}$ as,

$$\begin{cases}\phi^{(R)}=\frac{1}{g}\left(\frac{\partial}{\partial x_0}-\vec{\sigma}\cdot\vec{\nabla}\right)\phi^{(L)}\\ \phi^{(L)}=\frac{1}{g}\left(\frac{\partial}{\partial x_0}+\vec{\sigma}\cdot\vec{\nabla}\right)\phi^{(R)}.\end{cases} \tag{2.31}$$

Note that,

$$\phi^{(R)}=\frac{1}{g^2}\left(\frac{\partial}{\partial x_0}-\vec{\sigma}\cdot\vec{\nabla}\right)\left(\frac{\partial}{\partial x_0}+\vec{\sigma}\cdot\vec{\nabla}\right)\phi^{(R)}. \tag{2.32}$$

If we transform $\phi^{(R)}\to\phi$, we recover Eq. (2.30). Therefore, after some algebraic manipulations, we can write

$$\begin{cases}g\phi^{(L)}=\frac{\partial}{\partial x_0}\phi^{(R)}+\vec{\sigma}\cdot\vec{\nabla}\phi^{(R)}\\ g\phi^{(R)}=\frac{\partial}{\partial x_0}\phi^{(L)}-\vec{\sigma}\cdot\vec{\nabla}\phi^{(L)}\end{cases} \tag{2.33}$$

Upon summing and subtracting the coupled equations above, we can obtain, respectively,

$$\frac{\partial}{\partial x_0}\left[\phi^{(R)}+\phi^{(L)}\right]+\vec{\sigma}\cdot\vec{\nabla}\left[\phi^{(R)}-\phi^{(L)}\right]=g\left[\phi^{(R)}+\phi^{(L)}\right] \tag{2.34}$$

and

$$-\frac{\partial}{\partial x_0}\left[\phi^{(R)}-\phi^{(L)}\right]-\vec{\sigma}\cdot\vec{\nabla}\left[\phi^{(R)}+\phi^{(L)}\right]=g\left[\phi^{(R)}-\phi^{(L)}\right]. \tag{2.35}$$

We can write the wave functions in terms of a spinor as

$$\psi=\begin{pmatrix}\phi^R+\phi^L\\ \phi^R-\phi^L\end{pmatrix}=\begin{pmatrix}\psi_A\\ \psi_B\end{pmatrix}. \tag{2.36}$$

[2] Note that the dimension of g can be expressed as $[g]=\frac{Kg\cdot m}{s^2}\cdot\frac{1}{J}=\frac{1}{m}$.

Now, we rewrite Eq. (2.34) and Eq. (2.35) in terms of ψ_A and ψ_B, as

$$\begin{cases} \frac{\partial}{\partial x_0}\psi_A + \vec{\sigma}\cdot\vec{\nabla}\psi_B = g\psi_A \\ -\frac{\partial}{\partial x_0}\psi_B - \vec{\sigma}\cdot\vec{\nabla}\psi_A = g\psi_B. \end{cases} \tag{2.37}$$

In a matrix form, we have

$$\begin{pmatrix} \frac{\partial}{\partial x_0}\mathbb{1} & \vec{\sigma}\cdot\vec{\nabla} \\ -\vec{\sigma}\cdot\vec{\nabla} & -\frac{\partial}{\partial x_0}\mathbb{1} \end{pmatrix} \begin{pmatrix} \psi_A \\ \psi_B \end{pmatrix} = g \begin{pmatrix} \psi_A \\ \psi_B \end{pmatrix} \tag{2.38}$$

We will manipulate these matrices in order to write them in terms of the momentum operator. First, recalling that $g = \frac{mc}{i\hbar}$, we obtain

$$-i\hbar \begin{pmatrix} -\frac{\partial}{\partial x_0}\mathbb{1} & -\vec{\sigma}\cdot\vec{\nabla} \\ \vec{\sigma}\cdot\vec{\nabla} & \frac{\partial}{\partial x_0}\mathbb{1} \end{pmatrix} \begin{pmatrix} \psi_A \\ \psi_B \end{pmatrix} = mc \begin{pmatrix} \psi_A \\ \psi_B \end{pmatrix} \tag{2.39}$$

$$\begin{pmatrix} -i\hbar\frac{\partial}{\partial x_0}\mathbb{1} & -i\hbar\vec{\sigma}\cdot\vec{\nabla} \\ i\hbar\vec{\sigma}\cdot\vec{\nabla} & i\hbar\frac{\partial}{\partial x_0}\mathbb{1} \end{pmatrix} \begin{pmatrix} \psi_A \\ \psi_B \end{pmatrix} = -mc \begin{pmatrix} \psi_A \\ \psi_B \end{pmatrix} \tag{2.40}$$

Since $x_0 = ct$, we introduce $x_4 = ict$ to write

$$\frac{1}{\hbar} \begin{pmatrix} \hbar\frac{\partial}{\partial x_4}\mathbb{1} & -i\hbar\vec{\sigma}\cdot\vec{\nabla} \\ i\hbar\vec{\sigma}\cdot\vec{\nabla} & -\hbar\frac{\partial}{\partial x_4}\mathbb{1} \end{pmatrix} \begin{pmatrix} \psi_A \\ \psi_B \end{pmatrix} = \frac{-mc}{\hbar} \begin{pmatrix} \psi_A \\ \psi_B \end{pmatrix}. \tag{2.41}$$

Manipulating the matrix above, we can write

$$\begin{pmatrix} \frac{\partial}{\partial x_4}\mathbb{1} & -i\vec{\sigma}\cdot\vec{\nabla} \\ i\vec{\sigma}\cdot\vec{\nabla} & -\frac{\partial}{\partial x_4}\mathbb{1} \end{pmatrix} = \begin{pmatrix} \mathbb{1} & 0 \\ 0 & \mathbb{1} \end{pmatrix} \frac{\partial}{\partial x_4} + \begin{pmatrix} 0 & -i\sigma_k \\ i\sigma_k & 0 \end{pmatrix} \frac{\partial}{\partial x_k}$$

where $k = x$, y or z.

$$\begin{aligned} \begin{pmatrix} \frac{\partial}{\partial x_4}\mathbb{1} & -i\vec{\sigma}\cdot\vec{\nabla} \\ i\vec{\sigma}\cdot\vec{\nabla} & -\frac{\partial}{\partial x_4}\mathbb{1} \end{pmatrix} &= \sigma_z \otimes \sigma_0 \frac{\partial}{\partial x_4} + \sigma_y \otimes \sigma_k \frac{\partial}{\partial x_k} \\ &= \sigma_y \otimes \sigma_k \frac{\partial}{\partial x_k} + \sigma_z \otimes \sigma_0 \frac{\partial}{\partial x_4} \end{aligned} \tag{2.42}$$

Here $x \to 1$, $y \to 2$ and $z \to 3$, such that $k = 1, 2, 3$. We can use μ to write a more general subscript that contains the three dimensional (3D) space coordinates and time as a fourth coordinate, such that $\mu = 1, 2, 3, 4$. Making use of the following matrices

$$\gamma_k = \sigma_y \otimes \sigma_k = \begin{pmatrix} 0 & -i\sigma_k \\ i\sigma_k & 0 \end{pmatrix} \tag{2.43}$$

and,

$$\gamma_4 = \sigma_z \otimes \sigma_0 \ = \begin{pmatrix} \mathbb{1} & 0 \\ 0 & -\mathbb{1} \end{pmatrix}. \tag{2.44}$$

With this we can write

$$\gamma_\mu \frac{\partial}{\partial x_\mu}\psi = \frac{-mc}{\hbar}\psi \tag{2.45}$$

or simply,

$$\boxed{\left(\gamma_\mu \frac{\partial}{\partial x_\mu} + \frac{mc}{\hbar}\right)\psi = 0}. \tag{2.46}$$

Eq. (2.46) is the famous Dirac Equation, where

$$\gamma_k = \sigma_y \otimes \sigma_k. \tag{2.47}$$

This is the matrix form that synthesizes Dirac's solution into one single equation. Since it is a combination of quantum mechanics with special relativity, we have a four dimensional tensor, the three first dimensions are spatial ones and the fourth is temporal.

2.2 Weyl's Solution

In 1929, one year after Dirac's work, the German physicist Hermann Weyl published a different description for Dirac's Equation, proposing a new set of solutions for the same problem, leading to a new set of particles (WEYL, 1929). As we are about to see, he proposed that the rest mass of the particles are zero. As they knew at that time, charged particles, like electrons for example, are massive, while only bosonic particles, like photons which carries no charge, are known to be massless. So, they first divided particles into two groups with distinct properties, fermions and bosons. They have distinct properties. Fermions have charge, a finite mass and half-spin. Bosons, on the other hand are massless, have no charge and integer spin. Weyl was proposing a new class of particles, something totally different from what they already knew at that time. However, we know that mathematical solutions do not necessarily imply physical reality. In other words, theoretical predictions need experiments that prove the hypothesis and so far, there is no such experiment proving the existence of Weyl fermions. Indeed, these exotic massless particles were never found in high energy physics. Interestingly, Weyl fermions can appear as emergent quasiparticles in low energy physics of topological systems in condensed matter, a very recent field of research for extraordinary discoveries and potential applications on spintronics, magnetoresistance, transport phenomena and optics, to name a few (JIAN; YAO, 2015; ŠMEJKAL; JUNGWIRTH; SINOVA, 2017; YANG; LU; RAN, 2011; SUSHKOV et al., 2015; LANDSTEINER, 2014; LIANG et al., 2018).

Based on Weyl's solutions for Dirac's Equations, we have the following description. Dirac's Hamiltonian is given as follows

$$\left(\hbar\gamma_\mu\frac{\partial}{\partial x_\mu}+mc\right)\phi=0. \tag{2.48}$$

Weyl applied a symmetric condition to the equations as he noticed that there are some special cases in odd spatial dimension (WEYL, 1929; ARMITAGE; MELE; VISHWANATH, 2017). In the following, we use the matrix relations Eq. (2.43) and Eq. (2.44), we will manipulate to show Weyl's solutions. So, we have

$$\begin{pmatrix} \left(\hbar\frac{\partial}{\partial x_4}+mc\right)\mathbb{1} & -i\hbar\sigma_k\frac{\partial}{\partial x_k} \\ i\hbar\sigma_k\frac{\partial}{\partial x_k} & \left(-\hbar\frac{\partial}{\partial x_4}+mc\right)\mathbb{1} \end{pmatrix}\begin{pmatrix}\psi_A\\ \psi_B\end{pmatrix}=\begin{pmatrix}0\\0\end{pmatrix} \tag{2.49}$$

$$\begin{cases} \left(\hbar\frac{\partial}{\partial x_4}+mc\right)\psi_A-i\hbar\,\sigma_k\frac{\partial}{\partial x_k}\psi_B=0 \\ i\hbar\sigma_k\frac{\partial}{\partial x_k}\psi_A+\left(-\hbar\frac{\partial}{\partial x_4}+mc\right)\psi_B=0 \end{cases} \tag{2.50}$$

$$\begin{cases} \hbar\frac{\partial}{\partial x_4}\psi_A+mc\,\psi_A-i\hbar\,\sigma_k\frac{\partial}{\partial x_k}\psi_B=0 \\ i\hbar\sigma_k\frac{\partial}{\partial x_k}\psi_A-\hbar\frac{\partial}{\partial x_4}\psi_B+mc\psi_B=0. \end{cases} \tag{2.51}$$

Adding and subtracting the terms in Eq. (2.51), we have

$$\hbar\frac{\partial}{\partial x_4}\left(\psi_A-\psi_B\right)+i\hbar\,\sigma_k\frac{\partial}{\partial x_k}\left(\psi_A-\psi_B\right)+mc\,\left(\psi_A+\psi_B\right)=0 \tag{2.52}$$

and

$$\hbar\frac{\partial}{\partial x_4}\left(\psi_A+\psi_B\right)-i\hbar\,\sigma_k\frac{\partial}{\partial x_k}\left(\psi_A+\psi_B\right)+mc\,\left(\psi_A-\psi_B\right)=0. \tag{2.53}$$

Let us write $\psi_\pm=\frac{1}{\sqrt{2}}\left(\psi_A\pm\psi_B\right)$, so

$$\begin{cases} \hbar\frac{\partial}{\partial x_4}\psi_-+i\hbar\sigma_k\frac{\partial}{\partial x_k}\psi_-+mc\psi_+=0 \\ \hbar\frac{\partial}{\partial x_4}\psi_+-i\hbar\sigma_k\frac{\partial}{\partial x_k}\psi_++mc\psi_-=0 \end{cases} \tag{2.54}$$

or

$$\begin{cases} \hbar\left(\frac{\partial}{\partial x_4}\mathbb{1}-i\sigma_k\frac{\partial}{\partial x_k}\right)\psi_++mc\psi_-=0 \\ mc\psi_++\hbar\left(\frac{\partial}{\partial x_4}\mathbb{1}+i\sigma_k\frac{\partial}{\partial x_k}\right)\psi_-=0. \end{cases} \tag{2.55}$$

In its matrix form, we have

$$\begin{pmatrix} \frac{\partial}{\partial x_4}\mathbb{1}-i\sigma_k\frac{\partial}{\partial x_k} & \frac{mc}{\hbar} \\ \frac{mc}{\hbar} & \frac{\partial}{\partial x_4}\mathbb{1}+i\sigma_k\frac{\partial}{\partial x_k} \end{pmatrix}\begin{pmatrix}\psi_+\\ \psi_-\end{pmatrix}=\begin{pmatrix}0\\0\end{pmatrix} \tag{2.56}$$

Now, Weyl thought it would be a good idea trying to set mass equals to zero ($m = 0$). In this way, the solutions would be decoupled,

$$\begin{pmatrix} \frac{\partial}{\partial x_4}\mathbb{1} - i\sigma_k\frac{\partial}{\partial x_k} & 0 \\ 0 & \frac{\partial}{\partial x_4}\mathbb{1} + i\sigma_k\frac{\partial}{\partial x_k} \end{pmatrix} \begin{pmatrix} \psi_+ \\ \psi_- \end{pmatrix} = \begin{pmatrix} 0 \\ 0 \end{pmatrix}. \tag{2.57}$$

Or in other form

$$\begin{cases} \mathbb{1}\frac{\partial}{\partial x_4}\psi_+ - i\ \sigma_k\frac{\partial}{\partial x_k}\psi_+ = 0 \\ \mathbb{1}\frac{\partial}{\partial x_4}\psi_- + i\ \sigma_k\frac{\partial}{\partial x_k}\psi_- = 0. \end{cases} \tag{2.58}$$

Note that the first equation in Eq. (2.58) can be written as

$$\begin{pmatrix} 1 & 0 \\ 0 & 1 \end{pmatrix} \frac{\partial}{\partial x_4}\psi_+ - i\left(\sigma_k\frac{\partial}{\partial x_k}\psi_+\right) = 0 \tag{2.59}$$

Weyl noticed that for odd spatial dimensions, $d = 1$ for simplicity, this equation can be further simplified (WEYL, 1929). For $k = 1$, we have

$$\begin{pmatrix} \frac{\partial\psi_+}{\partial x_4} & 0 \\ 0 & \frac{\partial\psi_+}{\partial x_4} \end{pmatrix} - i\begin{pmatrix} 0 & \frac{\partial\psi_+}{\partial x_1} \\ \frac{\partial\psi_+}{\partial x_1} & 0 \end{pmatrix} = 0, \tag{2.60}$$

which leads to

$$\begin{cases} \frac{\partial\psi_+}{\partial x_4} = 0 \\ \frac{\partial\psi_+}{\partial x_1} = 0. \end{cases} \tag{2.61}$$

This implies that ψ_+ is independent of x_1 and x_4. The same applies for $k = 2$, since the matrix elements will lead to zero for the derivatives of the wavefunctions.

For $k = 3$, we have

$$\begin{pmatrix} 1 & 0 \\ 0 & 1 \end{pmatrix} \frac{\partial\psi_+}{\partial x_4} = i\begin{pmatrix} 1 & 0 \\ 0 & -1 \end{pmatrix} \frac{\partial\psi_+}{\partial z} \tag{2.62}$$

$$\begin{cases} \frac{\partial\psi_+}{\partial x_4} = i\frac{\partial\psi_+}{\partial x_3} \\ \frac{\partial\psi_+}{\partial x_4} = -i\frac{\partial\psi_+}{\partial x_3}. \end{cases} \tag{2.63}$$

Using the relation $x_4 = ict$ and multiplying by $\hbar$ in both sides, we have

$$\begin{cases} \hbar\frac{\partial\psi_+}{\partial(ict)} = i\hbar\frac{\partial\psi_+}{\partial z} \\ \hbar\frac{\partial\psi_+}{\partial(ict)} = -i\hbar\frac{\partial\psi_+}{\partial z}. \end{cases} \tag{2.64}$$

Multiplying both sides by the speed of light, c, and manipulating i, we obtain

$$\begin{cases} i\hbar\frac{\partial\psi_+}{\partial t} = \left(-i\hbar\frac{\partial\psi_+}{\partial z}\right)c \\ i\hbar\frac{\partial\psi_+}{\partial t} = -\left(-i\hbar\frac{\partial\psi_+}{\partial z}\right)c \end{cases} \tag{2.65}$$

or

$$\begin{cases} i\hbar\frac{\partial\psi_+}{\partial t} = +c\hat{p}_z\psi_+ \\ i\hbar\frac{\partial\psi_+}{\partial t} = -c\hat{p}_z\psi_+. \end{cases} \tag{2.66}$$

Therefore, the equation of motion for ψ_+ acquires the form

$$\boxed{i\hbar\frac{\partial\psi_+}{\partial t} = \pm c\ \hat{p}_z\ \psi_+.} \tag{2.67}$$

Similarly, for the other term of the equation in Eq. (2.58), we have

$$\begin{pmatrix} 1 & 0 \\ 0 & 1 \end{pmatrix}\frac{\partial\psi_-}{\partial x_4} = -i\begin{pmatrix} 1 & 0 \\ 0 & -1 \end{pmatrix}\frac{\partial\psi_-}{\partial z} \tag{2.68}$$

$$\begin{cases} \frac{\partial\psi_-}{\partial x_4} = -i\frac{\partial\psi_-}{\partial z} \\ \frac{\partial\psi_-}{\partial x_4} = i\frac{\partial\psi_-}{\partial z} \end{cases} \tag{2.69}$$

$$\begin{cases} -i\hbar\frac{\partial\psi_-}{\partial t} = -ic\hbar\frac{\partial\psi_-}{\partial z} \\ -i\hbar\frac{\partial\psi_-}{\partial t} = ic\hbar\frac{\partial\psi_-}{\partial z} \end{cases} \tag{2.70}$$

$$\begin{cases} i\hbar\frac{\partial\psi_-}{\partial t} = -c\left(-i\hbar\frac{\partial\psi_-}{\partial z}\right) \\ i\hbar\frac{\partial\psi_-}{\partial t} = c\left(-i\hbar\frac{\partial\psi_-}{\partial z}\right) \end{cases} \tag{2.71}$$

$$\begin{cases} i\hbar\frac{\partial\psi_-}{\partial t} = -c\hat{p}_z\psi_- \\ i\hbar\frac{\partial\psi_-}{\partial t} = +c\hat{p}_z\psi_- \end{cases} \tag{2.72}$$

$$\boxed{i\hbar\frac{\partial\psi_-}{\partial t} = \mp c\hat{p}_z\psi_-.} \tag{2.73}$$

Putting all these together, the equations of motion for ψ_+ and ψ_- are

$$\boxed{\begin{cases} i\hbar\frac{\partial\psi_+}{\partial t} = +c\hat{p}_z\psi_+ \\ i\hbar\frac{\partial\psi_+}{\partial t} = -c\hat{p}_z\psi_+ \\ i\hbar\frac{\partial\psi_-}{\partial t} = -c\hat{p}_z\psi_- \\ i\hbar\frac{\partial\psi_-}{\partial t} = +c\hat{p}_z\psi_- \end{cases}} \tag{2.74}$$

This box contains the Weyl solution where the first two are responsible for conduction electrons and the last two are responsible for the valence electrons, represented by the $\pm$ sings in the wavefunction's indexes respectively. These four nodes, the pair of cones with the same chirality, are separated when we break either one or both symmetries simultaneously, and once we have these broken, we see two nodes splitting into four, as expected in Weyl systems. It is a different case compared to Dirac because in this case we preserve both TRS and IS. The sign of the momentum denotes a right (+) or left(-) moving particle, also known as the chirality of the system, a characteristic of the Weyl's. For dimensions $d > 1$, Weyl solution is still valid, however it is harder to demonstrate do to the matrix order we should work with and since $d = 1$ is sufficient for demonstrating Weyl's solution, we will not extend to higher orders. The reader can use the original Weyl paper for further explanations (WEYL, 1929).

This strange property called chirality in particle physics, is a concept that emerges from Weyl's solution. It is a complex subject and should be understood as a quantum property just like spin. Chirality is only equivalent to helicity (another quantum mechanical concept) when particles are massless, which is the case in Weyl Fermions. Chirality can be viewed as the behavior of the particle's wavefunction when it is rotated. While talking about rotation, it is associated with topological concept and since we have massless particles in Weyl Fermions, can be understood in terms of helicity, which is the projection of the spin in the momentum of the particle. The emergence of chirality is due to the special relativistic property that, once we have massless particles, like photons, there is no preferable frame of reference and chirality and helicity are the same, also, for Weyl Fermions, chirality is invariant under Lorentz transformations.

The Weyl Fermions have momentum $\mathbf{p}$ and spin $\mathbf{s}$, and helicity is the projection of the spin onto the direction of its momentum.

3 Kondo Physics

The Kondo effect is an anomalous phenomenon observed for the first time in 1934 (de Haas; de Boer; van dën Berg, 1934) and shows that below a certain temperature, the material exhibits a behavior in resistivity that was not expected and was in disagreement with the explanation of the time. Jun Kondo proposed a model in which the scattering rate of the conduction electrons of the magnetic impurities present in these materials should diverge as we lower the temperature near $0K$ (KONDO, 1964b). According to Drude's Model, when a system approaches near zero Kelvin, the material should exhibit a residual constant resistance. However, he did not observed the expected behavior, instead he noticed that resistance increased and the scattering rate of the carriers should diverge, in other words, the resistence must increase below a certain temperature [See (3.2)]. There was a characteristic temperature, later called in his tribute as Kondo Temperature as well as the effect, below which this effect takes place.

There are essentially two typical systems where the Kondo effect emerges. One is associated with true magnetic impurities in metals and the other with quantum dots coupled with metallic leads. In the following we will discuss in more detail these two systems. It is very important to emphasize that this effect is purely a quantum behavior, so it can only be understood in this regime having no analogy in the classical realm.

3.1 Kondo Effect due to Magnetic Impurities

For the Kondo effect to take place in magnetic impurities, we first need a conducting material that hosts magnetic atoms and low temperature. As an example of Kondo effect in impurities embedded in a metal is Copper (Cu) doped with Iron (Fe). In this example Cu is our host material and Fe is the magnetic impurity. Fig. 1 shows the resistance (R/R_0) as a function of the temperature $T(K)$, for three different concentrations of Fe (0.05%, 0.1% and 0.2%). When the temperature decreases, we observe a decreasing of the resistance as well. However, at a certain characteristic temperature the resistance reaches a minimum point and R/R_0 starts increasing with further decrease of T. The temperature where the behavior changes is called the Kondo Temperature (T_K). Observe that the curves display an analogous shape, however with different values. For example, T_K for 0.05%-Fe is smaller compared with 0.1% and 0.2%-Fe, however their resistance at that point is higher.

Kondo proposed a local antiferromagnetic interaction between the impurities and the conduction electrons to explain this anomalous effect. He wrote down a model where

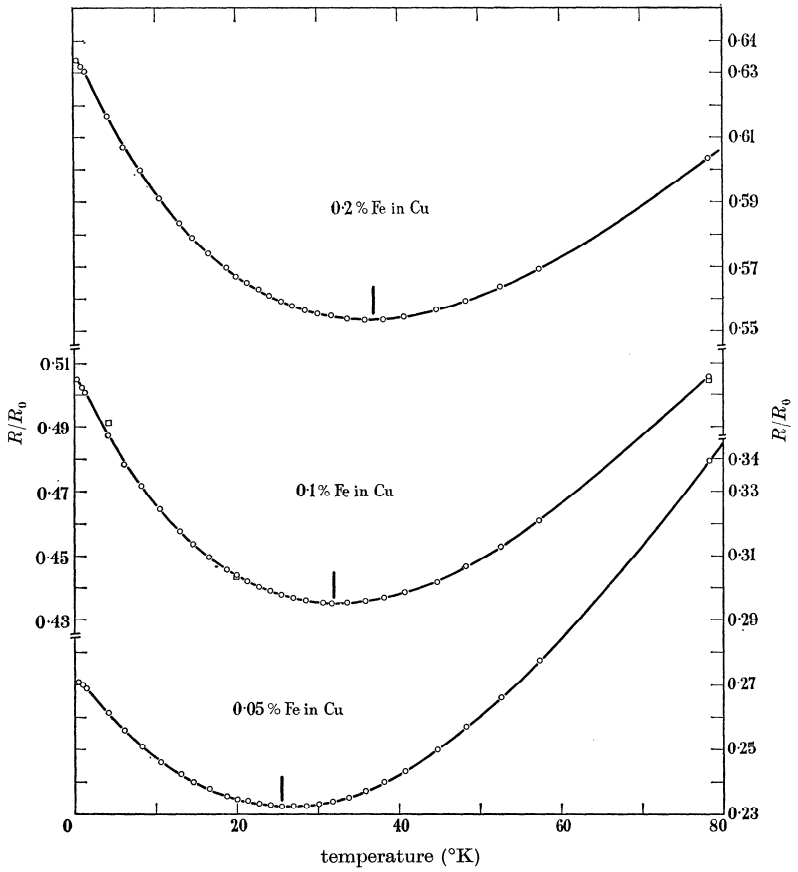

Figure 1 – The electrical resistance (R/R_0) as a function of temperature $T(K)$ of a Copper (Cu) crystal with different concentrations of Fe impurities. The top curve has 0.2% of Fe. The curve in the middle has a 0.1% concentration of Fe and the bottom curve has 0.05%. The vertical dashed line on the lowest part of the concavity of each curve marks the Kondo temperature for this alloy (FRANCK; MANCHESTER; MARTIN, 1961; KRULL, 2014).

he describes this mechanism as

$$H_K = J\vec{s}(\vec{r}=0)\cdot\vec{S}. \tag{3.1}$$

Here, J stands for the nature of the magnetic interaction, in which ferromagnetic and antiferromagnetic corresponds to $J<0$ and $J>0$, respectively (it is good to notice that this J that emerges in Eq.(3.1) should not be confused with the topological charge that is responsible for multi-Wyel systems). $\vec{s}$ represents the spin operator of the conduction electrons in the host and $\vec{S}$ is the impurity spin. By employing a perturbative approach

and considering only the conduction electrons around the Fermi level ε_F on a range of energy of the order K_BT Kondo showed that the electrical resistance can be written as

$$R_T = R_0\left[1 + 2J\rho ln\left(\frac{K_BT}{D-\varepsilon_F}\right)\right], \tag{3.2}$$

where R_0 is the first order electrical resistance, ρ is the density of states and D is a cut on the energy band. It is only in the antiferromagnetic regime ($J > 0$) that Kondo could observe the anomalous effect in the resistivity. The magnetic impurity has a spin oriented in a specific direction $\vec{S}$ and the conduction electrons of the host interacts with it creating an opposite alignment, thus screening the impurity. The screening creates a bound state making it harder for the conduction electrons to move throughout the system. The collection of conduction electrons that screen the impurity creates what is known as the Kondo cloud (BÜSSER et al., 2010; AFFLECK; SIMON, 2001; BERGMANN, 2008; PARK et al., 2013). The Kondo effect has no analog in the classical realm only understandable using a quantum theory approach to describe it. It is not our interest to explore the many facets of Kondo effect in great detail, therefore we are not diving deeper into this subject in different materials. It is, however, interesting to give an idea of this phenomenon since it is a fundamental application of the problem and is something we are looking for in the Weyl systems.

Even though Kondo was able to explain certain experiments, the problem has strong dependency with energy and a perturbative method is not enough to give a full understanding of it, in other words, we would have to consider higher orders of the perturbation series for a better description. Even in this case, we could be missing something for even higher orders. For low energy scales, the perturbation approach can be applied, but it is not true for higher energies. As we know, perturbation theory is only exact if we consider infinite orders. The logarithmic divergences that appears in Feynman diagrams, a pictorial representation of the behavior and interaction between particles (KAISER, 2005), tell us that a perturbation description could not give a complete understanding of the whole picture (ANDERSON; YUVAL; HAMANN, 1970). Also, based on the Schrieffer-Wolff transformation, that not only perturbatively diagonalize a many-body Hamiltonian, but also projects the higher orders excitations of it in a low-energy model (BRAVYI; DIVINCENZO; LOSS, 2011), we can see that the Kondo problem lies in the strong coupling regime as we use an Anderson impurity, which means we need higher orders to describe the problem leading to a more refined theory (ANDERSON, 1961; SCHRIEFFER; WOLFF, 1966).

The lower the energy scale, $\varepsilon = K_BT$, the stronger the coupling between impurity and the electrons of the host, consequently the higher the orders of the perturbation theory we need to describe these interactions. Said that, we need a more accurate method to

describe the strong coupling interactions that take place in low energy scale. This can be understood only under the light of the renormalization group (RG) (ANDERSON, 1961) as we are going to see further in Sec. 5.1. For now, you have to notice that the solution Kondo proposed is limited by the energy scale of the system a problem that RG calculations handles exactly.

The understanding of RG method will allow us to use a numerical approach (Numerical RG, or simply NRG) (see Sec. 5.2) and solve this problem properly.

3.2 Kondo Effect in quantum dots

While Kondo effect in magnetic impurities we have an anomaly in resistivity, the same effect in quantum dots has a different behavior. Although quantum dots are not the interest of this work, they offer a simple description of another application of Kondo effect and can be a candidate for future works and applications such as charge transport (HOSUR; PARAMESWARAN; VISHWANATH, 2012) and photocurrents in Weyl semimetals (CHAN et al., 2017) to name a few.

Quantum dots are artificial structures capable of confining electrons in three dimensional space. In this sense, they behave like atoms, hence they are known as artificial atoms. Their energy levels are easily tuned upon control of applied gate voltages. To understand the Kondo effect and its importance in these systems, we need to comprehend the behavior of the electrons and their interactions when confined in quantum dots.

Suppose we have a single level energy quantum dot ε_0 hybridized to two metallic reservoir under different chemical potentials, as shown in Fig. 2 extracted from (CRONENWETT; OOSTERKAMP; KOUWENHOVEN, 1998). This configuration allows the reservoirs to provide electrons to flow between them through the quantum dot respecting the Pauli exclusion principle and the energies of the quantum dot. The energy μ_L and μ_R ($\mu_L > \mu_R$) are the chemical potential of the left and right reservoir, respectively. If $\varepsilon_0 > \mu_L$, the dot will not let electrons flow from one side to the other, which is not the case in Fig. 2, as we can see in $A1$ ($\varepsilon_0 < \mu_L$ and μ_R, allowing them to flow from one side to the other).

In $A1$, the electron inside the device will produce a strong Coulomb repulsion (U) preventing the occupation of another electron in the quantum dot energy level. Since the Coulomb repulsion U plus the energy level ε_0 in the quantum dot are greater than the chemical potential level of the reservoirs, μ_L and μ_R (in other words $U + \varepsilon_0 > \mu_{L,R}$), then a single electron will occupy the quantum dot. There will be not enough energy for double occupation. Under these conditions, the transition of electrons between reservoirs is not possible, thus no current will flow in this experimental condition ($A1$). This is the result of a phenomenon called Coulomb Blockade (CB). However, at lower T, thermally activated transport will be suppressed and only co-tunneling will occur due to quantum fluctuations.

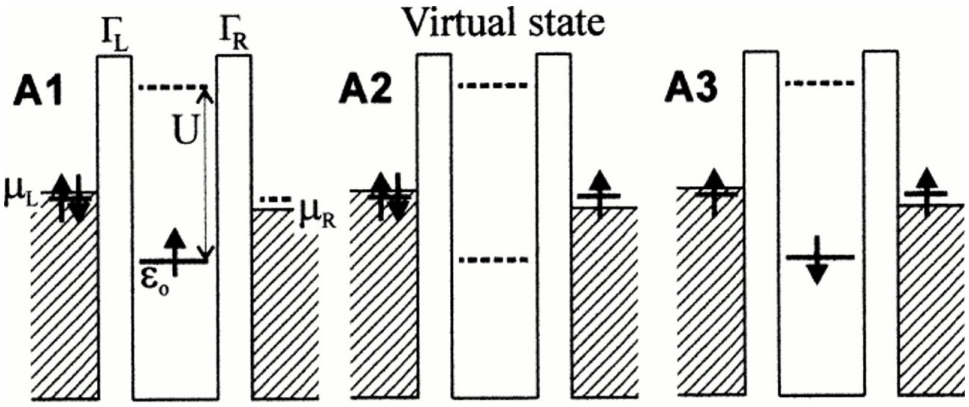

Figure 2 – Virtual states due to Kondo resonance once we reach the characteristic energy scale, Kondo Temperature (K_BT_K). This figure shows a single-level quantum dot with energy ε_0 connected to two reservoir μ_L and μ_R, where $\mu_L > \mu_R > \varepsilon_0$. In $A1$, we can see the occupied quantum dot level by a spin up electron. Because of Coulomb Blockade (CB), another electron with spin down cannot occupy this energy level, so there is no particle flow through it. In $A2$, we reach the energy scale K_BT_K, allowing virtual states, this contributes for the flow of electrons through reservoirs ($A3$). (CRONENWETT; OOSTERKAMP; KOUWENHOVEN, 1998).

These quantum fluctuations are more relevant as compared to thermal ones, there will be electronic transport between reservoirs, even if we are under CB regime, namely when the repulsion is greater than the Fermi level. This is only possible thanks to virtual states, accessible when we lower the energy scale of the experimental example and reach the quantum regime ($A2$). This is analogous to the Kondo problem in magnetic impurities in the sense that the interaction of the electron and the quantum dot can only occur when we access the condition $\varepsilon = K_BT_K$. Under this configuration, the spin can interact with the single energy level quantum dot due to quantum fluctuations. This allow the flow of the electrons from left to right reservoirs thus increasing the conductance of the system ($A3$).

We conclude that there is a significant difference between Kondo in an impurity embedded in a host material and due to quantum dots. In the latter, coherent processes take place and is characterized by a Kondo resonance in the Fermi level, and as a consequence, we observe the increase of the conductance of the system, even when CB is present. While in the system described in section 3.1, there is an increase in the resistivity due to the same nature of interaction, the Kondo resonance.

After the Kondo physics in the context of magnetic impurities, we have a better understanding of it and how this very effect can be applied resulting in opposite effects, the increase of resistivity in hosts doped with magnetic impurity and the increase of

conductivity in quantum dots when we reach a characteristic energy scale. Kondo effect can be explored in different contexts showing its vast scientific versatility.

When we have a host material such as Weyl semimetals, with a magnetic impurity embedded in it they will interact via hybridization function Γ. This function is responsible for describing the communication between host and magnetic impurity and will be extensively discussed in future sections since it is an important information to obtain other properties such as temperature, density of states and magnetization. The magnetic impurity is a local moment and the free electrons in the conduction band of the host material will feel the presence of this local moment. If the material presents an antiferromagnetic configuration in the host material, it will provide electrons capable of screening the magnetic impurity so Kondo effect can emerge.

An impurity coupled to host materials containing quasiparticles, such as Weyl SM, that present a strong particle-hole (PH) asymmetry is expected to have a pseudogap Kondo. When we have a finite chemical potential or a broken IS we induce this kind of phenomenon due to its asymmetric PH contribution (MITCHELL; FRITZ, 2015b). These pseudogaps are point-like regions on the Fermi surface, and that is exactly what happens in Dirac/Weyl systems, where we have these semimetals that are described by a DoS as $\rho(\omega) \propto |\omega|^r$, where $r = 2/J$, where J is a topological number that will be discussed in further detail later (TIMUSK; STATT, 1999; VOJTA; FRITZ, 2004; FRITZ; FLORENS; VOJTA, 2006). We study the behavior of the DoS depending on the values of $r = 2/J$ and discuss the emergence of Kondo physics. In cases like the Dirac metal, where μ is finite, providing free electrons to screen the impurity, which is well known in literature, we have Kondo physics. In some special cases, even for PH symmetry and $\mu = 0$, we show that by breaking and increasing IS, we can provide electrons to screen the impurity, reaching the pseudogap Kondo regime which was not yet described by the scientific community. We are going to show in this work, using the model presented here, that pseudogap Kondo emerges in MWSM and MDSM in PH symmetry due to the broken IS.

4 Kondo effect in Dirac and Weyl Systems

In this chapter, we discuss in more details the object of this study. We first present the Weyl and Multi-Weyl systems. The methods are rigorously presented in a chronological order, to make it easy for the reader to follow the discussion. In sec. 4.1 we present the Weyl systems and in sec. 4.2 we will see that there is a generalization of Weyl semimetals, the so called Multi-Weyl semimetals (MWSM).

4.1 Weyl Systems

When we study Weyl systems, the first figures we see in articles are those cones facing up against each other and touching in a single point, they represent the dispersion relation of these materials, which is the energy of the bands. This point occurs and gives the name semimetal, because we have a regime whether valence and conduction bands touch in a single point, in a stable region. The double degenerate bands when we preserve Time-Reversal and Inversion symmetries, which is equivalent to a Dirac semimetal or metal depending on if chemical potential is zero or not. For instance, if we break TRS, by applying an external magnetic field, the Dirac-like system split into a left and right handed chirality cones characterizing Weyl systems, even preserving IS. For finite structures, presenting surface states, if there is a degeneracy over the top of each cones, we have something called Fermi-arcs. These surface states happens only in the condensed matter context (WAN et al., 2011) and can be understood as the signature of Weyl systems. When we consider the four nodes, composed of positive and negative chiralities, the total momentum of the system is preserved. The right-hand chirality has $\pm\mathbf{p}$ momentum while the left hand chirality has $\mp\mathbf{p}$ momentum.

The first experimental observations of Weyl semimetals, in the context of condensed matter, in a TaAs crystal, was recently observed (XU et al., 2015b). Using a technique called angle-resolved photo-emission spectroscopy (ARPES), an experimental method based on the photoelectric effect, they could observe surface states showing Fermi arcs of the chiral cones for valence and conduction bands. Since then, the scientific community has devoting great deal of effort studying and exploring these structures and this exotic effect (JIA; XU; HASAN, 2016; LI et al., 2018; RAO et al., 2019). These characteristic cones in the dispersion relation for Weyl semimetals when TRS is broken, in Fig. 3 for example, can be deformed if we change the parameters of the Hamiltonian and change the exponents of host electrons wave vectors, $\mathbf{k}$, in other words, we can change the dispersion relation due to manipulations in the model in order to obtain single Weyl, double Weyl (2-Weyl) or triple Weyl (3-Weyl) systems. When we do that, we change the isotropic behavior on the

energy of the system as shown in Fig. 4. Now, the cones are not symmetric in all directions and we have what we call mult-Weyl systems (Fig. 4 b and c). The 2-Weyl semimetals were found in $HgCr_2Se_4$ (XU et al., 2011; FANG et al., 2012) and $SrSi_2$ (HUANG et al., 2016) crystals and 3-Weyl semimetals were predicted in $A(MoX)_3$ (with $A = Rb$, TI and $X = Te$) (LIU; ZUNGER, 2017). Theoretical studies are also being conducted in the direction of multi-Weyl (EZAWA, 2017; WANG; LIU; ZHANG, 2019; LÜ et al., 2019). In order to contribute to Kondo physics in multi-Dirac and multi-Weyl systems and different regimes. To this end, we choose a Hamiltonian model that allows to explore different system families such as multi-Weyl metals and semimetals, whether breaking or preserving TRS and IS, in order to understand the different regimes where Kondo emerges.

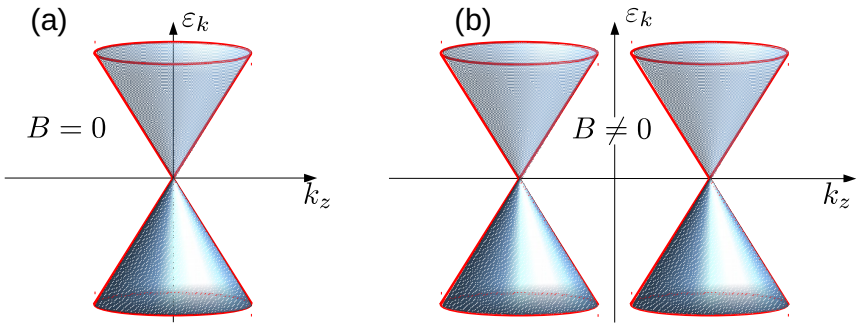

Figure 3 – Dispersion Relation of the model Hamiltonian. (a) Dirac Semimetal ($TRS = 0$ and $IS = 0$) e (b) Weyl Semimetal breaking TRS only ($TRS = 1$ and $IS = 0$). Since TRS is related to the magnetic field B, if TRS is broken we have $B \neq 0$. This figure was reproduced using the model Hamiltonian presented in this work.

It should be emphasized that Weyl systems are massless Dirac systems that have either or both TRS and IS broken. Because of the antiferromagnetic phase property of some materials such as Na_3Bi and Cd_3As_2 for Dirac systems and $TaAs$ and $NbAs$ in case of Weyl systems, they can sustaining Dirac points (XIONG et al., 2015). We consider a magnetic impurity that is coupled to these materials. Their aintiferromagnetic phase will allow the host electrons to interact with the magnetic impurity forming a screening so the Kondo physics can emerge.

Before addressing the main model we are interested in this work, we will discuss the Kondo effect in a specific Hamiltonian proposed by Andrew Mitchell (MITCHELL; FRITZ, 2015a). Upon comprehending this model, we were able to develop the methods used in a more general case. For concreteness, the Dirac-Weyl Hamiltonian considered by Mitchell, can be written as

$$\hat{\mathbf{H}} = \hat{\mathcal{H}}_D + \delta\hat{H}, \tag{4.1}$$

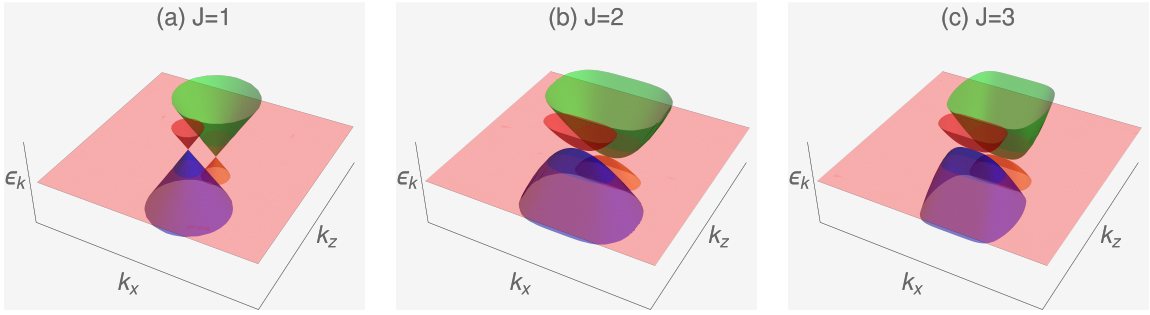

Figure 4 – The dispersion relation $\varepsilon_{\mathbf{k}}$ of a (a) Weyl semimetal $J = 1$, (b) a 2-multi-Weyl semimetal $J = 2$ and (c) 3-multi-Weyl semimetal. Here we fixed $k_y = 0$. Note that both TRS and IS are broken in this case.

where

$$\hat{\mathcal{H}}_D(\vec{k}) = v_F \hat{\tau}_z \otimes \vec{k} \cdot \hat{\sigma} \tag{4.2}$$

describes a bare Dirac material and $\delta\hat{H}$ is introduced to break the desired symmetry. In Eq. (4.2) $\hat{\sigma}$ and $\hat{\tau}$ are the Pauli matrices acting over the spin and orbital spaces, respectively, and v_F is the effective Fermi velocity. Following Mitchell, the perturbation term $\delta\hat{H}$ is given by

$$\delta\hat{H} = \Big(\vec{a} \cdot \vec{\tau} + a_0\tau_0\Big) \otimes \Big(\vec{b} \cdot \vec{\sigma} + b_0\sigma_0\Big), \tag{4.3}$$

where $\vec{a}$ is the IS parameters, $\vec{b}$ is the TRS parameter, while a_0 and b_0 are constants. Depending on the parameters of this Hamiltonian, the perturbation can lead to different symmetries and, consequently, break or preserve both symmetries, break TRS and preserve IS or preserve TRS and break IS. For instance, we have Dirac Metal if we preserve both symmetries and Weyl semimetal if we break TRS and preserve IS if we have the presence of $\vec{b}$. Also, the spin and orbital spaces will ensure different configurations depending on the combinations of their directions.

As an example, we consider the systems represented in Fig. 5. For a perturbation $\delta\hat{H} = -\mu\hat{\tau}_0 \otimes \hat{\sigma}_0$ (First line) we have a Dirac metal, where TRS and IS are preserved. In this case, Kondo physics emerge once we have $\mu \neq 0$, displacing the Fermi level to a region where the contribution of free electrons can now screen the impurity. If we observe the second line, where we have Dirac insulator (TRS and IS preserved), Kondo peak is suppressed and a Free Local Moment appears, due to the lack of free electrons in the Fermi level to screen the impurity. For $\delta\hat{H} = \hat{\tau}_0 \otimes \vec{b} \cdot \vec{\sigma}$ we have a Weyl semimetal with TRS broken while IS is preserved. Note that for this case, there is a symmetric behavior of dispersion for $\vec{k}$, characterizing the Weyl Semimetal where we do not have that single sharp peak in the spectral density $t(\omega)$ characterizing Kondo. This is due to $\mu = 0$ and so, not enough electrons to screen the impurity and a polarized local moment emerges in $t(\omega)$.

For the case in the last line, $\delta\hat{H} = a\hat{\tau}_z \otimes \hat{\sigma}_0$, we have a Weyl Metal. Here, TRS is preserved while IS is broken because the parameter a that is associated with the orbital space. Since IS displaces the nodes, we have contributions as if we are changing μ compared to Dirac metal, depending on the manipulation of the parameters, a pseudogap Kondo emerges in this regime.

In the case of Fig. 5 we have a summary of the different perturbations that leads to different configurations of the Hamiltonian. We have six different models depending on the perturbation. Each one has its dispersion relation given by E as a function of k_x and k_y, fixing k_z. The Density of States (DoS), $\rho_\sigma(\omega)$ for a given spin σ and the spectral function $t(\omega)$ for $T = 0K$. The NRG band cutoff is established as $D = v_F = 1.0$ and Coulomb repulsion $U = 0.3$. The impurity symmetry is set to be particle-hole symmetry $\eta = -2\varepsilon/U = 1.0$ and the coupling term or hopping term $V = 0.2$, for all except the fifth case, where the particle-hole symmetry is set as $\eta = 1/2$ and the hopping term varies $V = 0.420, 0.479, 0.520$ as represented in Fig. 5 for the Asymmetric Local Moment (ALM), Nontrivial Interacting Critical point (ACR) and Asymmetric Strong Coupling (ASC), respectively. The chemical potential is set to be $\mu = -1/3$ for the first case, $m = 0.1$ for the second, $b_z = 0.10$ for the cases 3, 4 and 5 and $a = 1/3$ for the last case. it is worth mentioning that we also obtained the spectral function $t(\omega)$ with the NRG, using the methods described in section Sec. 5.2.

From this model, we reproduced some important work in literature (MITCHELL; FRITZ, 2015a) and was the beginning of the discussion of Kondo in Weyl systems, which we are not going to present here only mentioning that our work started with the reliability test via reproducing what was well established. Based on this study, comprehending the steps from the model to the numerical implementation, we developed the numerical methods for the the multi-Weyl model with another more general Hamiltonian. However, this was a very important step for the understanding of symmetry breaking methods and how to manipulate variables of the model in order to implement the numerical tools to do so in a more general case. The contribution in this present work is to explore beyond 1-Weyl metals and semimetals and explore where those cases presented in Fig. 5 are not symmetric cones anymore, in other words, when k_x and k_y do not behave like k_z, distorting the Weyl cones.

4.2 Multi-Weyl Semimetals

From a theoretical point of view, multi-Dirac/Weyl systems are extensions of the Dirac/Weyl systems, more precisely, a generalization of the massless Dirac and Weyl cases. This new property of these materials can be vastly explored since it is a novel subject on the scientific community. From this study, we mainly explore how Kondo physics emerges

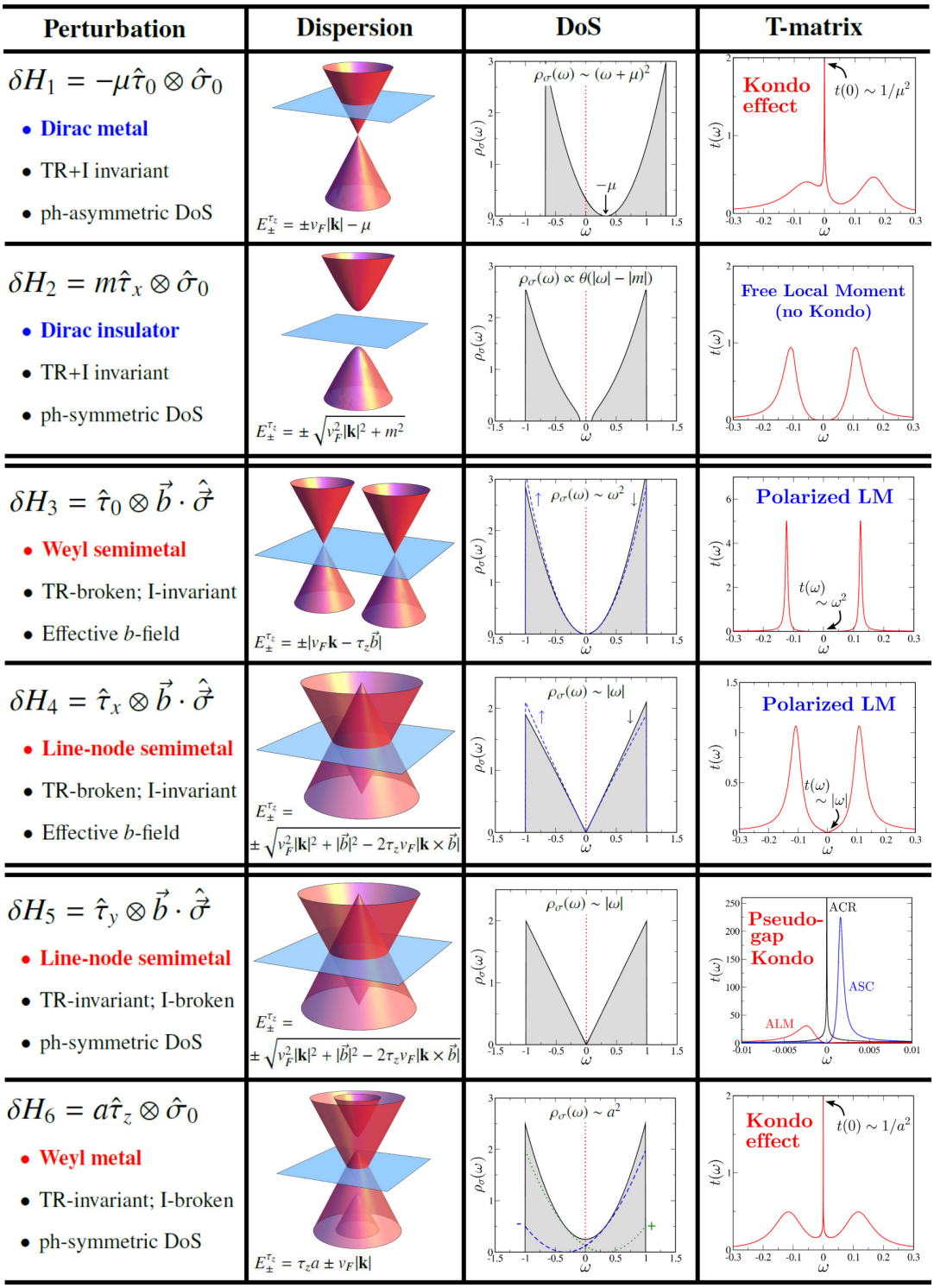

Figure 5 – Six possible cases related to the nature of the perturbation on the first column, the Dispersion relation on the second, DoS on the third and spectral function on the fourth column (MITCHELL; FRITZ, 2015a).

for different regimes of the model Hamiltonian.

The multi-Dirac/Weyl semimetals are characterized by abundant topological charge or topological invariant. Dirac and Weyl semimetals, for example, have symmetric dispersion relation with respect to Fermi Level plane. When it loses its symmetry or when we have anisotropic energy dispersion, it leads to an increase of topological charge, a characteristic of multi-Weyl and multi-Dirac systems. The topological charge only assumes discrete set of numbers and is related to the topological defects on the structure of the system such as strains in crystalline structure. The charge of a solved system is called the winding number and is represented by J and when the this number is two we have a 2-multi-Dirac/Weyl case and if it is three, the system is named 3-multy-Dirac/Weyl one, and so on. Since this topological property is related to the defects on the structure of the material, quite often because of its boundary conditions, we have spatial limitations on its dimensions, so we are going to stick to a 3-dimensional winding number (LÜ et al., 2019; FANG et al., 2012).

We are not going to extend this section since it is not the object of this work to explore the topological concepts but only apply them to the systems of interest. For a more complete discussion of this theme, I suggest the following Ref. (J.THOULESS, 2012).

In the next section, we will consider a model capable of describing multi-Dirac and Weyl systems with winding number up to 3. The winding number appears as a parameter of the Hamiltonian and can be simply manipulated, regardless of possible difficulties in implementing it experimentally.

4.3 Model

In this section we explore the model that allows us to develop the multi-Weyl system. The multi-Weyl and multi-Dirac metals and semimetals are due to a non linear anysotropy in dispersion relation associated with a topological charge parameter J in the Hamiltonian, as we discussed in Sec. 4.2. This parameter is responsible for changing from Weyl system when $J = 1$, to multi-Weyl cases, more specifically double-Weyl when $J = 2$ and triple-Weyl when $J = 3$ or simply multi-Weyl, noticing we already have either TRS or IS broken or both, leading to an anysotropy in energy since it is a function of the three directions on the wave vector $\mathbf{k}$.

For completeness, the total Hamiltonian that describes our system can be split into three terms as $H = H_0 + H_{\text{imp}} + H_{\text{V}}$, where H_0 represents the clean multi-Weyl/Dirac fermion system, H_{imp} describes the impurity Hamiltonian, and H_{V} accounts for the hybridization between them. Introducing the spinor

$$\Psi^{\dagger}_{\mathbf{k}} = (c^{\dagger}_{\mathbf{k}+\uparrow}, c^{\dagger}_{\mathbf{k}+\downarrow}, c^{\dagger}_{\mathbf{k}-\uparrow}, c^{\dagger}_{\mathbf{k}-\downarrow}), \tag{4.4}$$

in which $c^{\dagger}_{\mathbf{k}ps}$ creates a fermion with momentum $\vec{k}$, chirality $\pm p$, as defined in Chapter 2.2, and spin $s =\uparrow,\downarrow$, we can write

$$H_0 = \sum_{\mathbf{k}} \Psi^{\dagger}_{\mathbf{k}} \mathcal{H}_{\mathbf{k}} \Psi_{\mathbf{k}}$$

, with

$$\begin{aligned} \mathcal{H}_{\mathbf{k}} &= \tau_z \otimes \left[v_{\perp} k_0 \left(\tilde{k}^J_{-} \sigma_{+} + \tilde{k}^J_{+} \sigma_{-} \right) + v_z k_z \sigma_z - Q_0 \sigma_0 \right] \\ &\quad - v_z Q \tau_0 \otimes \sigma_z - \mu \tau_0 \otimes \sigma_0. \end{aligned} \tag{4.5}$$

Here, μ is the chemical potential, it will tell us if the material is a metal or a semimetal, for zero temperature, the chemical potential is the Fermi energy. $v_{\perp}$ and v_z, are effective velocities perpendicular and parallel with respect to z, respectively, and $\tilde{k}_{\pm} = (k_x \pm i k_y)/k_0$ with k_0 being system-dependent constant. These are parameters of the Hamiltonian that we kept constant and equal to one. Of key importance in this work are the parameters Q and Q_0, responsible for breaking time reversal (TRS) and inversion (IS) symmetries, respectively. These ones are responsible for giving us the Dirac or Weyl systems, depending on how we choose the values. These values were explored with detail and will be exposed in the results section. The exponent J in Eq. (4.5) represents the winding number associated with the multi-Weyl/Dirac topological charge (FANG et al., 2012) and is responsible for the anysotropy in the dispersion relation. As you can see it changes the exponents of k_x and k_y. If we keep $J = 1$, both k_x and k_y have the same dimension of k_z, leading to the usual cases of Dirac/Weyl systems, that is not true for $J > 1$, that will allow us to access the multi cases. Finally, σ and τ are Pauli matrices acting on the spin and chirality sectors of the Hilbert space, respectively, with σ_0 and τ_0 being the corresponding identities. To simplify the notation, we have introduced $\sigma_{\pm} = \left(\sigma_x \pm i\sigma_y\right)/2$.

The impurity Hamiltonian in turn can be written as

$$H_{\text{imp}} = \sum_{s=\uparrow,\downarrow} \left(\varepsilon_d - \mu\right) d^{\dagger}_s d_s + U n_{d\uparrow} n_{d\downarrow}, \tag{4.6}$$

where $d^{\dagger}_s(d_s)$ creates (annihilates) an electron in the impurity with spin s and energy ε_d at the impurity site. $n_{d\sigma} = d^{\dagger}_{\sigma} d_{\sigma}$ is the impurity number operator and U is the Coulomb interaction repulsion energy.

Assuming, for simplicity, that the impurity hybridizes equally with all bands with a $\vec{k}$-independent matrix element V [1], the Hamiltonian H_{V} can be written as $H_{\text{V}} = \sum_{\mathbf{k}} (\Psi^{\dagger}_{\mathbf{k}} \hat{V} \Psi_d + \text{H.c})$, where $\Psi^{\dagger}_d = (d^{\dagger}_{\uparrow}, d^{\dagger}_{\downarrow})$ and $\hat{V}$ is a matrix given by (LÜ et al., 2019)

$$\hat{V} = \begin{pmatrix} V & 0 & V & 0 \\ 0 & V & 0 & V \end{pmatrix}. \tag{4.7}$$

[1] Assuming $\mathbf{k}$-independent matrix element V implies a point-like hybridization between the impurity and host orbitals. A more realistic approach to a specific material should account for the structure of the orbitals involved in the hybridization.

To access the low-energy physics of the full system we employ the NRG method which allows us to compute the impurity spectral and thermodynamic properties (BULLA; COSTI; PRUSCHKE, 2008). Within this method, the entire effect of the host material on the impurity is given by the so-called hybridization function, $\Gamma(\omega)$. To obtain this quantity, we define local Green's function (NOLTING; BREWER, 2009)

$$\hat{G}_{\text{imp}}(\omega) = \left[(\omega - \varepsilon_d)\sigma_0 - \hat{\Sigma}^{(I)}(\omega) - \hat{\Sigma}^{(0)}(\omega)\right]^{-1}, \tag{4.8}$$

where $\hat{\Sigma}^{(I)}(\omega)$ and $\hat{\Sigma}^{(0)}(\omega)$ are the interacting and hybridization self-energies. The latter accounts for the effect of the host fermions on the impurity and is formally given by

$$\hat{\Sigma}^{(0)}(\omega) = \int \frac{d\mathbf{k}}{(2\pi)^3} \hat{V} G^{\text{host}}_{\mathbf{k}}(\omega) \hat{V}^{\dagger}, \tag{4.9}$$

in which

$$\hat{G}^{\text{host}}_{\mathbf{k}}(\omega) = \left[\omega \mathbb{I} - \mathcal{H}_{\mathbf{k}}\right]^{-1}. \tag{4.10}$$

In spherical coordinates, $k_x = k\sin\theta\cos\phi$, $k_y = k\sin\theta\sin\phi$, and $k_z = k\cos\theta$, the Green's function (4.10) can be recast in the matrix form

$$\hat{G}^{\text{host}}_{\mathbf{k}}(\omega) = \begin{pmatrix} g_{+,Q_0,Q}(k,\theta) & -e^{-iJ\phi}F_{Q_0,Q}(k,\theta) & 0 & 0 \\ -e^{iJ\phi}F_{Q_0,Q}(k,\theta) & g_{-,Q_0,Q}(k,\theta) & 0 & 0 \\ 0 & 0 & g_{-,-Q_0,-Q}(k,\theta) & e^{-iJ\phi}F_{-Q_0,-Q}(k,\theta) \\ 0 & 0 & e^{iJ\phi}F_{-Q_0,-Q}(k,\theta) & g_{+,-Q_0,-Q}(k,\theta) \end{pmatrix}.$$

In the above we have defined

$$g_{\pm,Q_0,Q}(k,\theta) = \frac{1}{\omega + \mu + Q_0 \mp v_z(k\cos\theta - Q) - \frac{k_0^2 v_\perp^2 \left(\tilde{k}\sin\theta\right)^{2J}}{\omega+\mu+Q_0 \pm v_z(k\cos\theta - Q)}} \tag{4.11}$$

and

$$F_{Q_0,Q}(k,\theta) = \frac{k_0 v_\perp \left(\tilde{k}\sin\theta\right)^J}{k_0^2 v_\perp^2 \left(\tilde{k}\sin\theta\right)^{2J} + v_z^2(Q - k\cos\theta)^2 - (\mu + Q_0 + \omega)^2}. \tag{4.12}$$

With these expressions, the integrand of Eq. (4.9) becomes

$$\hat{V}\hat{G}^{\text{host}}_{\mathbf{k}}(\omega)\hat{V}^{\dagger} = V^2 \begin{pmatrix} A_{Q_0,Q}(k,\theta) & e^{-iJ\phi}B_{Q_0,Q}(k,\theta) \\ e^{iJ\phi}B_{Q_0,Q}(k,\theta) & A_{-Q_0,-Q}(k,\theta), \end{pmatrix} \tag{4.13}$$

where $A_{Q_0,Q}(k,\theta) = g_{+,Q_0,Q}(k,\theta) + g_{-,-Q_0,-Q}(k,\theta)$ and $B_{Q_0,Q}(k,\theta) = F_{-Q_0,-Q}(k,\theta) - F_{Q_0,Q}(k,\theta)$. Transforming the integral (4.9) into spherical coordinates, it is easy to see that the off diagonal terms vanish under integration over the azimuthal angle ϕ, while the remaining diagonal terms can be written as

$$\Sigma^{(0)}_s(\omega) = \frac{V^2}{4\pi^2}\int_0^\infty k^2 dk \int_0^\pi d\theta \sin\theta A_{sQ_0,sQ}(k,\theta,\omega). \tag{4.14}$$

On the right hand side of the expression above, $s = +1$ and -1 for spin $\uparrow$ and $\downarrow$, respectively. We ask the reader not to mistake the s in $A_{sQ_0,sQ}(k,\theta,\omega)$ for spins but only the signs that multiplies Q and Q_0. For practical purpose we introduce a cutoff k_c to truncate the integral over k [2].

Within the NRG approach, the effect of the host material on the impurity and entirely accounted for by *hybridization function* defined as

$$\Gamma_s(\omega) = -\mathrm{Im}[\Sigma_s^{(0)}(\omega + i0^+)]. \tag{4.15}$$

The integration in Eq. (4.14) is rather complicated and, in general, cannot be performed analytically. Therefore, we solve it numerically via the introduction of the integrals of Eq. (4.14) in any numerical software capable of calculating it. Having the numerical results for $\Gamma_s(\omega)$ we apply the standard numerical logarithmic discretization scheme described in Ref. (BULLA; COSTI; PRUSCHKE, 2008).

To get some insight on what we expect from our numerical results for the Kondo physics, it is instructive to take a close look at the structure of the hybridization function in the various regimes of the Hamiltonian model. This will allow us to compare the Kondo regimes expected here with those already known in the literature. For a given set of parameters of the host Hamiltonian, the contribution for $\Gamma_s(\omega)$ is associated to the four energy bands of the clean multi-Weyl/Dirac node system [obtained upon diagonalizing the Hamiltonian (4.5)],

$$\varepsilon_{hs\vec{k}} = h\sqrt{k_0^2 v_\perp^2 \tilde{k}_\perp^{2J} + v_z^2 \left(Q - sk_z\right)^2} - sQ_0 - \mu. \tag{4.16}$$

Here, $k_0^2\tilde{k}_\perp^2 = k_x^2 + k_y^2$, h represents conduction (+) and valence (-) bands and $s = \pm$ is the quantum number resulting from linear combinations of the original spin and chirality quantum numbers (we advise the reader to be careful not to confuse these sub-indexes in the dispersion relation with quantum numbers defined above. Even though these are related to quantum numbers, the choice of indexes are merely illustrative, having the purpose to tag each band.). These bands are shown in the three upper layers of Fig. 6. Each of these layers corresponds to a given value of J indicated on the left hand side of the figure, while a given set of Q and Q_0 is indicated by the pair (Q, Q_0) placed at the top of each column.

In first column of Fig. 6, we have the degenerated conduction and valence bands once we preserve both TRS and IS, (0,0) respectively. The column starts with $J = 1$ and

[2] This is the cutoff, more like a limitation of the method. The ideal case would have to be integrated over all space and see the contribution of it, however the numerical method cannot perform an integration from $-\infty$ to $+\infty$, so we have to truncate it with this parameter. It is worth noticing that k_c is problematic because the numerical method has a hard time handling with it. We choose the cutoff k_c such that the total density of states of the host electrons, normalized within $[-D, D]$ and calculated for $Q_0 = Q = 0$, does not change significantly upon a further increase of k_c. Note that D is an ultraviolet energy cutoff (imposed independently from k_c) that establishes a finite bandwidth for the host material.

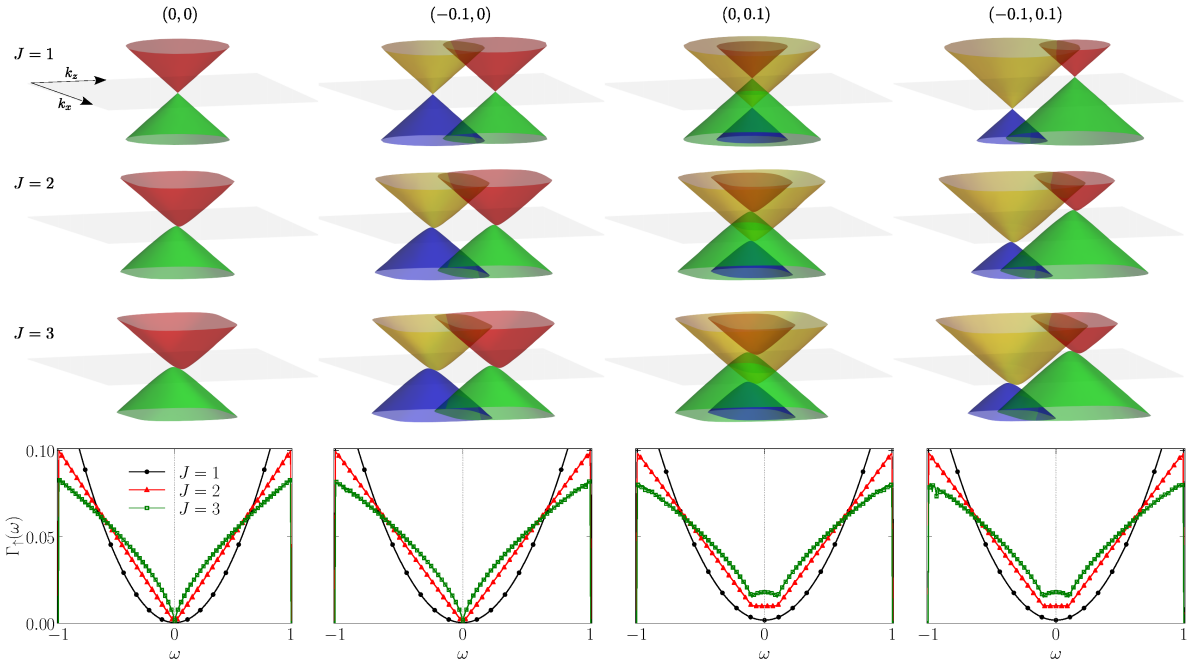

Figure 6 – Energy bands vs k_x and k_z ($k_y = 0$) (top three layers) and hybridization vs energy for different values of J (lowest layer). The different columns correspond to different values of Q and Q_0 indicated by the pairs (Q, Q_0) at the top of the columns. The dashed gray vertical lines in the lowest panels represent the chemical potential, here set at $\mu = 0$. Other parameters are $k_0 = v_\perp = v_z = 1$.

if we go back to the Hamiltonian (4.5) and to the dispersion relation (4.16), the momentum k_x, k_y and k_z have the same value of exponents when $J = 1$, so we have symmetric valence and conduction bands with respect to $k_x k_z$ plane. For $J = 2$, we can see that the nodes are not symmetric in $k_x k_z$ plane anymore and the asymmetry is even larger for $J = 3$ in the third line. In the second column of Fig. 6, we break TRS and preserve IS, (-0.1,0) respectively. The negative sign in Q is due to our magnetic field, $B = -v_z Q$ [we are going to discuss it in Sec. 4.4]. For this configuration, there is a break on the degeneracy and we see four nodes, the conduction and valence bands on the right (red and green, respectively), valence and conduction on the left side (yellow and blue, respectively) (the inversion of valence and conduction bands are described by Weyl's solution to Dirac's Equations). The right side nodes have positive chirality while the left side nodes have negative chirality. The asymmetry in the dispersion relation increases with the increase of J, in fact, the first line where $J = 1$, we will have symmetric dispersion relation. The second line, where $J = 2$, we have an asymmetry in dispersion relation that increases with $J = 3$ on the third line. For the third column in Fig. 6, we preserve TRS and break IS, (0,0.1) respectively. We see a displacement of the nodes merging each other as the IS break causes the nodes to displace the red-green nodes to move vertically down while the yellow-blue nodes will move vertically up breaking the degeneracy. The last column in Fig. 6, we break both symmetries so we observe a displacement of the red-green nodes moving right and down,

while the yellow-blue nodes move left and up.

The lower layer of Fig. 6 shows the hybridization function of spin up for different representative instances of the multi-Weyl and Dirac node cases studied here. We only plot the spin up $\Gamma_\uparrow$ because it is degenerate to the $\Gamma_\downarrow$. The dots on each curve are the numerical points. We have black red and green curves for $J = 1$, 2 and 3, respectively. The curves obey the relation $\rho \propto |\omega|^{2/J}$. When we break TRS and preserve IS, there is no change in $\Gamma_\uparrow$, however if we break IS in any case, there is a finite hybridization function in its lower point ($\Gamma(\omega = 0) \neq 0$) that increases with J. Since there is a similarity between Γ and the DoS, this gap will also be present in the DoS allowing pseudogap Kondo.

In the next section we will discuss in detail the various features of the hybridization function alongside the discussion of the Kondo physics dredged up by the NRG calculations.

Our first approach to these multi-Weyl and multi-Dirac systems was using an analytical description, however we encountered major difficulties and the problem had no solution due to its complexity in solving for a wide variety of parameters and degrees of freedom such as s and h.

4.4 Spin-Polarization in Weyl Semimetals $\mu = 0$

The model Hamiltonian (4.5) has a term that can be understood as a magnetic field. This term, by comparison with the behavior of the Zeeman Effect $\langle S_z \rangle$ is presented in our model as the magnetic field $B = -v_z Q$. Also, we can control whether k_x, k_y and k_z is zero or not by adopting various values for them. Our model is three- dimensional and since we are plotting a two dimensional view of the dispersion relation, we will fix two and the other will be our variable. These results are qualitative and the parameters were chosen just for plotting the magnetization, then some of those will differ from previous values. A variety of behavior in the bands will emerge as we manipulate the two other momenta that are fixed. We can see that $\langle S_z \rangle$ changes its value for each band smoothly when either of the two fixed parameters are finite. We also tested different combinations of symmetry breaking, as you can see in the following pictures where we preserve IS and break TRS, preserve TRS and break IS, break both symmetries or preserve both. We have four distinct cases for each plot depending on the combination of chirality and valence/conduction bands. The quantum numbers in the dispersion relation ε_{sh} (s and h) stands for chirality and valence/conduction bands, respectively. Remember that here we changed the indexes. This will give us the tags for each band in the plots. For instance, ε_{++} is the conduction band with positive chirality, while ε_{--} is the valence band with negative chirality. We also have the conduction band with negative chirality, ε_{-+} and the valence band with positive chirality, ε_{+-}. The bands are given by the blue/red colors, where blue means negative magnetization, while red is positive. A colormap is displayed

on the right side of each plot with the respective value of $\langle S_z \rangle$. The cases we are about to study are Weyl systems only, $J = 1$ and can be extend for $J = 2$ and 3 in future studies. The behavior of these bands are associated with the Eq. (4.16). Note that since we will have terms inside the square root that are not zero, the dispersion relation does not go to zero in its lowest point. We should emphasize that it is not a gap but a kinetic energy due to finite momentum of the electrons. The following study will analyze the plot of dispersion relation in terms of a specific momentum and keeping the other two as constants.

The expression that allows us to calculate the magnetization $\langle S_z \rangle$ can be written as

$$\langle S_z \rangle = \sum_{sh} \langle sh | \hat{S}_z | sh \rangle, \tag{4.17}$$

where $|sh\rangle$ are the diagonal eigenvectors of Eq. (4.5) and the magnetization matrix can be expressed as

$$\hat{S}_z = \sigma_0 \otimes \sigma_z, \tag{4.18}$$

σ_0 and σ_z are Identity and Pauli matrix, respectively.

In the first case, we break TRS and IS and plot ε_{sh} as a function of k_z, so k_x and k_y will be constants. Note that our model Hamiltonian (4.5) is symmetric in k_x and k_y, meaning that switching k_x and k_y does not change the results, in other words, our model is symmetric for rotations in the plane $k_x k_y$. The parameters k_x and k_y add two more degrees of freedom to the system and for this reason we have four plots for each case of each set of symmetries. For our first case, in Fig. 7, TRS and IS are broken, so we have a non degenerate Weyl semimetal with a displacement in both directions, horizontally and vertically. When k_x and k_y are zero, we have constant magnetization on each band, which is also equivalent to say that the Hamiltonian is diagonal, otherwise the magnetization would vary in each band. The mix between momenta, due to the Hamiltonian, is responsible for the behavior of the magnetization varying for each band. Since $\langle S_z \rangle$ is associated with the magnetic field, $B = -v_z Q$, if we change the sign of Q we also change the magnetization in the bands, in terms of our plots, the positive magnetization (red in colormap representation) will become negative (blue in colormap representation), and vice-versa.

Note that broken IS contributes for the unbalance of the energy bands. We can see that one band contributes more than the other due to this asymmetry. We can preserve the TRS and analyze the dispersion relation $\varepsilon(k_z)$ while breaking only IS. In this case, we have Fig. 8, where the preservation of TRS kept the bands centered, and the displacement is only in the vertical direction. Again, cases (b) and (c) are identical due to the symmetry of the Hamiltonian for k_x and k_y. Comparing the cases (b) and (c) to the case (a), we observe that the distance between bands is greater for greater contributions, in this case, when we have $k_x = k_y = 1$. In case (d), we notice that $\langle S_z \rangle$ is constant in each band since

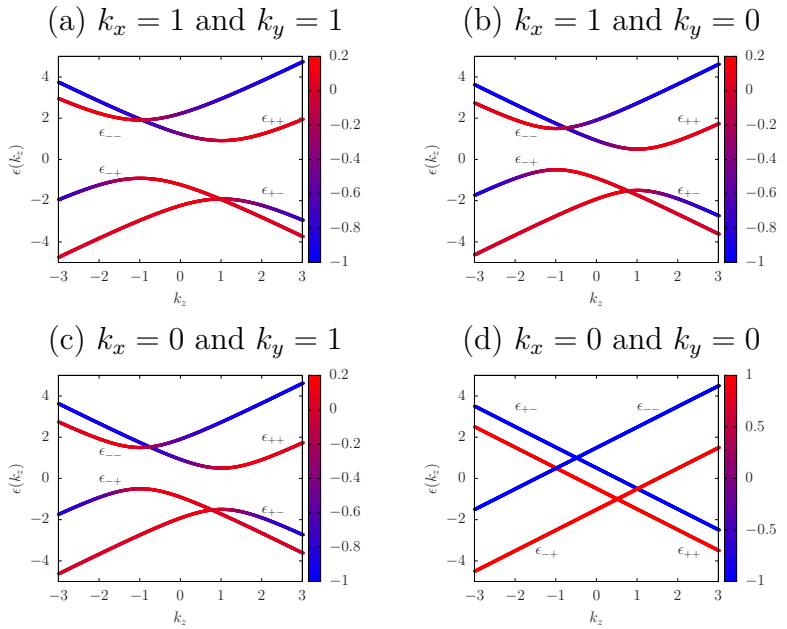

Figure 7 – Dispersion relation ε_{sh} as a function of k_z for TRS and IS broken, where $Q = 1$ and $Q_0 = 0.5$. We also have $v_\perp = v_z = 1$, $k_0 = 1$ and $\mu = 0$. The magnetization $\langle S_z \rangle$ is given by the colormap, where blue is negative and red is positive. Since k_z is our variable, k_x and k_y are fixed parameters that will give us four plot combinations, depending whether it is zero or not. We have (a) $k_x = 1$ and $k_y = 1$, (b) $k_x = 1$ and $k_y = 0$, (c) $k_x = 0$ and $k_y = 1$ and (d) $k_x = 0$ and $k_y = 0$. Note that cases (b) and (c) are equivalent, since the Hamiltonian is symmetric in the xy-plane.

the Hamiltonian is diagonal and the bands of different magnetization touch each other points equivalent to the value of $\pm Q_0$. To make it easier for visualization, lets think about the Hamiltonian in terms of matrix and divide it into two blocks, the upper block is the positive chirality and the bottom block is the negative chirality. Each block can be divided into conduction and valence terms in its diagonal. This way, we can have a picture in mind of how ε_{sh} is divided and we can conclude that the conduction and valence, positive and negative chirality bands are exchanged, ε_{++} and ε_{--} are at the same side while ε_{+-} and ε_{-+} are on the other.

We also have the dispersion relation in terms of k_z, where we break only TRS, preserving IS. As we know, a broken TRS gives the bands a displacement in the horizontal direction. Note that the cases in Fig. 7, 9 and 8, where $\varepsilon_{sh}(k_z)$, are equivalent in terms of $\langle S_z \rangle$, and we can conclude that this term does not depend on the symmetries we are working with, as long as we have Weyl semimetals, in other words, if we break one symmetry we will have the magnetization of the bands. In these three cases, it is clear that the greater the contribution of the fixed momentum the greater the kinetic energy and the distance between valence and conduction bands for each chirality.

We can also do the same study if we keep k_y and k_z as parameters and plot the

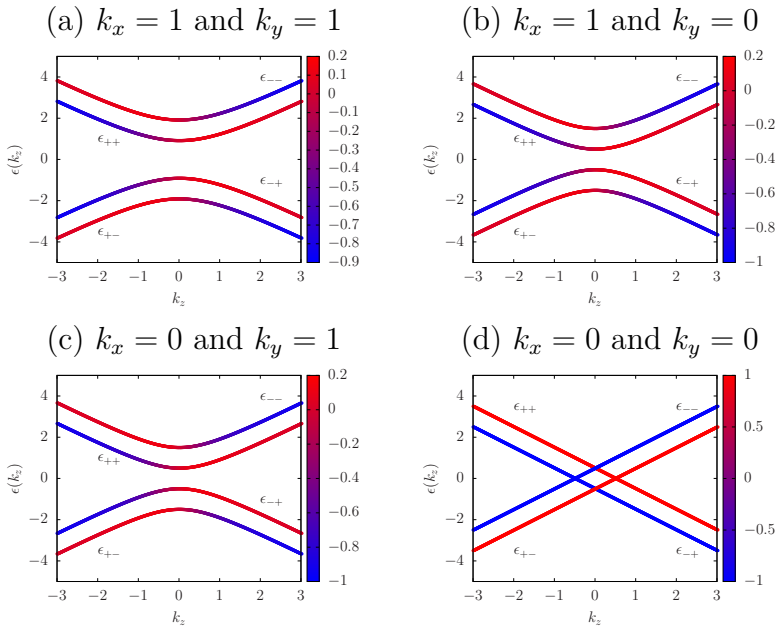

Figure 8 – Dispersion relation ε_{sh} as a function of k_z for TRS preserved and IS broken, where $Q = 0$ and $Q_0 = 0.5$. We also have $v_\perp = v_z = 1$, $k_0 = 1$ and $\mu = 0$. The magnetization $\langle S_z \rangle$ is given by the colormap, where blue is negative and red is positive. Since k_z is our variable, k_x and k_y are fixed parameters that will give us four plot combinations, depending whether it is zero or not. We have (a) $k_x = 1$ and $k_y = 1$, (b) $k_x = 1$ and $k_y = 0$, (c) $k_x = 0$ and $k_y = 1$ and (d) $k_x = 0$ and $k_y = 0$. Note that cases (b) and (c) are identical, since the Hamiltonian is symmetric in the xy-plane. We see a displacement only in the vertical direction, since the IS is broken and TRS is preserved. We also notice that the distance between bands is greater when we have a contribution of both parameters k_x and k_y, and is smaller when we have only one of them.

dispersion relation in terms of k_x that is equivalent to the study where we keep k_x and k_z as parameters and analyze the dispersion relation in terms of k_y. As we already discussed, the model is symmetric for k_x and k_y. For broken TRS and IS, we have the dispersion relation in the x direction. Because of a different set of symmetries due to the choice of the parameters, a different behavior will emerge. Note that, in Fig. 10, even though some cases are similar, they are not equivalent, since the symmetries of the model Hamiltonian are not present like in the previous cases.

Another case would be to preserve IS and break TRS. For this specific case, when we place the parameter $k_z = 0$, we have a degeneracy for the bands of opposite chirality, for valence and conduction bands. Since we choose to plot the dispersion relation in terms of k_x, the plane we are analyzing does not allow us to observe the effects of TRS break when we keep this set of parameters.

For the last case, we have TRS preserved and we now break IS. This is an exotic case where the manipulation of the parameters will give us a small change in the kinetic *gap* for cases (a) and (c), and there will be distinct behavior for the cases (b) and (d), where

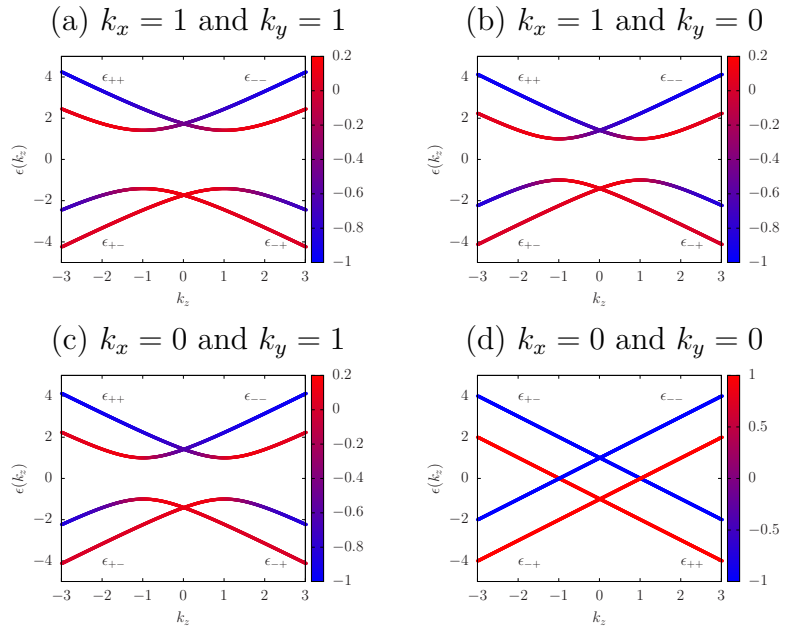

Figure 9 – Dispersion relation ε_{sh} as a function of k_z for broken TRS and IS preserved, where $Q = 1.0$ and $Q_0 = 0$. We also have $v_\perp = v_z = 1$, $k_0 = 1$ and $\mu = 0$. The magnetization $\langle S_z \rangle$ is given by the colormap, where blue is negative and red is positive. Since k_z is our variable, k_x and k_y are fixed parameters that will give us four plot combinations, depending whether it is zero or not. We have (a) $k_x = 1$ and $k_y = 1$, (b) $k_x = 1$ and $k_y = 0$, (c) $k_x = 0$ and $k_y = 1$ and (d) $k_x = 0$ and $k_y = 0$. Note that cases (b) and (c) are identical, since the Hamiltonian is symmetric in the xy-plane. We see a displacement only in the horizontal direction, since the TRS is broken and IS is preserved. We also notice that the distance between bands is greater when we have a contribution of both parameters k_x and k_y, and is smaller when we have only one of them.

the magnetization is zero. It should be emphasized that this is not indeed a gap but only a cut in the dispersion relation, and since we are plotting an hyperfigure [a four-dimensional figure $\varepsilon(k_x, k_y, k_z)$], we should fix some parameters in order to present the following plots, from where this *gap* emerges. Case (d) behaves like case (d) of Fig. 8, although in the present case, the magnetization vanished due to the choice of the parameters and the symmetries we are considering.

This is a brief study on the magnetization behavior for bands where we manipulate symmetries and parameters of the system in order to have different regimes for the bands. This study contributed for the understanding of the momentum in each band, whether it is valence or conduction. We see the change of magnetization, or in other words, the spin and this is in agreement with the literature where we know that the momentum must be conserved (ARMITAGE; MELE; VISHWANATH, 2017).

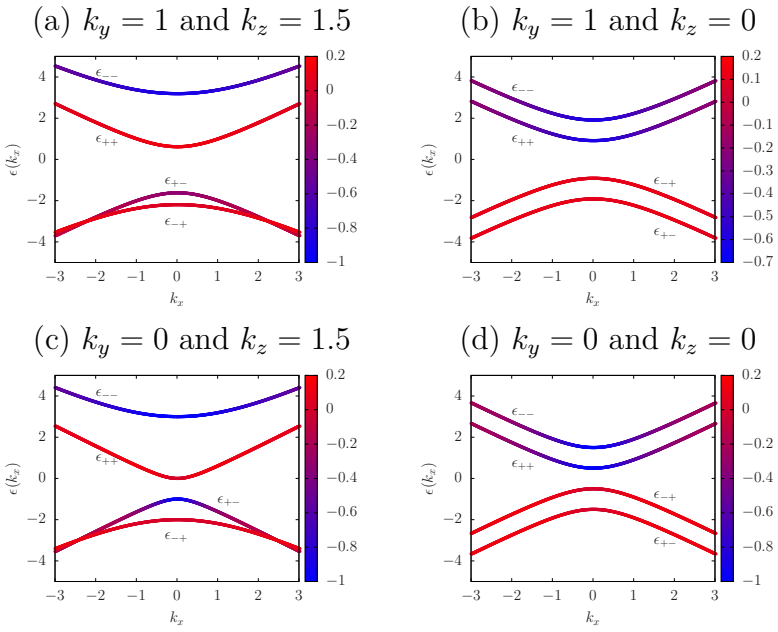

Figure 10 – Dispersion relation in the x direction, where TRS and IS are broken, $Q = 1.0$ and $Q_0 = 0.5$, respectively. We also have $v_\perp = v_z = 1$, $k_0 = 1$ and $\mu = 0$. The magnetization $\langle S_z \rangle$ is given by the colormap, where blue is negative and red is positive. Since k_x is our variable, k_y and k_z are fixed parameters that will give us four plot combinations, depending whether it is zero or not. We have (a) $k_y = 1$ and $k_z = 1.5$, (b) $k_y = 1$ and $k_z = 0$, (c) $k_y = 0$ and $k_z = 1.5$ and (d) $k_y = 0$ and $k_z = 0$.

4.5 A brief Explanation on the cutoff k_c

As you may have noticed, our numerical method depends on the region of the momentum space we consider for our calculations. Our numerical method relies on the integration on the momentum k_x, k_y and k_z, since it is a three-dimensional model. So we have to integrate over this three dimensional momentum space to find the quantum propagator, that in turn will allow us to find the hybridization matrix, as we discussed in 4.3. The cutoff is responsible to tell us the portion of the band we are analyzing. Therefore, if we want to complete description of the problem we should consider the entire band, but that is not possible due to numerical limitations. For this reason, we introduce k_c which is a limitation in our method but that allow us to perform the numerical calculations. In order to know what value or values of k_c we should consider, we compare our method with the literature for some well known case.

When we calculate the host DoS using any k_c, we known that the Weyl system DoS, when we break IS should go to zero in its minimum point. The valence band behaves just like the conduction one, we calculate the two distinct chirality $s = \pm$. We should also consider that our method may not handle well the low energy cases for some very large k_c, also, small ones may not reproduce the physics we are interested to study.

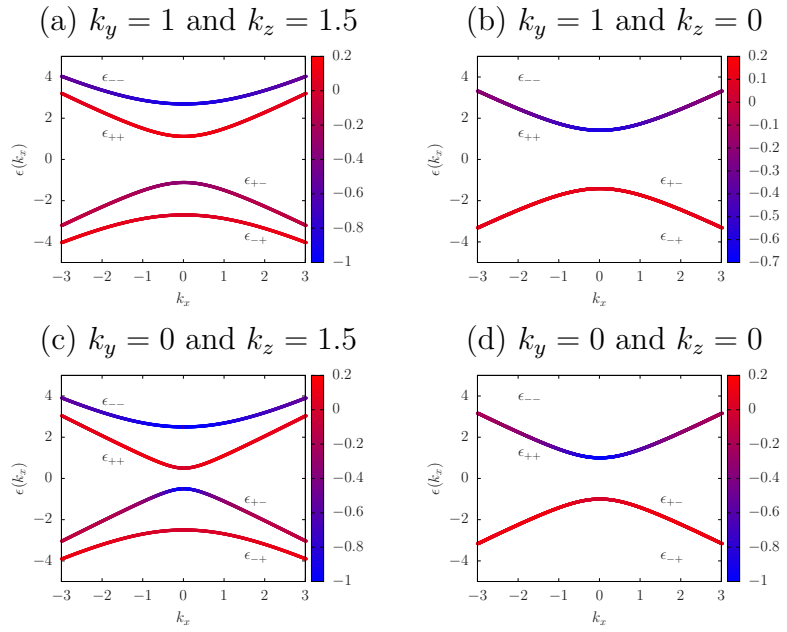

Figure 11 – Dispersion relation in the x direction, where TRS is broken and IS is preserved, $Q = 1.0$ and $Q_0 = 0$, respectively. We also have $v_\perp = v_z = 1$, $k_0 = 1$ and $\mu = 0$. The magnetization $\langle S_z \rangle$ is given by the colormap, where blue is negative and red is positive. Since k_x is our variable, k_y and k_z are fixed parameters that will give us four plot combinations, depending whether it is zero or not. We have (a) $k_y = 1$ and $k_z = 1.5$, (b) $k_y = 1$ and $k_z = 0$, (c) $k_y = 0$ and $k_z = 1.5$ and (d) $k_y = 0$ and $k_z = 0$. Notice the degeneracy in the cases (b) and (d) due to the plane we are analyzing our data and the set of parameters we choose, where $k_z = 0$. For the cases (a) and (c), the magnetization is positive in the conduction band and negative in the valence band. For the cases (b) and (d) for positive chirality we have inverted magnetization, where it is positive in the valence band and negative in the conduction band. While in the negative chirality, the valence band has negative magnetization while the conduction band the magnetization is positive.

We can see in Fig. 13 using (4.5), that increasing k_c does not change significantly the DoS. The distance between the minimum point in DoS increases slightly with the significant increase in k_c. We know that when we break IS, there will be a gap in dispersion relation (ϵ). This gap in ϵ means that we do not have electrons with such energy, and in DoS we see as ρ going to zero. For this reason, we wish to see in Fig. 13 the curve going to zero in ω in Fig.13 as much as possible. This shows us that the optimum value is $k_c = 5$, as we can see in Fig. 13.

In some other tests, we calculate the dispersion relation to understand how it behaves for different values of k_c. There is relation between DoS and dispersion relation given by

$$\rho_n(\epsilon) = \int_{S_n(\epsilon)} \frac{dS}{4\pi^3} \frac{1}{|\nabla \epsilon_n(\mathbf{k})|}. \tag{4.19}$$

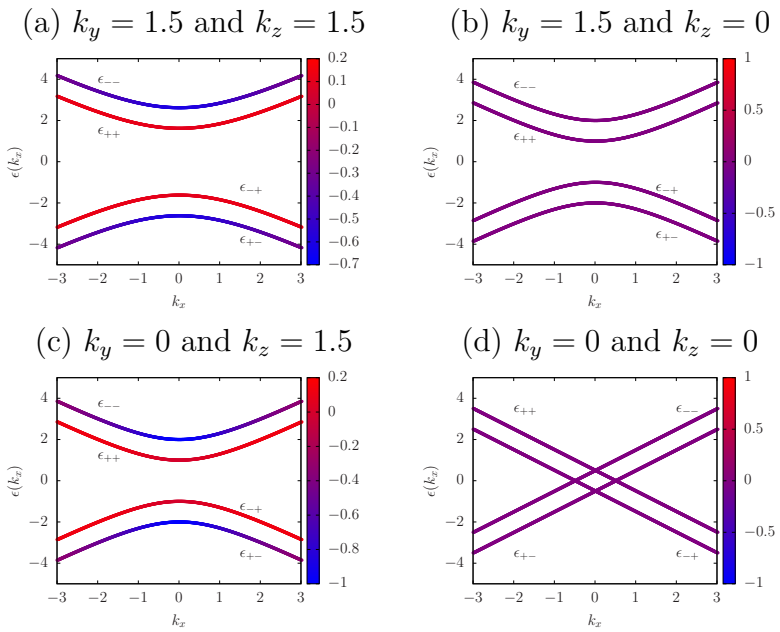

Figure 12 – Dispersion relation in the x direction, where TRS is preserved and IS is broken, $Q = 0$ and $Q_0 = 0.50$, respectively. We also have $v_\perp = v_z = 1$, $k_0 = 1$ and $\mu = 0$. The magnetization $\langle S_z \rangle$ is given by the colormap, where blue is negative and red is positive. Since k_x is our variable, k_y and k_z are fixed parameters that will give us four plot combinations, depending whether it is zero or not. We have (a) $k_y = 1$ and $k_z = 1.5$, (b) $k_y = 1$ and $k_z = 0$, (c) $k_y = 0$ and $k_z = 1.5$ and (d) $k_y = 0$ and $k_z = 0$. Notice that cases (a) and (c) are similar differing only on the distance between conduction and valence bands of same chirality. This is due to the fact that preserving $k_z = 1.5$ in both cases and changing only k_y only changes contribution to kinetic energy of each band. For the case (b) and (d) the magnetization is zero, while in (d) is similar when we keep the same symmetries but analyze the dispersion in terms of k_z.

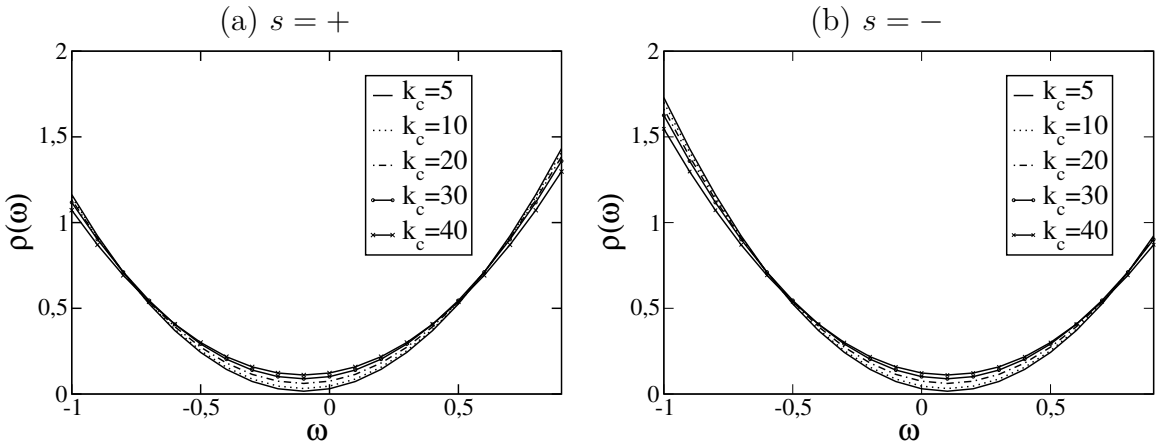

Figure 13 – DoS $\rho(\omega)$ for $k_c = 5$, 10, 20, 30 and 40. The Hamiltonian parameters are $v_\perp = v_z = 1$, $k_0 - 1$, $J = 1$, $\mu = 0$. We also break TRS and IS, $Q = 1$ and $Q_0 = 0.1$, respectively. We use 20 points for each curve. In case (a) the band has positive chirality ($s = +$), while for case (b) we have negative chirality ($s = -$). The valence and conduction bands are degenerate.

The DoS is equivalent to the hybridization function. Despite the fact that the hybridization function we have the products with the matrix $\hat{V}$, it behaves like the DoS. We can conclude that the hybridization matrix is influenced by the choice of k_c. We have seen that, for a small region of $\mathbf{k}$, the dispersion relation continues to exhibit parabolic energy, as the density of states is linked with the inverse of the module of the gradient of the dispersion relation, implying that if the dispersion relation is a plane, that is, a constant, then the gradient will be null, which leads to a singularity in the moment. However, as our dispersion relation remains parabolic for the adopted parameters, we saw that the DoS does not have singularity for certain values of k_c, but this does not prevent us from having cases where the dispersion relation is flat and that the DoS diverges. This will happen for example, when $v_\perp = 0$ or k_x and k_y are zero. In this case, the dispersion relations are planes (showed as lines for our case, since we are plotting only ε as function of only one momentum) and the gradient is zero. We will discuss this behavior in Sec. 6, where we plot some specific cases where some momentum are zero in dispersion relation.

We can conclude that the choice of an optimal value of k_c will allow a better description of the problems we describe in this chapter. For our study, the region considered due to the choice of the cutoff of the band, permitted us to reproduce the well known cases in literature. This is sufficient to ensure the reliability of the results provided from our work. The next natural step of this thesis is to find a method capable of handling this limitation. It would be of great use to find a way to avoid work with the cutoff, this would give us a more complete description of Weyl and Multi weyl systems. After finding the best k_c for our numerical integration method, we keep this value ($k_c = 5$) for all the results presented in this work.

5 Methodology

In this part of the journey we will describe the theoretical approach that led to a numerical method to solve the Kondo problem exactly. We will try to provide a trustworthy description of Weyl and multi-Weyl semimetals ($\mu = 0$) and metals ($\mu \neq 0$) and the methods that allow us to perform calculations and study these materials numerically using the NRG approach. The numerical renormalization group comes from a theory called Renormalization Group (RG) and receives the name, called the Numerical Renormalization Group (NRG). In the following we will give you a brief description of the RG and the NRG methods. Since it is not our propose to give a thorough digression on the method, there is no need for exhaustive and prolix description of something that were already vastly discussed in the literature (GONZALEZ-BUXTON; INGERSENT, 1998; ŽITKO; PRUSCHKE, 2009; BULLA; COSTI; PRUSCHKE, 2008; HEWSON, 1993).

5.1 The Renormalization Group

In the previous chapter we have discussed the treatment of the Kondo effect using perturbation theory, and how problematic it can be. It was shown that a more robust method is necessary to deal with this problem. The north-American physicist Philip Warren Anderson, laureated with the Nobel Prize in 1977, proposed a model Hamiltonian to describe magnetic impurities hosted in metals, called Anderson Impurity Model described by

$$H = \sum_{\mathbf{k},\sigma} \varepsilon_{\mathbf{k}} c^{\dagger}_{\mathbf{k},\sigma} c_{\mathbf{k},\sigma} + \sum_{\sigma} \varepsilon_d d^{\dagger}_{\sigma} d_{\sigma} + U d^{\dagger}_{\uparrow} d_{\uparrow} d^{\dagger}_{\downarrow} d_{\downarrow} + \sum_{\mathbf{k},\sigma} V_{\mathbf{k}} (d^{\dagger}_{\sigma} c_{\mathbf{k},\sigma} + c^{\dagger}_{\mathbf{k},\sigma} d_{\sigma}), \tag{5.1}$$

where $c^{\dagger}_{\mathbf{k},\sigma}$ and $c_{\mathbf{k},\sigma}$ are creation and annihilation operators for conducting electrons in host materials with momentum $\mathbf{k}$ and spin σ, respectively, $d^{\dagger}_{\mathbf{k},\sigma}$ and $d_{\mathbf{k},\sigma}$ are creation and annihilation operators for electrons in the magnetic impurity energy level. The Coulomb repulsion between electrons in the magnetic impurities is U and $V_{\mathbf{k}}$ gives the interaction between host and magnetic impurity, or the hybridization between them. Together with Eq. (5.1), Keneth Wilson, an American theoretical physicist, proposed the *Numerical Renormalization Group* method specifically to solve the Kondo problem. In few words, the idea consists in a recursive rescaling of the Hamiltonian parameters that allow us to avoid the divergences that are present in the Kondo problem. In this problem, and many others presented in physics and science in general, the many-body interactions take place in a broad range of the energy scale, there are very fast energetic particles and also low energetic ones in the same system. The conduction electrons of the host system in

question vary from several electron-Volts (eV) to values near the scale of energy $10^{-4}eV$, the equivalent to few Kelvin. The Kondo effect occurs at very low energy scale, however all energy scales matter equally. The arising question is then how to come up with a method that treats the infrared limit and also takes into account the influence of high energy scales that also influences the low-temperature behavior of the system. The crucial idea of this method consists of, instead of considering the fine details of the model for high energy, like the conduction band width, we go all the way to the lower energy scales by considering the contributions of these small energies and grouping them in intervals and analyzing their contributions separately. It is a rescaling in energy to get a specific regime [see Fig. 14(a)]. This way, in a perturbative approach of some kind, we take into account the high energy effects. This is possible because the parameters of the Hamiltonian can be reproduced at smaller scales compared to the conduction band cutoff D, so we can consider smaller energy regimes of the system until we reach even lower scales also compared to D (We should emphasize that all scales are set based on D, the band cutoff). For example the Kondo regime, the model can be described by the fixed point of this Hamiltonian where the model tends to and we say it belongs to the same *Universality Classes*. These collections of properties that share this invariant property has a specific energy scale. Although, to be more precise, *Universality class* are defined by a set of critical exponents in the thermodynamical limit. This *Universality* implies that the behavior of these systems at low energies, consequently, low temperature behaviors are independent of the fine details of the high temperature model.

The *Renormalization Group* can be applied to a model to attain its *Universalities* of the low energy scales, doing so, we rescale the energy through a reduction in the conduction band width, $D \to D' = D/\lambda$, where $\lambda > 1$. After that, we integrate over the degrees of freedom in the energy interval $[D/\lambda, D]$. This will change the Hamiltonian, $H(D) \to H'$. We then rescale the energy back, such that $\omega = \lambda\omega'$ (where ω is the variation of energy in the band interval $[-D, D]$). The new Hamiltonian can be written as $H(D/\lambda) = \lambda H'$. This rescaling method is performed successively when we obtain $H(D)$, back to the top of the integration limit.

5.2 The Numerical Renormalization Group (NRG)

Motivated by the perturbative RG, the NRG is a non-perturbative numerical method proposed by the American physicist Kenneth Wilson to solve the Kondo problem exactly. As a numerical method, it solves the problem through an iterative procedure using the RG theory.

The NRG is applied to a system in order to diagonalize it exactly with a numerical approach. As it solves the Kondo problem, the NRG performs the study of a quantum

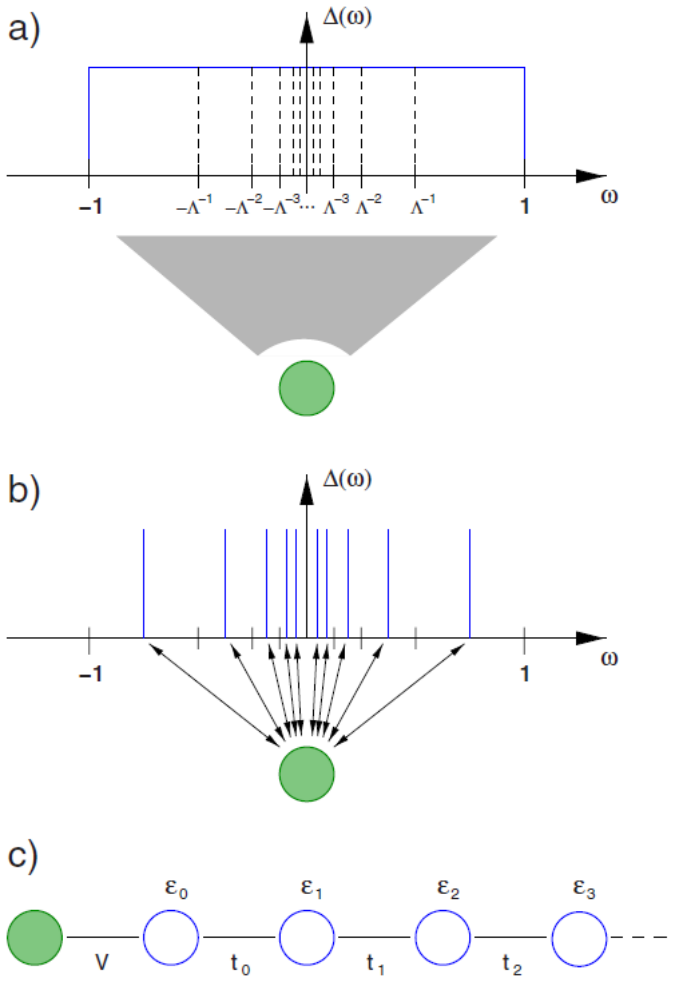

Figure 14 – Initial steps of the NRG method illustrated for the single-impurity Anderson model in which an impurity (green circle) couples to a continuous conduction band via the hybridization function $\Delta(\omega)$ [in our case $\Gamma(\omega)$]. (a) A logarithmic set of intervals is introduced through the NRG discretization parameter Λ. (b) The continuous spectrum within each of these intervals is approximated by a single state. (c) The resulting discretized model is mapped onto a semi-infinite chain where the impurity couples to the first conduction electron site via the hybridization parameter V while ϵ_n and t_n are the parameters of the tight-binding Hamiltonian (BULLA; COSTI; PRUSCHKE, 2008).

mechanical impurity with some degrees of freedom coupled to its host. The impurity interacts with electrons in the material. It is worth mentioning that the NRG calculations do not consider the interaction between conduction electrons.

To perform our numerical analysis, we will look mainly at the impurity magnetic moment $k_B T\chi_{\rm imp}(T)$ and the local density of states $\rho(\omega)$ that reveal most of the relevant features of the Kondo effect. Here, $\chi_{\rm imp}(T)$ is the impurity contribution to the total magnetic susceptibility defined as $\chi_{\rm imp}(T) \equiv \chi(T) - \chi^{(0)}(T)$, where $\chi(T) - \chi^{(0)}(T)$ are the magnetic susceptibilities calculated with and without the impurity, respectively [see

discussion in Ref. (BULLA; COSTI; PRUSCHKE, 2008)], and $\rho_s(\omega)$ can be defined using the diagonal elements of the impurity local Green's function matrix (4.8) as $\rho_s(\omega) = -\frac{1}{\pi}\mathrm{Im}[\hat{G}_{\mathrm{imp}}(\omega + i0^+)]_{ss}$. Within the NRG approach, $\rho_s(\omega)$ is calculated via Lehman representation $\hat{G}_{\mathrm{imp}}(\omega+i0^+)_{ss}$ using the many-body spectrum readily available in standard NRG calculations, where s is the impurity spin quantum number. For more details, see thorough discussion in Ref. (ŽITKO; PRUSCHKE, 2009).

The basic procedure of the NRG method consists first to dividing the energy of the hybridization function $\Gamma(\omega)$ of the host into logarithmic intervals (the Γ function is the responsible for the interaction between impurity and host and will be extensively explored in further sections). The best way to do it is using a logarithmic discretization, that consists in a division of the band energy in logarithmic sections, although there are many other ways to divide the continuous interval. The explanation for choosing the logarithmic discretization is that for a finite system the splitting of energies is inversely proportional to the system size, since the system size is of the order of some microns, the number of sites is extremely big ($\sim 10^6$ for example). The logarithmic method reduces the problem in which the low-energy resolution now depends exponentially on the number of sites of the discretized model, a chain of atoms beginning with the impurity in the first site and each site corresponds to an energy scale in the problem, usually called NRG shell, as shown in Fig. 14-c. The next step consists in mapping the model that was discretized onto a semi-infinite chain. Then we diagonalize iteratively this chain and the final step is to analyze and treat the output data such as band structure, matrix elements, spectral function and local density of states.

In Fig. 14, we show a pictorial scheme of how the NRG works. We have a continuous host in an interval $[-1, 1]$. The NRG discretization parameter, $\Lambda > 1$, defines a set of logarithmic discretization displacement points $\pm\Lambda^{-n}$, where $n = 0, 1, 2, \cdots$ and a corresponding set of intervals. The continuous case in Fig. 14(a) is then approximated by a single state in each interval, Fig. 14(b). Then we map it in a semi-infinite chain as shown in Fig. 14(c), where the impurity is the green circle and corresponds to the first site of the chain. It turns out that the hopping matrix elements decreases exponentially with increasing distance from the impurity since we consider a logarithmic discretization, $t_n = \Lambda^{-n/2}$ (BULLA; COSTI; PRUSCHKE, 2008).

The Hamiltonian of the general impurity model inserted in a host, is composed of three parts, the impurity part H_{imp}, the host part H_0 and the interaction between those two, that we call the hybridization Hamiltonian H_V. This Hamiltonian was explicitly shown in Eq. (5.1) in a more general form and can be simply written as

$$H = H_{imp} + H_0 + H_V. \tag{5.2}$$

We will go into the details of our Hamiltonians in the next sections. But for now, this is the general form of the Hamiltonian and will be used as the initial step for the calculations of the NRG. The information of our system is all stored in this Hamiltonian. After that, we calculate the hybridization matrix $\Gamma(\omega)$, whose matrix elements will be the input data for the NRG to provide us with the required information such as LDOS and Kondo temperature, to name a few. This hybridization matrix function contains the H_V part of the Hamiltonian responsible for the interaction of the host and the impurity. To calculate the hybridization function $\Gamma(\omega)$, we should find the self-energy, which is the scattering rate for single-particle excitations with energy $|\omega|$, of the propagator related to the Hamiltonian we want to calculate, in our case Eq. (4.5). The self energy was discussed in Sec. 4.3 and $\Gamma(\omega)$ is minus the imaginary part of this quantity, as shown in Eq.(4.15). The product between interaction matrix $V_{\mathbf{k}}$, the host propagator related to the Hamiltonian and the complex conjugated interaction matrix $V_{\mathbf{k}}^{\dagger}$ is equivalent to $\Gamma(\omega)$, which can be written as

$$\hat{\Gamma} = \hat{V} \cdot \hat{G}_{\mathbf{k}}^{\text{host}}(\omega) \cdot \hat{V}^{\dagger}. \tag{5.3}$$

With this in hand, we have the complete influence of the conduction band over the magnetic impurity.

The NRG calculations perform a discretization over the reciprocal space of the conduction band. The method does a series of calculations at logarithmic intervals inside the band being considered. In order to calculate physical quantities such as magnetization and entropy, NRG provides the energies and states of the Hamiltonian we are working with.

From the model Hamiltonian (4.5), we derive a Green function of the host, given by

$$\hat{G}_{\mathbf{k}}^{host}(\omega) = \Big[\Big(\omega + i\eta\Big)\mathbb{1} - \mathcal{H}_{\mathbf{k}}\Big]^{-1}. \tag{5.4}$$

From this expression, we can calculate, using $\hat{V}$, the interaction matrix (4.7), we derive the hybridization function Eq. (5.3). We should emphasize that the total hybridization function is a combination of advanced Γ^{+} and retarded Γ^{-} hybridization functions, given by

$$\Gamma(\omega) = \frac{i}{2}\Big[\Gamma^{+}(\omega + i\eta) - \Gamma^{-}(\omega - i\eta)\Big]. \tag{5.5}$$

We can also calculate the magnetic impurity DoS via the steps that follows

$$\rho_{imp}(\omega) = -\frac{1}{\pi}\,\text{Im}\left[\hat{G}_{\mathbf{k}}^{imp}(\omega)\right], \tag{5.6}$$

where the impurity propagator is associated to the self-energy that gives the interaction between the host and the impurity as

$$\hat{G}^{imp}_{\mathbf{k}}(\omega) = \Big[(\omega + i\eta)\mathbb{1} - U - \hat{\Gamma}(\omega)\Big]^{-1}, \tag{5.7}$$

where $\hat{\Gamma}$ was previously defined by Eq. (5.5) and Eq. (5.3). Notice that they depend on $\hat{G}^{host}_{\mathbf{k}}(\omega)$ that is described by Eq. (5.4). With all these tools, the impurity DoS can be calculated.

The physical properties can be derived from the states given by the NRG method. Entropy is defined by

$$S = K_B T \frac{\partial ln(Z)}{\partial T} \tag{5.8}$$

where Z is the partition function. Or, in terms of the states, we can write

$$S = \frac{1}{T}\sum_n \langle n|S_z|n\rangle e^{-\beta E_n}, \tag{5.9}$$

where $\beta = 1/K_B T$. The states $|n\rangle$ and the energies E_n are obtained from the NRG calculations. The magnetic impurity entropy is given by the difference between the total and host entropies, as follows

$$S_{imp} = S_{total} - S_{host}. \tag{5.10}$$

With the eigenvalues and eigenvectors, we can also calculate the magnetic susceptibility as

$$\chi(T) = \beta\Big(\langle S_z^2\rangle - \langle S_z\rangle^2\Big), \tag{5.11}$$

and the impurity susceptibility can be written as

$$\chi_{imp}(T) = \chi_{total}(T) - \chi_{host}(T). \tag{5.12}$$

The NRG calculation details are omitted but the main method is presented here. Because the NRG can solve the Kondo problem exactly allowing us to perform an accurate description of our problem (the pseudogap Kondo in MWSM and MDSM), it is a useful tools for this work that can only be possible because of this numerical method.

5.3 A Brief Look at the Numerical Steps

To understand the steps we use to develop the numerical method, it is of great use to describe how we go from a theoretical Hamiltonian that contains the information of our

system until we reach the NRG method. After this part, all we have left is to treat the data that this systematization provides.

From the model Hamiltonian (4.5), that will be discussed in the next section, we calculate the propagator, also known as the Green function as

$$\hat{G}^{\text{host}}_{\mathbf{k}}(\omega) = [\omega \mathbb{1} - \mathcal{H}_{\mathbf{k}}]^{-1} . \tag{5.13}$$

Here, $\mathcal{H}_{\mathbf{k}}$ is the system Hamiltonian (4.5). From this Green's function, we use the hybridization matrix $\hat{V}$, the one responsible for the interaction between the magnetic impurity and the host material, which was presented as Eq. 5.3.

Since the Green's function (5.13) is a 4×4 matrix for the Weyl host and $\hat{V}$ is a 2×4 matrix, the outcome Γ matrix is a 2×2 matrix, which is not true for a metal. This matrix is the entry data for the NRG calculation.

The fist goal was to find the best candidate to describe the physical problems we want to treat, in our case we want to connect our host material with a magnetic impurity using the NRG to calculate main physical quantities such as DoS and spectral function revealing features of the Kondo effect. Once we had the Hamiltonian in hand (remember that it is a theoretical model) we are able to follow the steps describe above and obtain a systematic calculation of this interaction.

Our NRG calculations were obtained using the well-known open source NRG Ljubljana code (ŽITKO; PRUSCHKE, 2009), using $\Lambda = 2.5$, keeping a maximum number of states $N_s = 2000$ at each iteration and z-averaging $N_z = 4$. The NRG flow is truncated at a lowest energy $E_{\text{min}} = 10^{-12}$. This choice is good enough to access the main features of the Kondo regime with great accuracy. Finally, the impurity density of states ρ_s was calculated at $T = 10^{-10}$ (the temperature unit is related to D).

6 Numerical results

Having discussed the Kondo effect and its features in relevant physical quantities using NRG, we are now in position to tackle the Kondo effect in multi-Weyl semimetals. Akin to what happens in pseudogap Kondo systems, we will show that Kondo depends strongly on the parameters of the system. Some of those, such as J and μ are well established in literature, however for cases like multi-Weyl semimetals, Kondo is present due to the configuration of the model Hamiltonian and is the contribution of this work for this area of research. We are going to explore the effects of each parameter such as the symmetries and chemical potential and its contributions for the emergence of Kondo physics.

To obtain the numerical results, we set $D = 1$ as the ultraviolet energy cutoff for all the calculations which follows. Moreover, we set the model parameters $v_\perp = v_z = k_0 = 1$. For simplicity, we also set the fundamental Boltzmann and Plank constants $k_B = \hbar = 1$. We will fix the impurity-related parameters $V = 0.12625$, $U = 0.2$ and $\varepsilon_d = -U/2$. You may ask yourself why there is such a simple choice for the velocity constants but a peculiar one for the coupling strength (or hybridization strength). There is nothing special with the specific choice of the coupling strength V here. It just renders $\Gamma_\uparrow(D) = \Gamma_\downarrow(D) = 0.1$, which in combination with $U = 0.2$ and $\epsilon_d = -U/2$ (corresponding to the particle-hole symmetric point of the impurity Hamiltonian) provides us with T_K much smaller than D, U, and Γ_s for any regime considered in this work. This prevents the system from entering in a mixed-valence regime. It is worth mentioning that along with the specific values of the set of parameters together with $V = 0.12625$ we reproduced Fig. 1 of (LI et al., 2019). We first established the particle-hole parameters U and ε_d and then tuned the coupling strength until we reach the referred case of the article.

6.1 Multi-Dirac node fermions: $Q = Q_0 = 0$

Let us start by studying the regime of $(Q, Q_0) = (0, 0)$, in which the Hamiltonian (4.5) is invariant under TRS and IS (note that we do not have a Weyl system for this case since we preserve both symmetries). The Hamiltonian then describes the aforementioned multi-Dirac node materials (YANG; NAGAOSA, 2014; YU et al., 2015; WU, 2019). For $\mu = 0$ and $\mu \neq 0$ it corresponds to semimetal and metal, respectively. The energy bands and hybridization functions for this case are shown in the first column of Fig. 6. For $J = 1$ the host corresponds to a four-band Dirac semimetal (for $\mu = 0$) exhibiting two copies of Dirac cones. This renders a hybridization function that behaves as $\Gamma(\omega) \equiv \Gamma_\uparrow(\omega) \sim |\omega - \mu|^2 = \Gamma_\downarrow(\omega)$ (since TRS is preserved). For $J = 2$ and 3, the bands are distorted

around $\mathbf{k} = 0$. Note that, while $\varepsilon(0, 0, k_z) \sim |k_z|$ the dispersion is no longer linear with k_x or k_y. The hybridization function behaves as $\Gamma(\omega) \sim |\omega - \mu|$ and $\Gamma(\omega) \sim |\omega - \mu|^{2/3}$ (for $J = 2$ and $J = 3$, respectively). These results are consistent with the prediction that $\Gamma(\omega) \sim |\omega - \mu|^{2/J}$ as $\omega \to 0$ for a generic J (BERA; SAU; ROY, 2016; ROY; GOSWAMI; JURIČ, 2017).

The Kondo physics emerging from this class of hybridization functions is well understood as it has been thoroughly investigated previously in a generic context, namely the so-called pseudogap regime (WITHOFF; FRADKIN, 1990). Indeed, the Anderson and Kondo models for a pseudogap density of states $\rho(\omega) \propto |\omega|^r$, where $r = 2/J$, presents a rich quantum phase diagram extensively studied (INGERSENT; SI, 2002; FRITZ; VOJTA, 2004; FRITZ; FLORENS; VOJTA, 2006; CHENG et al., 2017; BULLA; PRUSCHKE; HEWSON, 1997; MITCHELL et al., 2013; KOLLER; HEWSON; MEYER, 2005) [remember that $\Gamma(\omega) \propto \rho_{\text{host}}(\omega)$]. Numerical and perturbative renormalization group calculations shown that the fixed points structure of the pseudogap Anderson/Kondo systems are radically distinct for $r < 1$ and $r > 1$, suggesting $r = 1$ as the upper-critical "dimension" of the problem in the RG sense (INGERSENT; SI, 2002; FRITZ; VOJTA, 2004). For completeness, here we present the results we have obtained for these three regimes when $J = 1, 2$, or 3. From a theoretical point of view, cases of $J > 3$ are interesting as they render $r \leq 1/2$, leading to anomalous Kondo screenings (GONZALEZ-BUXTON; INGERSENT, 1998). It has been shown, however, that Weyl materials with $J > 3$ are not topologically protected (FANG et al., 2012). Therefore, these cases are not considered here. The results for $J = 1$, which corresponds to $r = 2$, are summarized in Fig. 15.

In Ref. (VOJTA; FRITZ; BULLA, 2010), the authors have shown that the Kondo screening in this case is influenced by the electron-hole asymmetry of the pseudogap density of states. Here, the electron-hole asymmetry of the multi-Dirac/Weyl hosts is controlled by the chemical potential μ, resulting in significant changes in the low-energy physics in comparison with the electron-hole symmetric case ($\mu = 0$). This is shown in Fig. 15(a) that presents us with $\Gamma(\omega)$ vs ω for various values of μ. Note that the hybridization function vanishes quadratically at $\omega = -\mu$, which results in a finite hybridization function at $\omega = 0$. This is why for $\mu = 0$ there is no Kondo peak, as seen in Fig. 15(b) (black line). Note also that as $\Gamma(0)$ increases with $|\mu|$ the system becomes metallic, resulting in the emergence of the Kondo peak (note the sharp peaks for $\mu = -0.15$ and $\mu = -0.2$). The finite Kondo temperature (T_K) in this case is known in the literature (HEWSON, 1993; MITCHELL; FRITZ, 2015b). The right inset of Fig. 15(b) shows the evolution of $\rho_s(0)$ (the height of the impurity density of states) with $|\mu|$. Observe that the Kondo peak starts increasing very rapidly for $|\mu| \approx 0.1$. For very small $|\mu|$, although finite, T_K is smaller than T (the temperature at which ρ_s is calculated). The maximum value of $\rho_s(0)$ for $|\mu| \approx 0.16$ suggests the complete onset of the Kondo screening when T_K becomes larger than T, after which the broadening of the Kondo resonance is more pronounced.

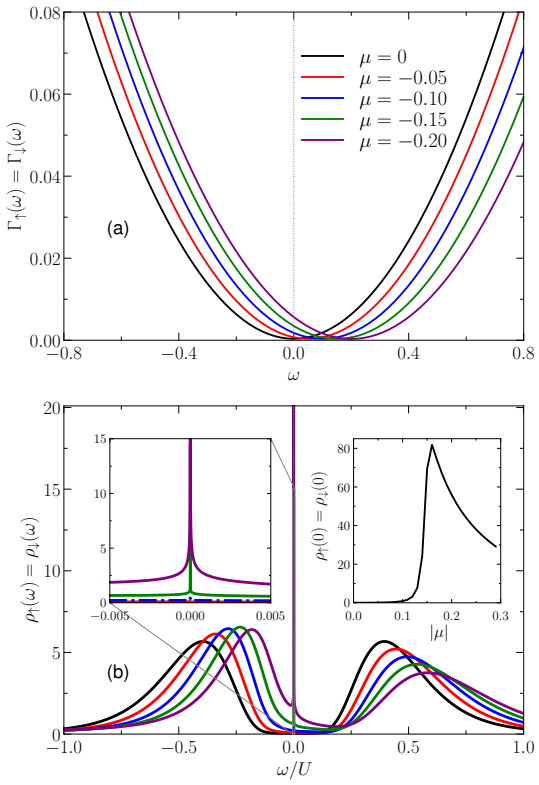

Figure 15 – Hybridization function (a) and impurity density of states ρ_s ($s =\uparrow,\downarrow$) (b) of a Dirac system transitioning from semimetal ($\mu = 0$) to a metal ($\mu \neq 0$) as a function of ω for $J = 1$ and for different values of μ. The left inset of (b) shows a zoom of the region about $\omega = 0$, while the right inset shows the height of the peak, $\rho_s(0)$, as a function of $|\mu|$.

The results for $J = 2$ and $J = 3$ ($r = 1$ and $r = 2/3$) are shown in Figs. 16 and 17, respectively, showing the same quantities plotted in Fig. 15. Note that the results for the three values of J are qualitatively equivalent. This equivalence is consistent with the predictions of Ref. (CHENG et al., 2017) that identifies all cases of $r > 1/2$ as belonging to the same class of pseudogap Kondo screening. Note, however that for larger values of J the Kondo peaks are broader for a fixed value of μ. This can be understood by noticing that for a given value of μ and any $\omega \neq \mu$, $\rho_{\rm host}(\omega) = |\omega - \mu|^{2/J}$ is larger for larger J. Hence, the impurity is more strongly hybridized with the host material for larger J. It is also noteworthy that the value of the chemical potential below which $\rho_s(0)$ drops to zero is smaller for larger J. We will come back to this point below.

To conclude this section, in Fig. 18(a), 18(b), and 18(c) we show the impurity magnetic moment, $k_B T \chi_s$ as a function of temperature for $J = 1$, $J = 2$, and $J = 3$, respectively, and various values of μ. Note that for all J and $\mu = 0$ the magnetic moment remains finite all the way to $T \to 0$, confirming the doublet ground state, a characteristic of the LM fixed point. However, for $\mu \neq 0$, it drops to zero when $T \to 0$, which is consistent with the singlet Kondo ground state, the strong coupled fixed point. Figure 18(d) shows

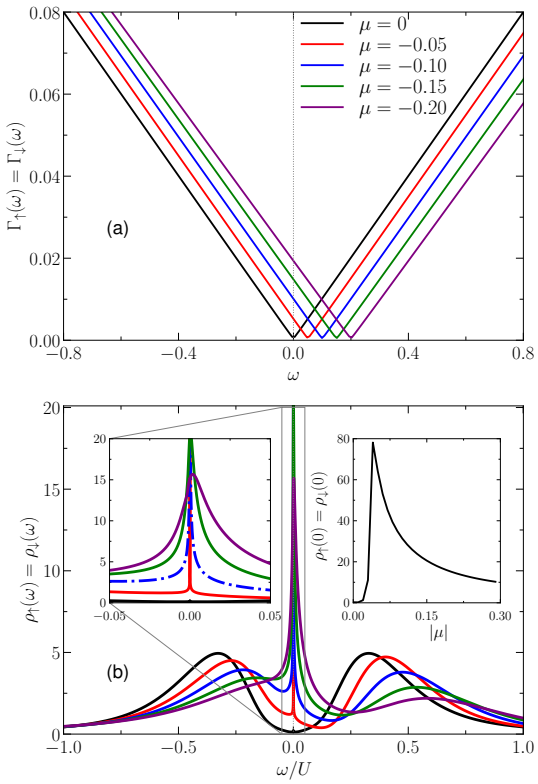

Figure 16 – Hybridization function (a) and impurity density of states ρ_s ($s = \uparrow, \downarrow$) (b) as a function of ω for $J = 2$ and for different values of μ. The left inset of (b) shows a zoom of the region about $\omega = 0$, while the right inset shows the height of the peak $\rho_s(0)$, as a function of $|\mu|$.

T_K as a function of μ for the three values of J[1]. Note that T_K becomes vanishingly small as $|\mu| \to 0$ for all three values of J. When $|\mu|$ increases the curves tend to coincide with each other, which is better observed for $J = 2, 3$. This is an expected behavior since there are two regions along ω within which the hybridization functions, $\Gamma(\omega)$, for different J have similar values, see lower panel in the left column of Fig. 6. Interestingly, the values of $|\mu|$ for which T_K crosses T ($= 10^{-10}$) agree fairly well with those at which $\rho_s(0)$ is maximum in the insets of Figs. 15(b), 16(b) and 17(b), confirming that, indeed, $\rho_s(0)$ vanishes as $|\mu| \to 0$ because T_K becomes smaller than T.

The physical explanation for when $k_B T \chi_s$ goes to zero is that the Kondo singlet is formed and the impurity's magnetic moment vanishes. In other words, the impurity has a total magnetic moment and the conduction electrons in host material surrounds the impurity in order to cancel its total magnetic moment, forming the Kondo singlet. This cloud of carriers around impurity's magnetic moment occurs for lower temperatures for $J = 2$ and even lower for $J = 3$, meaning that the hybridization between conduction carriers of host material and impurity is stronger for greater values of J.

[1] The Kondo temperature is extracted from the magnetic moment, following Wilson criteria $k_B T_K \chi_{\rm imp}(T_K) = 0.07$ (KRISHNA-MURTHY; WILKINS; WILSON, 1980).

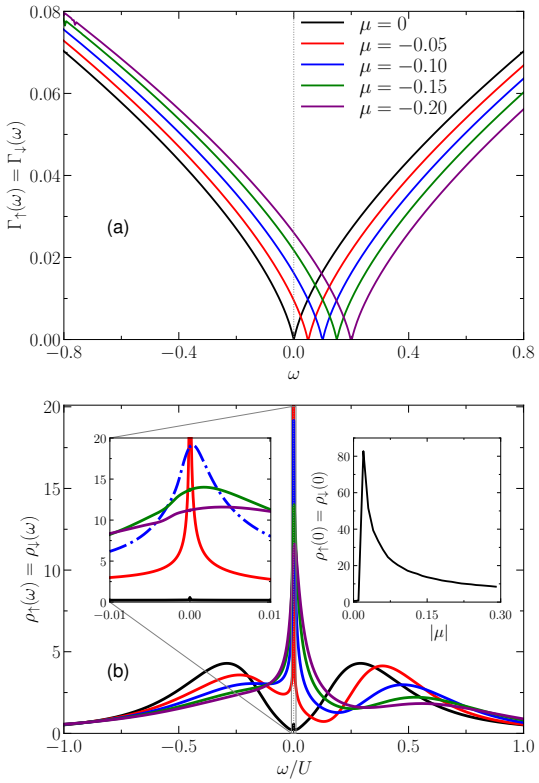

Figure 17 – Hybridization function (a) and impurity density of states (b) as a function of ω for $J = 3$ and for different values of μ. Left inset of (b) shows a zoom of the region about $\omega = 0$, while right inset shows the height of the peak, $\rho_s(0)$, as a function of $|\mu|$.

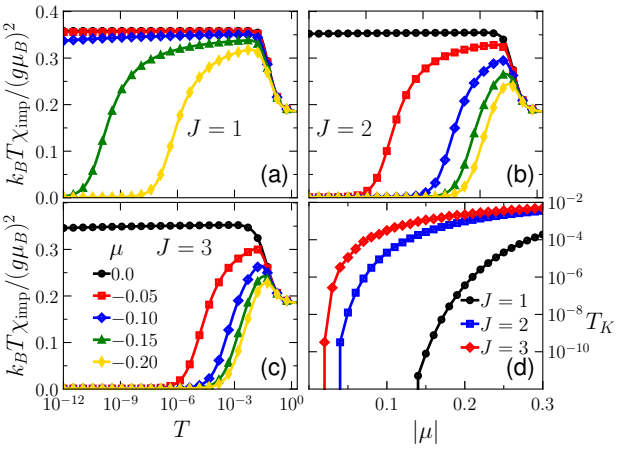

Figure 18 – Impurity magnetic moment for $J = 1$ (a), $J = 2$ (b), and $J = 3$ (c) and various values of μ. (d) Kondo temperature as a function of μ for different values of J. Other parameters are $Q = Q_0 = 0$.

6.2 Multi-Weyl node fermions: $Q \neq 0$ or $Q_0 \neq 0$

Up to now we have considered situations in which the system exhibits both TRS and IS invariance. Let us now focus on the Weyl fermions, obtained when at least one of these symmetries is broken.

6.2.1 Broken TRS multi-Weyl node semimetal ($Q \neq 0$)

Here we analyze the situation where only TRS is broken by keeping $Q_0 = 0$. The energy bands and hybridization function for this case are shown in the second column of Fig. 6, where we used the notation $(Q, Q_0) = (-0.1, 0)$.

The effect of breaking TRS in the energy bands is to shift the nodes along k_z. We should note that the conduction and valence energy bands have opposite spin polarization. As a result, since here we have assumed that the spins of the impurity couples equally to all bands of the host material, at a given value of μ the spin splitting of the hybridization functions vanishes upon integration over the entire momentum space. In our approach, the introduction of the momentum cutoff k_c induces a small spin splitting in the hybridization function for a finite Q.

The polarization $\Gamma_\uparrow - \Gamma_\downarrow$ of the hybridization function is shown in Fig. 19(a) for $J = 1$, $\mu = -0.2$, and several values of Q. Observe that it depends on ω and vanishes at $\omega = -\mu$. This is quite different from that obtained in Ref. (LI et al., 2019) in the context of magnetic graphene, in which $\Gamma_\uparrow(\omega)$ and $\Gamma_\downarrow(\omega)$ vanish at different energies, rendering a full polarization of the hybridization function. Here, full polarization should be absent and is indeed very small. Nevertheless, it is enough to induce a visible spin splitting in the impurity density of states. In real systems, integration over the well defined first Brillouin zone should naturally induce spin splitting in the hybridization function. This can be confirmed by adopting a more realistic model for the multi-Dirac/Weyl node host material. Moreover, spin-dependent coupling of the impurity orbital to the host bands can also contribute to spin polarization of the hybridization function. This important improvement in the model is beyond the scope of the present work and will be presented in a future publication.

The spin resolved LDOS is shown in Fig. 19(b) (for spin $\uparrow$) and Fig. 19(c) (for spin $\downarrow$) for $J = 1$. Interestingly, despite the relatively large spin splitting of the LDOS, the suppression of the Kondo peak is slow as Q increases as shown in Fig. 19(d). The spin splitting in the LDOS induces a sizable magnetization $\langle S_z \rangle$, shown in Fig. 19(e). For $J = 2$ and $J = 3$, the spin polarization is vanishingly small and is not observed in our calculations [see red and blue curves in Fig. 19(e)]. Moreover, the Kondo temperature is larger for these cases, making the Kondo screening more robust against TRS breaking. A change $Q \to -Q$ in the above leads to opposite polarization in the hybridization function

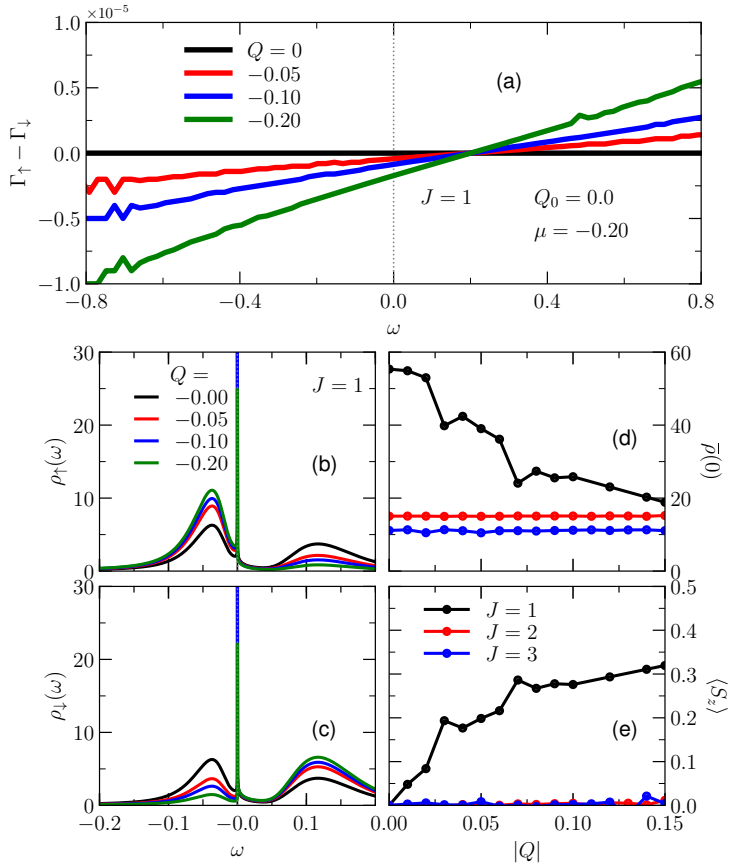

Figure 19 – (a) Splitting of the hybridization function for several values of Q for a fixed chemical potential $\mu = -0.2$. Impurity density of states for spin *up* (b) and *down* (c) for the same values of Q as in panel (a). (d) height of the Kondo peak averaged over spins $[\bar{\rho}(0) = [\rho_\uparrow(0) + \rho_\downarrow(0)]/2$ vs Q for $\mu = -0.2$. (e) $\langle S_z \rangle$ vs $|Q|$ also for $\mu = -0.2$. In all panels $Q_0 = 0$ and J=1.

with identical effect in the Kondo screening.

6.2.2 Broken IS multi-Weyl node semimetal ($Q_0 \neq 0$)

The situation is radically different for finite Q_0. The hybridization function, $\Gamma(\omega)$, is always finite even for $\mu = 0$, as shown in the lower panel of the third column of Fig. 6. Consequently, the system can exhibit Kondo screening for any chemical potential μ. The results we present in this section were not yet explored in scientific community and therefore is our major contribution in this area of study.

Figure 20(a) shows the hybridization function as a function of ω for $J = 1$, $\mu = 0$, and various values of Q_0. Note that the parabolas are shifted upwards and becomes slightly flatter as Q_0 increases[2]. The progressive enhancement of the hybridization function at

[2] It has been found in Ref. (LÜ et al., 2019) that the host density of states behaves as $\rho_{\text{host}}(\omega) \sim |(\omega+\mu)^2 + Q_0^2$ for $J = 1$ and and $\rho_{\text{host}}(\omega) \sim |\omega + \mu + Q_0|^{2/J} + |\omega + \mu - Q_0|^{2/J}$ for $J = 2, 3$.

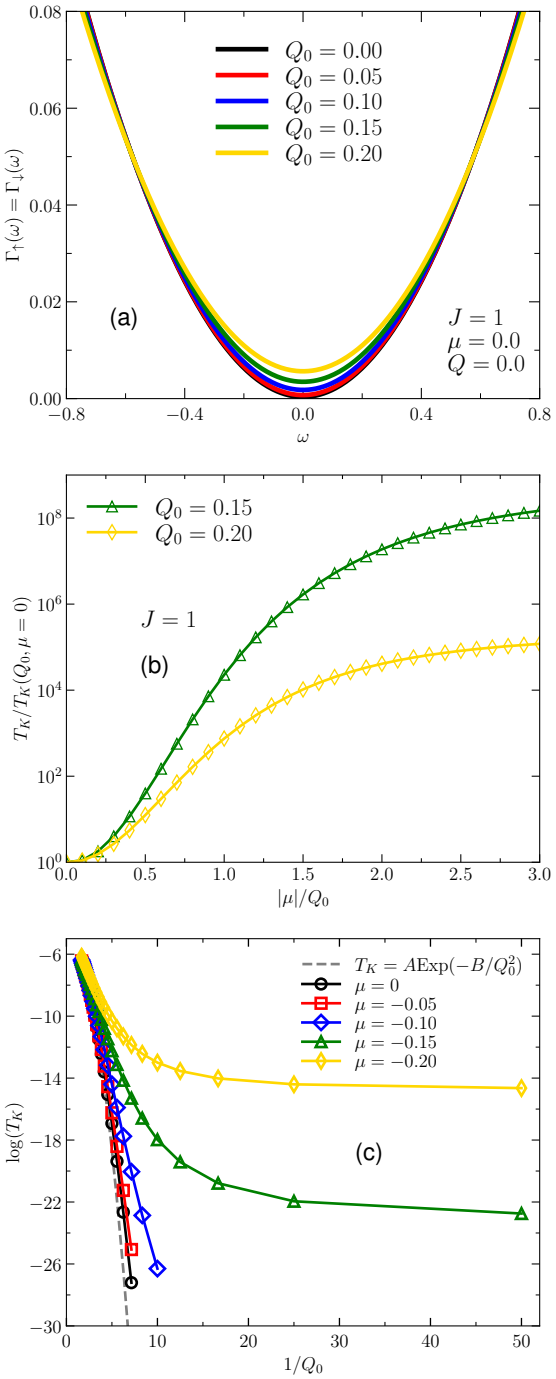

Figure 20 – (a) Hybridization function vs energy for $J = 1$ and various values of Q_0. (b) $T_K(Q_0, \mu)/T_K(Q_0, \mu = 0)$ as a function of μ/Q_0, for different values of Q_0. (c). Kondo temperature vs Q_0^{-1} for various values of μ. Here, $Q = 0$ for all panels.

$\omega = 0$ as Q_0 increases provides the condition for the Kondo screening to take place at finite temperature. In Fig. 20(b) we show $T_K(Q_0, \mu)/T_K(Q_0, \mu = 0)$ as a function of μ for $Q_0 = 0.15$ and $Q_0 = 0.2$, which shows how T_K increases with $|\mu|$. Despite of their values, note that the curves exhibits very similar behavior. This is because a finite value of μ produces a rigid shift of the curves (not shown) enhancing the value of $\Gamma(0)$ due to more conduction electron's density of states at the Fermi level. The reader may have already anticipated this by noticing that the hybridization function is a smooth function of ω. It is worth mentioning that for $Q_0 = 0.1$ and $Q_0 = 0.05$ shown in Fig. 20(a), T_K becomes too small to be captured by our NRG flow which was truncated at a lower temperature $T_{\text{min}} = 10^{-12}$. We examine now, how the Kondo temperature changes with Q_0. To see this, in Fig. 20(c) we show $T_K(Q_0, \mu)$ vs $1/Q_0$ for several values of μ. Note that in the limit of large Q_0 (small $1/Q_0$) all curves tend to collapse onto a single function of Q_0 given by $T_K = A\text{Exp}(-B/Q_0^2)$, where A and B depend on the parameters of the system. This is because in this limit the density of states of the effective conduction band depends essentially on Q_0 and becomes $\rho_{\text{host}}(\omega) \sim Q_0^2$ even for finite values of μ (NADA, a), and the Kondo temperature approaches its "standard" form for usual metallic systems $T_K \sim \text{Exp}[-1/\rho(0)J_0]$ (HEWSON, 1993), where J_0 is the Kondo coupling of the equivalent effective low-energy Kondo model[3].

The situation is more compelling for $J > 1$, in which case the energy dependence of the hybridization function changes at $\omega = \pm Q_0$ (for $\mu = 0$) (NADA, a). Figure 21(a) shows how the hybridization function evolves with increasing Q_0 for $J = 2$ by fixing $\mu = 0$. Clearly, the hybridization function exhibits a plateau of width $2Q_0$, consistent with previous analytical calculations in Ref. (LÜ et al., 2019). Moreover, the height of the plateau increases with Q_0, which suggests that the Kondo temperature increases with Q_0, resembling the flat band Anderson model. This is important to understand the behavior of T_K in the regime of $Q_0 > |\mu|$. Indeed, this suggests that for $J = 2$ and for a fixed $Q_0 \neq 0$ the system will exhibit two distinct regimes observed in the behavior of T_K as a function of μ. To confirm this expectation, in Fig. 21(b) we show $T_K(Q_0, \mu)/T_K(Q_0, \mu = 0)$ as a function of $|\mu|/Q_0$ for several values of Q_0. One can clearly see that T_K have distinct behavior for $|\mu|/Q_0 < 1$ and $|\mu|/Q_0 > 1$. For $|\mu|/Q_0 < 1$ the Kondo temperature tends to collapse onto a single universal function of $|\mu|/Q_0$. On the other hand, for $|\mu|/Q_0 > 1$, the curves change their concavity and are far apart from each other. This reveals that the region $|\mu|/Q_0 < 1$ characterizes a regime dominated by Q_0 in which T_K should depend very weakly on μ as the hybridization function is nearly flat. This becomes more evident in Fig. 21(c) where we show $T_K(Q_0, \mu)$ vs $1/Q_0$ for various values of μ. These curves expose very clearly that indeed for $Q_0 > |\mu|$, T_K depends on Q_0 as $T_K = A\text{Exp}(-B/Q_0)$. Again, here A and B are quantities dependent on the other parameters of the model.

[3] An effective equivalent Kondo model could be obtained by performing a Schrieffer-Wolff transformation to a single impurity Anderson model with parameter equivalent to ours is some particular limit.

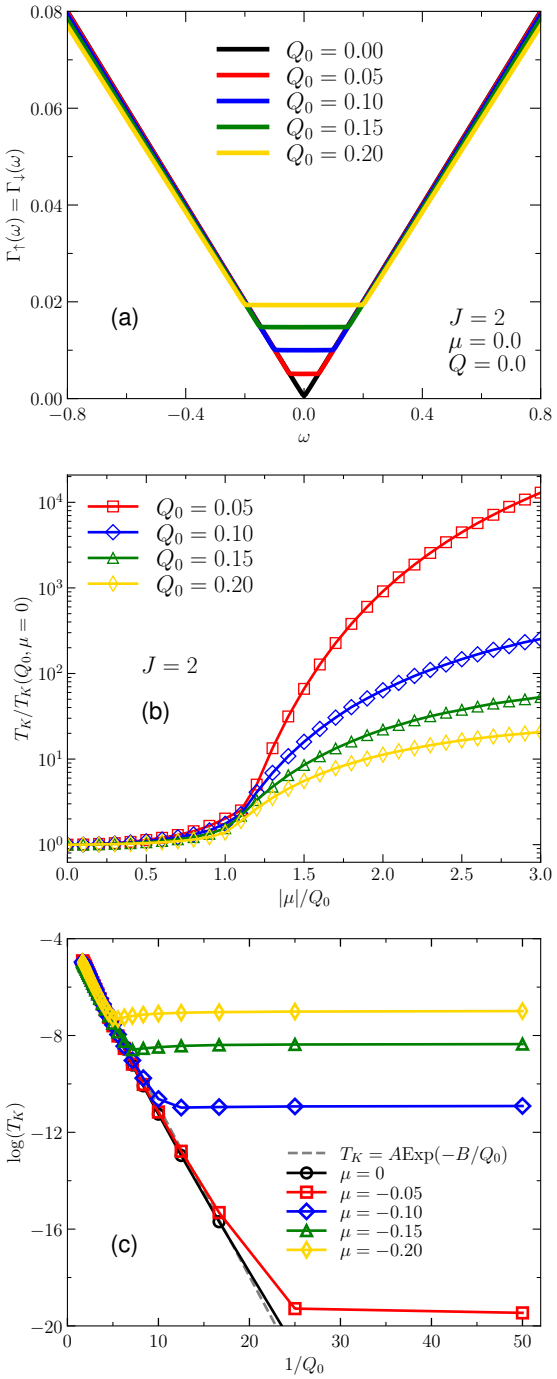

Figure 21 – (a) Hybridization function vs energy for $J = 2$ and various values of Q_0. (b) $T_K(Q_0, \mu)/T_K(Q_0, \mu = 0)$ as a function of μ/Q_0, for different values of Q_0. (c). Kondo temperature vs Q_0^{-1} for various values of μ. Here, $Q = 0$ for all panels.

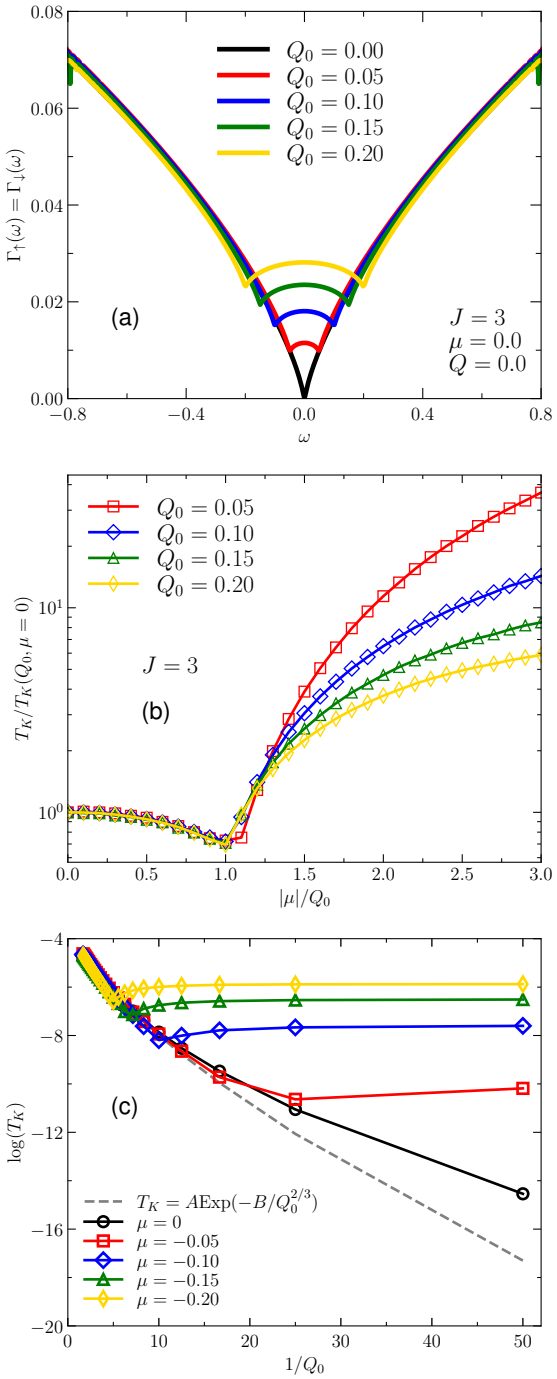

Figure 22 – (a) Hybridization function vs energy for $J = 3$ and various values of Q_0. (b) $T_K(Q_0, \mu)/T_K(Q_0, \mu = 0)$ as a function of μ/Q_0, for different values of Q_0. (c). Kondo temperature vs Q_0^{-1} for various values of μ. Here, $Q = 0$ for all panels.

Finally, we examine the Kondo regimes for triple WSM, $J = 3$. In Fig. 22 we show the same results as in Figs. 20 and 21 but for $J = 3$. First, note that we have again two very distinct regions in the energy axis. The flat plateau observed in the hybridization function shown in Fig. 21(a) is deformed into an arc within the region $|\omega| \leq Q_0$ in Fig. 22(a) with a maximum value at $\omega = 0$. The non monotonic behavior of $\Gamma(\omega)$ is reflected in the Kondo temperature of the system. Figure 22(b) shows $T_K(Q_0, \mu)/T_K(Q_0, \mu = 0)$ for various valued of Q_0. Similar to the case of $J = 2$, one can clearly distinguish two regimes separated by $|\mu| = Q_0$. Interestingly, note that the minimum of $\Gamma(\omega)$ observed at $\omega = \pm Q_0$ is accompanied by a minimum of T_K at $|\mu| = Q_0$, visible in the green and yellow curves. Moreover, it is remarkable that even in this case the curves collapse nicely onto each other $|\mu| < Q_0$, showing the universality of the Q_0 dominated regime.

From what we have seen above, the Kondo temperature for broken IS MWSMs behaves asymptotically as $T_K = A\text{Exp}(-B/Q_0^{2/J})$ for large Q_0 for all $J = 1, 2, 3$ [Figs. 20(c), 21(c), and 22(c)]. This behavior results from the shape of the effective hybridization function. Recalling that the Kondo temperature depends essentially on the structure of $\Gamma(\omega)$ at ω near the Fermi level and that $\Gamma(\omega) = \pi V^2 \rho_{\text{host}}(\omega)$, the behavior of T_K for $Q_0 \gtrsim \mu$ can be understood in light of the well-known Haldane formula for the Kondo temperature $T_K \sim \text{Exp}[-\pi U/8\Gamma(0)]$ (HALDANE, 1978), valid for a flat band SIAM in the particle-hole symmetric point. Keeping this in mind, we can see that $J = 2$ is a special case in which $\Gamma(\omega)$ becomes flat for $|\omega| \leq Q_0$ [Fig. 21(a)]. This is why the curves of Fig. 21(c) collapse more nicely onto the analytical result shown in the dashed line as compared to those of Fig. 20(c) and Fig. 22(c).

In conclusion, the breaking of IS in regimes $J > 1$ has a special motivation for this study and was not yet explored in literature. Not only these results brought us the conclusion that Kondo can emerge for these special cases even for $\mu = 0$, but this work also provided a contribution from the publication of Ref. (PEDROSA; SILVA; VERNEK, 2021) in collaboration with Dr. Joelson F. Silva.

7 Conclusion

We have studied the Kondo physics in a quantum magnetic impurity embedded in multi-Dirac(Weyl) node fermionic systems. Our numerical results reveal that the Kondo physics in the double- and triple-Dirac node systems always lies within known classes of pseudogap Kondo problem, well studied in the literature. While no Kondo screening is observed in the particle-hole symmetric case, in the asymmetric case for finite chemical potential, $\mu \neq 0$, the Kondo screening takes place due to finite hybridization function at the Fermi level. However, different scenarios appear in multi-Weyl node systems. (i) Breaking TRS (finite Q) is detrimental to Kondo at any finite chemical potential, but the Kondo peak is very slowly suppressed as $|Q|$ increases. This is because the spin polarization induced in the impurity is very tiny, as the polarization of the various conduction and valence band compensate each other, rendering a vanishingly small spin splitting in the hybridization function. (ii) When IS is broken we show that Kondo screening is present for any finite Q_0, meaning that the Kondo temperature is always finite. We find that the double- ($J = 2$) and triple- ($J = 3$) Weyl node fermionic systems are radically distinct from the single- ($J = 1$) Weyl node fermion systems. In contrast to the $J = 1$ case where μ is always an important parameter, for $J = 2$ and $J = 3$ we observe two distinct regimes: namely the regime $|\mu| > Q_0$, in which the Kondo temperature depends strongly on μ, and the regime $|\mu| < Q_0$, where T_K depends very weakly on the chemical potential. In particular, for $J = 2$ the system behaves almost as the traditional flat-band single impurity Anderson model. We believe our results expose distinct Kondo regimes present in multi-node Dirac and Weyl materials, contributing for future theoretical as well as experimental investigations in various Dirac/Weyl available materials.

In conclusion, our study comprehends the possibility of breaking TRS and IS through the manipulation of the model Hamiltonian which allows us to reproduce the well known results in the literature such as Kondo in Weyl and Dirac systems. Not only, but the Hamiltonian also allows us to study the topological physics of these systems trough manipulation of parameter J, showing that topology and pseudogap Kondo are intimately related for these materials when $J > 1$. When we protect the symmetries, PH asymmetry must be present in order for Kondo to emerge, however when IS is broken it is not necessary.

For future works, we want to explore different methods of calculating the numerical integrals of $\Gamma(\omega)$ in Eq.4.14 in $\mathbf{k}$ eliminating the usage of k_c.

Bibliography

It has been found in Ref. (LÜ et al., 2019) that the host density of states behaves as $\rho_{\text{host}}(\omega) \sim |(\omega+\mu)^2 + Q_0^2$ for $J = 1$ and and $\rho_{\text{host}}(\omega) \sim |\omega+\mu+Q_0|^{2/J} + |\omega+\mu-Q_0|^{2/J}$ for $J = 2, 3$. Citado na página 81.

AFFLECK, I.; SIMON, P. Detecting the kondo screening cloud around a quantum dot. *Phys. Rev. Lett.*, American Physical Society, v. 86, p. 2854–2857, Mar 2001. Disponível em: <https://link.aps.org/doi/10.1103/PhysRevLett.86.2854>. Citado na página 41.

AKHMEROV, A. R. Topological quantum computation away from the ground state using majorana fermions. *Phys. Rev. B*, American Physical Society, v. 82, p. 020509, Jul 2010. Disponível em: <https://link.aps.org/doi/10.1103/PhysRevB.82.020509>. Citado na página 25.

ALEXANDRADINATA, A.; WANG, Z.; BERNEVIG, B. A. Topological insulators from group cohomology. *Phys. Rev. X*, American Physical Society, v. 6, p. 021008, Apr 2016. Disponível em: <https://link.aps.org/doi/10.1103/PhysRevX.6.021008>. Citado na página 22.

ALICEA, J. Majorana fermions in a tunable semiconductor device. *Phys. Rev. B*, American Physical Society, v. 81, p. 125318, Mar 2010. Disponível em: <https://link.aps.org/doi/10.1103/PhysRevB.81.125318>. Citado na página 25.

ANDERSON, C. D. The positive electron. *Phys. Rev.*, American Physical Society, v. 43, p. 491–494, Mar 1933. Disponível em: <https://link.aps.org/doi/10.1103/PhysRev.43.491>. Citado na página 27.

ANDERSON, P. W. Localized magnetic states in metals. *Phys. Rev.*, American Physical Society, v. 124, p. 41–53, Oct 1961. Disponível em: <https://link.aps.org/doi/10.1103/PhysRev.124.41>. Citado 3 vezes nas páginas 23, 41, and 42.

ANDERSON, P. W.; YUVAL, G.; HAMANN, D. R. Exact results in the kondo problem. ii. scaling theory, qualitatively correct solution, and some new results on one-dimensional classical statistical models. *Phys. Rev. B*, American Physical Society, v. 1, p. 4464–4473, Jun 1970. Disponível em: <https://link.aps.org/doi/10.1103/PhysRevB.1.4464>. Citado na página 41.

ANDO, Y. Topological insulator materials. *Journal of the Physical Society of Japan*, v. 82, n. 10, p. 102001, 2013. Citado na página 22.

ARMITAGE, N.; MELE, E.; VISHWANATH, A. Weyl and dirac semimetals in three dimensional solids. *Reviews of Modern Physics*, v. 90, 05 2017. Citado 2 vezes nas páginas 34 and 59.

ARMITAGE, N. P.; MELE, E. J.; VISHWANATH, A. Weyl and dirac semimetals in three-dimensional solids. *Rev. Mod. Phys.*, American Physical Society, v. 90, p. 015001, Jan 2018. Disponível em: <https://link.aps.org/doi/10.1103/RevModPhys.90.015001>. Citado na página 23.

BERA, S.; SAU, J. D.; ROY, B. Dirty weyl semimetals: Stability, phase transition, and quantum criticality. *Phys. Rev. B*, American Physical Society, v. 93, p. 201302(R), May 2016. Disponível em: <https://link.aps.org/doi/10.1103/PhysRevB.93.201302>. Citado na página 74.

BERGMANN, G. Quantitative calculation of the spatial extension of the kondo cloud. *Phys. Rev. B*, American Physical Society, v. 77, p. 104401, Mar 2008. Disponível em: <https://link.aps.org/doi/10.1103/PhysRevB.77.104401>. Citado na página 41.

BERNEVIG, B. *Topological Insulators and Topological Superconductors*. [S.l.]: Princeton University Press, 2013. ISBN 9781400846733. Citado na página 25.

BERNEVIG, B. A.; HUGHES, T. L. *Topological Insulators and Topological Superconductors*. Stu - student edition. Princeton University Press, 2013. ISBN 9780691151755. Disponível em: <http://www.jstor.org/stable/j.ctt19cc2gc>. Citado na página 22.

BERNEVIG, B. A.; HUGHES, T. L.; ZHANG, S.-C. Quantum Spin Hall Effect and Topological Phase Transition in HgTe Quantum Wells. *Science*, American Association for the Advancement of Science, v. 314, n. 5806, p. 1757–1761, 2006. ISSN 0036-8075. Disponível em: <https://science.sciencemag.org/content/314/5806/1757>. Citado na página 22.

BORISENKO, S. et al. Experimental realization of a three-dimensional dirac semimetal. *Phys. Rev. Lett.*, American Physical Society, v. 113, p. 027603, Jul 2014. Disponível em: <https://link.aps.org/doi/10.1103/PhysRevLett.113.027603>. Citado na página 22.

BRAVYI, S.; DIVINCENZO, D. P.; LOSS, D. Schrieffer–wolff transformation for quantum many-body systems. *Annals of Physics*, v. 326, n. 10, p. 2793–2826, 2011. ISSN 0003-4916. Disponível em: <https://www.sciencedirect.com/science/article/pii/S0003491611001059>. Citado na página 41.

BULLA, R.; COSTI, T. A.; PRUSCHKE, T. Numerical renormalization group method for quantum impurity systems. *Rev. Mod. Phys.*, American Physical Society, v. 80, p. 395–450, Apr 2008. Disponível em: <https://link.aps.org/doi/10.1103/RevModPhys.80.395>. Citado 7 vezes nas páginas 14, 23, 52, 53, 65, 67, and 68.

BULLA, R.; PRUSCHKE, T.; HEWSON, A. C. Anderson impurity in pseudo-gap Fermi systems. *Journal of Physics Condensed Matter*, v. 9, n. 47, p. 10463–10474, 1997. Citado na página 74.

BURKOV, A. A.; HOOK, M. D.; BALENTS, L. Topological nodal semimetals. *Phys. Rev. B*, American Physical Society, v. 84, p. 235126, Dec 2011. Disponível em: <https://link.aps.org/doi/10.1103/PhysRevB.84.235126>. Citado na página 22.

BÜSSER, C. A. et al. Numerical analysis of the spatial range of the kondo effect. *Phys. Rev. B*, American Physical Society, v. 81, p. 045111, Jan 2010. Disponível em: <https://link.aps.org/doi/10.1103/PhysRevB.81.045111>. Citado na página 41.

CHAN, C.-K. et al. Photocurrents in weyl semimetals. *Phys. Rev. B*, American Physical Society, v. 95, p. 041104, Jan 2017. Disponível em: <https://link.aps.org/doi/10.1103/PhysRevB.95.041104>. Citado na página 42.

CHEN, Y.; NAZAROV, Y. *Spintronics with a Weyl point in superconducting nanostructures*. 2020. Citado na página 25.

CHENG, M. et al. Phase boundaries of power-law anderson and kondo models: A poor man's scaling study. *Phys. Rev. B*, American Physical Society, v. 96, p. 045103, Jul 2017. Disponível em: <https://link.aps.org/doi/10.1103/PhysRevB.96.045103>. Citado 2 vezes nas páginas 74 and 75.

CRONENWETT, S. M.; OOSTERKAMP, T. H.; KOUWENHOVEN, L. P. A tunable kondo effect in quantum dots. *Science*, American Association for the Advancement of Science, v. 281, n. 5376, p. 540–544, 1998. ISSN 0036-8075. Disponível em: <https://science.sciencemag.org/content/281/5376/540>. Citado 3 vezes nas páginas 11, 42, and 43.

de Haas, W.; de Boer, J.; van dën Berg, G. The electrical resistance of gold, copper and lead at low temperatures. *Physica*, v. 1, n. 7, p. 1115–1124, 1934. ISSN 0031-8914. Disponível em: <https://www.sciencedirect.com/science/article/pii/S0031891434803102>. Citado na página 39.

DIRAC, P. A. M.; FOWLER, R. H. The quantum theory of the electron. *Proceedings of the Royal Society of London. Series A, Containing Papers of a Mathematical and Physical Character*, v. 117, n. 778, p. 610–624, 1928. Disponível em: <https://royalsocietypublishing.org/doi/abs/10.1098/rspa.1928.0023>. Citado na página 22.

EZAWA, M. Merging of momentum-space monopoles by controlling zeeman field: From cubic-dirac to triple-weyl fermion systems. *Phys. Rev. B*, American Physical Society, v. 96, p. 161202, Oct 2017. Disponível em: <https://link.aps.org/doi/10.1103/PhysRevB.96.161202>. Citado na página 46.

FANG, C. et al. Multi-weyl topological semimetals stabilized by point group symmetry. *Phys. Rev. Lett.*, v. 108, p. 266802, Jun 2012. Disponível em: <https://link.aps.org/doi/10.1103/PhysRevLett.108.266802>. Citado 5 vezes nas páginas 23, 46, 50, 51, and 74.

FRANCK, J.; MANCHESTER, F.; MARTIN, D. The specific heat of pure copper and of some dilute copper+iron alloys showing a minimum in the electrical resistance at low temperatures. *Proceedings of The Royal Society A: Mathematical, Physical and Engineering Sciences*, v. 263, p. 494–507, 10 1961. Citado 2 vezes nas páginas 11 and 40.

FRANZ, M. Race for majorana fermions. *Physics*, v. 3, 03 2010. Citado na página 25.

FRITZ, L.; FLORENS, S.; VOJTA, M. Universal crossovers and critical dynamics of quantum phase transitions: A renormalization group study of the pseudogap kondo problem. *Phys. Rev. B*, American Physical Society, v. 74, p. 144410, Oct 2006. Disponível em: <https://link.aps.org/doi/10.1103/PhysRevB.74.144410>. Citado 2 vezes nas páginas 44 and 74.

FRITZ, L.; VOJTA, M. Phase transitions in the pseudogap anderson and kondo models: Critical dimensions, renormalization group, and local-moment criticality. *Phys. Rev. B*, American Physical Society, v. 70, p. 214427, Dec 2004. Disponível em: <https://link.aps.org/doi/10.1103/PhysRevB.70.214427>. Citado na página 74.

FU, L.; KANE, C. L. Topological insulators with inversion symmetry. *Phys. Rev. B*, American Physical Society, v. 76, p. 045302, Jul 2007. Disponível em: <https://link.aps.org/doi/10.1103/PhysRevB.76.045302>. Citado 2 vezes nas páginas 22 and 24.

FU, L.; KANE, C. L.; MELE, E. J. Topological insulators in three dimensions. *Phys. Rev. Lett.*, American Physical Society, v. 98, p. 106803, Mar 2007. Disponível em: <https://link.aps.org/doi/10.1103/PhysRevLett.98.106803>. Citado na página 24.

GONZALEZ-BUXTON, C.; INGERSENT, K. Renormalization-group study of anderson and kondo impurities in gapless fermi systems. *Phys. Rev. B*, American Physical Society, v. 57, p. 14254–14293, Jun 1998. Disponível em: <https://link.aps.org/doi/10.1103/PhysRevB.57.14254>. Citado 3 vezes nas páginas 23, 65, and 74.

HALDANE, F. D. M. Scaling theory of the asymmetric anderson model. *Phys. Rev. Lett.*, American Physical Society, v. 40, p. 416–419, Feb 1978. Disponível em: <https://link.aps.org/doi/10.1103/PhysRevLett.40.416>. Citado na página 84.

HALDANE, F. D. M. Nonlinear field theory of large-spin heisenberg antiferromagnets: Semiclassically quantized solitons of the one-dimensional easy-axis néel state. *Phys. Rev. Lett.*, American Physical Society, v. 50, p. 1153–1156, Apr 1983. Disponível em: <https://link.aps.org/doi/10.1103/PhysRevLett.50.1153>. Citado na página 24.

HASAN, M. Z.; KANE, C. L. Colloquium: Topological insulators. *Rev. Mod. Phys.*, American Physical Society, v. 82, p. 3045–3067, Nov 2010. Disponível em: <https://link.aps.org/doi/10.1103/RevModPhys.82.3045>. Citado na página 22.

HE, L. P. et al. Quantum transport evidence for the three-dimensional dirac semimetal phase in cd_3as_2. *Phys. Rev. Lett.*, American Physical Society, v. 113, p. 246402, Dec 2014. Disponível em: <https://link.aps.org/doi/10.1103/PhysRevLett.113.246402>. Citado na página 22.

HE, T. et al. Structure, phase stability, half-metallicity, and fully spin-polarized weyl states in compound Nav_2o_4: An example for topological spintronic material. *Phys. Rev. Materials*, American Physical Society, v. 5, p. 024205, Feb 2021. Disponível em: <https://link.aps.org/doi/10.1103/PhysRevMaterials.5.024205>. Citado na página 25.

HEIDARI, S.; ASGARI, R. Chiral hall effect in strained weyl semimetals. *Phys. Rev. B*, American Physical Society, v. 101, p. 165309, Apr 2020. Disponível em: <https://link.aps.org/doi/10.1103/PhysRevB.101.165309>. Citado na página 23.

HEWSON, A. C. *The Kondo Problem to Heavy Fermions*. Cambridge, England: University Press, 1993. Citado 4 vezes nas páginas 23, 65, 74, and 81.

HOSUR, P.; PARAMESWARAN, S. A.; VISHWANATH, A. Charge transport in weyl semimetals. *Phys. Rev. Lett.*, American Physical Society, v. 108, p. 046602, Jan 2012. Disponível em: <https://link.aps.org/doi/10.1103/PhysRevLett.108.046602>. Citado na página 42.

HUANG, S.-M. et al. New type of weyl semimetal with quadratic double weyl fermions. *Proceedings of the National Academy of Sciences*, National Academy

of Sciences, v. 113, n. 5, p. 1180–1185, 2016. ISSN 0027-8424. Disponível em: <https://www.pnas.org/content/113/5/1180>. Citado 2 vezes nas páginas 23 and 46.

INGERSENT, K.; SI, Q. Critical local-moment fluctuations, anomalous exponents, and ω/t scaling in the kondo problem with a pseudogap. *Phys. Rev. Lett.*, American Physical Society, v. 89, p. 076403, Jul 2002. Disponível em: <https://link.aps.org/doi/10.1103/PhysRevLett.89.076403>. Citado na página 74.

JIA, S.; XU, S.-Y.; HASAN, M. Z. Weyl semimetals, fermi arcs and chiral anomalies. *Nature Materials*, v. 15, p. 1140–1144, 10 2016. Citado na página 45.

JIAN, S.-K.; YAO, H. Correlated double-weyl semimetals with coulomb interactions: Possible applications to $hgcr_2se_4$ and $srsi_2$. *Phys. Rev. B*, American Physical Society, v. 92, p. 045121, Jul 2015. Disponível em: <https://link.aps.org/doi/10.1103/PhysRevB.92.045121>. Citado na página 33.

J.THOULESS, D. Topological quantum numbers in nonrelativistic physics. *International Journal of Modern Physics B*, v. 11, 01 2012. Citado na página 50.

KAISER, D. Physics and feynman's diagrams. *American Scientist*, v. 93, p. 156–165, 03 2005. Citado na página 41.

KANE, C. L.; MELE, E. J. Quantum spin hall effect in graphene. *Phys. Rev. Lett.*, American Physical Society, v. 95, p. 226801, Nov 2005. Disponível em: <https://link.aps.org/doi/10.1103/PhysRevLett.95.226801>. Citado na página 22.

KOLLER, W.; HEWSON, A. C.; MEYER, D. Singular dynamics of underscreened magnetic impurity models. *Phys. Rev. B*, American Physical Society, v. 72, p. 045117, Jul 2005. Disponível em: <https://link.aps.org/doi/10.1103/PhysRevB.72.045117>. Citado na página 74.

KONDO, J. Resistance Minimum in Dilute Magnetic Alloys. *Progress of Theoretical Physics*, v. 32, n. 1, p. 37–49, 07 1964. ISSN 0033-068X. Disponível em: <https://doi.org/10.1143/PTP.32.37>. Citado na página 26.

KONDO, J. Resistance minimum in dilute magnetic alloys. *Progress of Theoretical Physics - PROG THEOR PHYS KYOTO*, v. 32, p. 37–49, 07 1964. Citado na página 39.

KÖNIG, M. et al. Quantum spin hall insulator state in hgte quantum wells. *Science*, American Association for the Advancement of Science, v. 318, n. 5851, p. 766–770, 2007. ISSN 0036-8075. Disponível em: <https://science.sciencemag.org/content/318/5851/766>. Citado na página 22.

KOSTERLITZ, J.; THOULESS, D. Long range order and metastability in two dimensional solids and superfluids. (application of dislocation theory). *Journal of Physics C: Solid State Physics*, v. 5, p. L124, 03 2001. Citado na página 24.

KRISHNA-MURTHY, H. R.; WILKINS, J. W.; WILSON, K. G. Renormalization-group approach to the anderson model of dilute magnetic alloys. i. static properties for the symmetric case. *Phys. Rev. B*, American Physical Society, v. 21, p. 1003–1043, Feb 1980. Disponível em: <https://link.aps.org/doi/10.1103/PhysRevB.21.1003>. Citado na página 76.

KRULL, C. *Electronic Structure of Metal Phthalocyanines on Ag(100)*. [S.l.]: Springer, Cham, 2014. ISBN 978-3-319-02659-6. Citado 2 vezes nas páginas 11 and 40.

KUNDU, A. et al. Magnetotransport of weyl semimetals with tilted dirac cones. *New Journal of Physics*, IOP Publishing, v. 22, n. 8, p. 083081, aug 2020. Disponível em: <https://doi.org/10.1088%2F1367-2630%2Faba98d>. Citado na página 23.

KUREBAYASHI, D.; NOMURA, K. Voltage-driven magnetization switching and spin pumping in weyl semimetals. *Phys. Rev. Applied*, American Physical Society, v. 6, p. 044013, Oct 2016. Disponível em: <https://link.aps.org/doi/10.1103/PhysRevApplied.6.044013>. Citado na página 25.

LAFLAMME, C. et al. Hybrid topological quantum computation with majorana fermions: A cold-atom setup. *Phys. Rev. A*, American Physical Society, v. 89, p. 022319, Feb 2014. Disponível em: <https://link.aps.org/doi/10.1103/PhysRevA.89.022319>. Citado na página 25.

LANDSTEINER, K. Anomalous transport of weyl fermions in weyl semimetals. *Phys. Rev. B*, American Physical Society, v. 89, p. 075124, Feb 2014. Disponível em: <https://link.aps.org/doi/10.1103/PhysRevB.89.075124>. Citado na página 33.

LEE, E. J. H. et al. Zero-bias anomaly in a nanowire quantum dot coupled to superconductors. *Phys. Rev. Lett.*, American Physical Society, v. 109, p. 186802, Oct 2012. Disponível em: <https://link.aps.org/doi/10.1103/PhysRevLett.109.186802>. Citado na página 25.

LI, F. et al. Weyl points and fermi arcs in a chiral phononic crystal. *Nature Physics*, v. 14, 01 2018. Citado na página 45.

LI, G.-Y. et al. Ferromagnetism-induced kondo effect in graphene with a magnetic impurity. *Phys. Rev. B*, American Physical Society, v. 100, p. 115115, Sep 2019. Disponível em: <https://link.aps.org/doi/10.1103/PhysRevB.100.115115>. Citado 2 vezes nas páginas 73 and 78.

LI, P. et al. Spin-momentum locking and spin-orbit torques in magnetic nano-heterojunctions composed of weyl semimetal wte2. *Nature Communications*, v. 9, 09 2018. Citado na página 25.

LIANG, S. et al. Experimental tests of the chiral anomaly magnetoresistance in the dirac-weyl semimetals na_3Bi and gdptbi. *Phys. Rev. X*, American Physical Society, v. 8, p. 031002, Jul 2018. Disponível em: <https://link.aps.org/doi/10.1103/PhysRevX.8.031002>. Citado na página 33.

LIU, Q.; ZUNGER, A. Predicted realization of cubic dirac fermion in quasi-one-dimensional transition-metal monochalcogenides. *Phys. Rev. X*, American Physical Society, v. 7, p. 021019, May 2017. Disponível em: <https://link.aps.org/doi/10.1103/PhysRevX.7.021019>. Citado 2 vezes nas páginas 23 and 46.

LIU, Z. K. et al. Discovery of a three-dimensional topological dirac semimetal, na3bi. *Science*, American Association for the Advancement of Science, v. 343, n. 6173, p. 864–867, 2014. ISSN 0036-8075. Disponível em: <https://science.sciencemag.org/content/343/6173/864>. Citado na página 22.

LOGAN, D. E.; TUCKER, A. P.; GALPIN, M. R. Common non-fermi liquid phases in quantum impurity physics. *Phys. Rev. B*, American Physical Society, v. 90, p. 075150, Aug 2014. Disponível em: <https://link.aps.org/doi/10.1103/PhysRevB.90.075150>. Citado na página 23.

LOPEZ, J. C.; TORRES, L. E. F. F.; NUNEZ, A. S. Multiterminal conductance at the surface of a weyl semimetal. *Phys. Rev. B*, American Physical Society, v. 97, p. 125419, Mar 2018. Disponível em: <https://link.aps.org/doi/10.1103/PhysRevB.97.125419>. Citado na página 23.

LÜ, H.-F. et al. Quantum impurity in topological multi-weyl semimetals. *Phys. Rev. B*, American Physical Society, v. 99, p. 115109, Mar 2019. Disponível em: <https://link.aps.org/doi/10.1103/PhysRevB.99.115109>. Citado 8 vezes nas páginas 23, 25, 46, 50, 51, 79, 81, and 87.

LV, B. Q. et al. Experimental discovery of weyl semimetal taas. *Phys. Rev. X*, American Physical Society, v. 5, p. 031013, Jul 2015. Disponível em: <https://link.aps.org/doi/10.1103/PhysRevX.5.031013>. Citado na página 25.

MA, D. et al. Kondo effect with weyl semimetal fermi arcs. *Phys. Rev. B*, American Physical Society, v. 97, p. 045148, Jan 2018. Disponível em: <https://link.aps.org/doi/10.1103/PhysRevB.97.045148>. Citado na página 26.

MAJORANA, E. Teoria simmetrica dell'elettrone e del positrone. *Il Nuovo Cimento*, v. 14, p. 171–184, 01 1937. Citado na página 25.

MITCHELL, A. K.; FRITZ, L. Kondo effect in three-dimensional dirac and weyl systems. *Phys. Rev. B*, American Physical Society, v. 92, p. 121109, Sep 2015. Disponível em: <https://link.aps.org/doi/10.1103/PhysRevB.92.121109>. Citado 5 vezes nas páginas 11, 26, 46, 48, and 49.

MITCHELL, A. K.; FRITZ, L. Kondo effect in three-dimensional dirac and weyl systems. *Physical Review B*, v. 92, p. 121109(R), 09 2015. Citado 3 vezes nas páginas 23, 44, and 74.

MITCHELL, A. K. et al. Quantum phase transitions and thermodynamics of the power-law kondo model. *Phys. Rev. B*, American Physical Society, v. 88, p. 195119, Nov 2013. Disponível em: <https://link.aps.org/doi/10.1103/PhysRevB.88.195119>. Citado na página 74.

MOORE, J. The birth of topological insulators. *Nature*, v. 464, p. 194–8, 03 2010. Citado na página 24.

MOORE, J. E. The birth of topological insulators. *Nature*, v. 464, n. 7286, p. 194–198, 2010. ISSN 0028-0836. Citado na página 22.

NANDY, S. et al. Chiral anomaly as the origin of the planar hall effect in weyl semimetals. *Phys. Rev. Lett.*, American Physical Society, v. 119, p. 176804, Oct 2017. Disponível em: <https://link.aps.org/doi/10.1103/PhysRevLett.119.176804>. Citado na página 23.

NAYAK, C. et al. Non-abelian anyons and topological quantum computation. *Rev. Mod. Phys.*, American Physical Society, v. 80, p. 1083–1159, Sep 2008. Disponível em: <https://link.aps.org/doi/10.1103/RevModPhys.80.1083>. Citado na página 25.

NOLTING, W.; BREWER, W. *Fundamentals of Many-body Physics*. [S.l.]: Springer-Verlag Berlin Heidelberg, 2009. 602/607 p. ISBN 978-3-540-71930-4. Citado na página 52.

OJANEN, T. Helical fermi arcs and surface states in time-reversal invariant weyl semimetals. *Phys. Rev. B*, American Physical Society, v. 87, p. 245112, Jun 2013. Disponível em: <https://link.aps.org/doi/10.1103/PhysRevB.87.245112>. Citado na página 23.

OREG, Y.; REFAEL, G.; OPPEN, F. von. Helical liquids and majorana bound states in quantum wires. *Phys. Rev. Lett.*, American Physical Society, v. 105, p. 177002, Oct 2010. Disponível em: <https://link.aps.org/doi/10.1103/PhysRevLett.105.177002>. Citado na página 25.

PACHOS, J.; SIMON, S. Focus on topological quantum computation. *New Journal of Physics*, v. 16, p. 065003, 06 2014. Citado na página 25.

PARK, J. et al. How to directly measure a kondo cloud's length. *Phys. Rev. Lett.*, American Physical Society, v. 110, p. 246603, Jun 2013. Disponível em: <https://link.aps.org/doi/10.1103/PhysRevLett.110.246603>. Citado na página 41.

PEDROSA, G. T. D.; SILVA, J. F.; VERNEK, E. Kondo screening regimes in multi-dirac and weyl systems. *Phys. Rev. B*, American Physical Society, v. 103, p. 045137, Jan 2021. Disponível em: <https://link.aps.org/doi/10.1103/PhysRevB.103.045137>. Citado 2 vezes nas páginas 26 and 84.

PRINCIPI, A.; VIGNALE, G.; ROSSI, E. Kondo effect and non-fermi-liquid behavior in dirac and weyl semimetals. *Phys. Rev. B*, American Physical Society, v. 92, p. 041107, Jul 2015. Disponível em: <https://link.aps.org/doi/10.1103/PhysRevB.92.041107>. Citado 2 vezes nas páginas 23 and 26.

QI, X.-L.; ZHANG, S.-C. Topological insulators and superconductors. *Rev. Mod. Phys.*, American Physical Society, v. 83, p. 1057–1110, Oct 2011. Disponível em: <https://link.aps.org/doi/10.1103/RevModPhys.83.1057>. Citado 2 vezes nas páginas 22 and 24.

RAO, Z. et al. Observation of unconventional chiral fermions with long fermi arcs in cosi. *Nature*, v. 567, p. 1, 03 2019. Citado na página 45.

READ, N.; GREEN, D. Paired states of fermions in two dimensions with breaking of parity and time-reversal symmetries and the fractional quantum hall effect. *Phys. Rev. B*, American Physical Society, v. 61, p. 10267–10297, Apr 2000. Disponível em: <https://link.aps.org/doi/10.1103/PhysRevB.61.10267>. Citado na página 25.

ROY, B.; GOSWAMI, P.; JURIČ, V. Interacting weyl fermions: Phases, phase transitions, and global phase diagram. *Phys. Rev. B*, American Physical Society, v. 95, p. 201102(R), May 2017. Disponível em: <https://link.aps.org/doi/10.1103/PhysRevB.95.201102>. Citado na página 74.

SARMA, S. D.; FREEDMAN, M.; NAYAK, C. Majorana zero modes and topological quantum computation. *npj Quantum Information*, v. 1, 01 2015. Citado na página 25.

SCHNYDER, A. P. et al. Classification of topological insulators and superconductors in three spatial dimensions. *Phys. Rev. B*, American Physical Society, v. 78, p. 195125, Nov 2008. Disponível em: <https://link.aps.org/doi/10.1103/PhysRevB.78.195125>. Citado na página 24.

SCHRIEFFER, J. R.; WOLFF, P. A. Relation between the anderson and kondo hamiltonians. *Phys. Rev.*, American Physical Society, v. 149, p. 491–492, Sep 1966. Disponível em: <https://link.aps.org/doi/10.1103/PhysRev.149.491>. Citado na página 41.

SILVA, L. G. G. V. Dias da et al. Conductance and kondo interference beyond proportional coupling. *Phys. Rev. Lett.*, American Physical Society, v. 119, p. 116801, Sep 2017. Disponível em: <https://link.aps.org/doi/10.1103/PhysRevLett.119.116801>. Citado na página 23.

SILVA, L. G. G. V. Dias da et al. Zero-field kondo splitting and quantum-critical transition in double quantum dots. *Phys. Rev. Lett.*, American Physical Society, v. 97, p. 096603, Aug 2006. Disponível em: <https://link.aps.org/doi/10.1103/PhysRevLett.97.096603>. Citado na página 23.

ŠMEJKAL, L.; JUNGWIRTH, T. s.; SINOVA, J. Route towards dirac and weyl antiferromagnetic spintronics. *physica status solidi (RRL) – Rapid Research Letters*, v. 11, n. 4, p. 1700044, 2017. Disponível em: <https://onlinelibrary.wiley.com/doi/abs/10.1002/pssr.201700044>. Citado 2 vezes nas páginas 25 and 33.

SUN, Y. et al. Strong intrinsic spin hall effect in the taas family of weyl semimetals. *Phys. Rev. Lett.*, American Physical Society, v. 117, p. 146403, Sep 2016. Disponível em: <https://link.aps.org/doi/10.1103/PhysRevLett.117.146403>. Citado na página 25.

SUSHKOV, A. B. et al. Optical evidence for a weyl semimetal state in pyrochlore $eu_2ir_2o_7$. *Phys. Rev. B*, American Physical Society, v. 92, p. 241108, Dec 2015. Disponível em: <https://link.aps.org/doi/10.1103/PhysRevB.92.241108>. Citado na página 33.

THOULESS, D. J. et al. Quantized hall conductance in a two-dimensional periodic potential. *Phys. Rev. Lett.*, American Physical Society, v. 49, p. 405–408, Aug 1982. Disponível em: <https://link.aps.org/doi/10.1103/PhysRevLett.49.405>. Citado na página 24.

TIMUSK, T.; STATT, B. The pseudogap in high-temperature superconductors: an experimental survey. *Reports on Progress in Physics*, v. 62, p. 61–122, 1999. Citado na página 44.

TOKURA, Y.; YASUDA, K.; TSUKAZAKI, A. Magnetic topological insulators. *Nature Reviews Physics*, v. 1, 01 2019. Citado na página 24.

VOJTA, M.; FRITZ, L. Upper critical dimension in a quantum impurity model: Critical theory of the asymmetric pseudogap kondo problem. *Phys. Rev. B*, American Physical Society, v. 70, p. 094502, Sep 2004. Disponível em: <https://link.aps.org/doi/10.1103/PhysRevB.70.094502>. Citado na página 44.

VOJTA, M.; FRITZ, L.; BULLA, R. Gate-controlled kondo screening in graphene: Quantum criticality and electron-hole asymmetry. *EPL (Europhysics Letters)*, IOP

Publishing, v. 90, n. 2, p. 27006, apr 2010. Disponível em: <https://doi.org/10.1209%2F0295-5075%2F90%2F27006>. Citado na página 74.

WAN, X. et al. Topological semimetal and fermi-arc surface states in the electronic structure of pyrochlore iridates. *Phys. Rev. B*, American Physical Society, v. 83, p. 205101, May 2011. Disponível em: <https://link.aps.org/doi/10.1103/PhysRevB.83.205101>. Citado 2 vezes nas páginas 23 and 45.

WANG, J.-R.; LIU, G.-Z.; ZHANG, C.-J. Topological quantum critical point in a triple-weyl semimetal: Non-fermi-liquid behavior and instabilities. *Phys. Rev. B*, American Physical Society, v. 99, p. 195119, May 2019. Disponível em: <https://link.aps.org/doi/10.1103/PhysRevB.99.195119>. Citado na página 46.

WENG, H. et al. Weyl semimetal phase in noncentrosymmetric transition-metal monophosphides. *Phys. Rev. X*, American Physical Society, v. 5, p. 011029, Mar 2015. Disponível em: <https://link.aps.org/doi/10.1103/PhysRevX.5.011029>. Citado na página 25.

WEYL, H. Elektron und gravitation. i. *Z. Phys.*, v. 56, p. 330–352, 01 1929. Citado 4 vezes nas páginas 33, 34, 35, and 37.

WITHOFF, D.; FRADKIN, E. Phase transitions in gapless fermi systems with magnetic impurities. *Phys. Rev. Lett.*, American Physical Society, v. 64, p. 1835–1838, Apr 1990. Disponível em: <https://link.aps.org/doi/10.1103/PhysRevLett.64.1835>. Citado na página 74.

WU, C.-H. Electronic properties of the dirac and weyl systems with first- and higher-order dispersion in non-fermi-liquid picture. *Physics Letters A*, v. 383, n. 31, p. 125876, 2019. ISSN 0375-9601. Disponível em: <http://www.sciencedirect.com/science/article/pii/S0375960119306954>. Citado na página 73.

XIA, Y. et al. Observation of a large-gap topological-insulator class with a single Dirac cone on the surface. *Nature Physics*, Nature Publishing Group, v. 5, n. 6, p. 398–402, 2009. ISSN 17452481. Citado na página 22.

XIONG, J. et al. Evidence for the chiral anomaly in the dirac semimetal na3bi. *Science*, American Association for the Advancement of Science, 2015. ISSN 0036-8075. Disponível em: <https://science.sciencemag.org/content/early/2015/09/02/science.aac6089>. Citado na página 46.

XU, G. et al. Chern semimetal and the quantized anomalous hall effect in $hgcr_2se_4$. *Phys. Rev. Lett.*, American Physical Society, v. 107, p. 186806, Oct 2011. Disponível em: <https://link.aps.org/doi/10.1103/PhysRevLett.107.186806>. Citado 2 vezes nas páginas 23 and 46.

XU, S.-Y. et al. Discovery of a weyl fermion semimetal and topological fermi arcs. *Science*, American Association for the Advancement of Science, v. 349, n. 6248, p. 613–617, 2015. ISSN 0036-8075. Disponível em: <https://science.sciencemag.org/content/349/6248/613>. Citado 2 vezes nas páginas 23 and 25.

XU, S.-Y. et al. Discovery of a weyl fermion semimetal and topological fermi arcs. *Science (New York, N.Y.)*, v. 349, 07 2015. Citado na página 45.

YAN, B.; FELSER, C. Topological materials: Weyl semimetals. *Annual Review of Condensed Matter Physics*, v. 8, n. 1, p. 337–354, 2017. Disponível em: <https://doi.org/10.1146/annurev-conmatphys-031016-025458>. Citado na página 25.

YANAGISAWA, T. Kondo effect in Dirac systems. *Journal of the Physical Society of Japan*, v. 84, n. 7, p. 1–7, 2015. ISSN 13474073. Citado 2 vezes nas páginas 23 and 26.

YANG, B. J.; NAGAOSA, N. Classification of stable three-dimensional Dirac semimetals with nontrivial topology. *Nature Communications*, Nature Publishing Group, v. 5, 2014. ISSN 20411723. Citado 2 vezes nas páginas 23 and 73.

YANG, H. et al. Topological weyl semimetals in the chiral antiferromagnetic materials mn3ge and mn3sn. *New Journal of Physics*, IOP Publishing, v. 19, n. 1, p. 015008, jan 2017. Disponível em: <https://doi.org/10.1088/1367-2630/aa5487>. Citado na página 25.

YANG, K.-Y.; LU, Y.-M.; RAN, Y. Quantum hall effects in a weyl semimetal: Possible application in pyrochlore iridates. *Phys. Rev. B*, American Physical Society, v. 84, p. 075129, Aug 2011. Disponível em: <https://link.aps.org/doi/10.1103/PhysRevB.84.075129>. Citado na página 33.

YANG, S. A. Dirac and weyl materials: Fundamental aspects and some spintronics applications. *SPIN*, v. 06, n. 02, p. 1640003, 2016. Disponível em: <https://doi.org/10.1142/S2010324716400038>. Citado na página 25.

YOUNG, S. M. et al. Dirac semimetal in three dimensions. *Phys. Rev. Lett.*, American Physical Society, v. 108, p. 140405, Apr 2012. Disponível em: <https://link.aps.org/doi/10.1103/PhysRevLett.108.140405>. Citado na página 22.

YU, R. et al. Topological node-line semimetal and dirac semimetal state in antiperovskite cu_3PdN. *Phys. Rev. Lett.*, American Physical Society, v. 115, p. 036807, Jul 2015. Disponível em: <https://link.aps.org/doi/10.1103/PhysRevLett.115.036807>. Citado na página 73.

ZHAO, B. et al. Observation of charge to spin conversion in weyl semimetal wte_2 at room temperature. *Phys. Rev. Research*, American Physical Society, v. 2, p. 013286, Mar 2020. Disponível em: <https://link.aps.org/doi/10.1103/PhysRevResearch.2.013286>. Citado na página 25.

ZHONG, C. et al. Towards three-dimensional Weyl-surface semimetals in graphene networks. *Nanoscale*, Royal Society of Chemistry, v. 8, n. 13, p. 7232–7239, 2016. ISSN 20403372. Citado na página 23.

ŽITKO, R.; PRUSCHKE, T. Energy resolution and discretization artifacts in the numerical renormalization group. *Phys. Rev. B*, American Physical Society, v. 79, p. 085106, Feb 2009. Disponível em: <https://link.aps.org/doi/10.1103/PhysRevB.79.085106>. Citado 3 vezes nas páginas 65, 68, and 71.

A From Dirac to Weyl

This is the supplemental material to the text. Here you will find some calculus that were not included in the main text.

The following steps proves that quantum operators obey the same mathematical rules when they are submitted to matrix operations. So we have

$$\begin{aligned}
\hat{p}\times\hat{p} &= \begin{vmatrix} \hat{x} & \hat{y} & \hat{z} \\ p_x & p_y & p_z \\ p_x & p_y & p_z \end{vmatrix} = \\
&= (p_y p_z - p_z p_y)\hat{x} + (p_z p_x - p_x p_z)\hat{y} + (p_x p_y - p_y p_x)\hat{z} = \\
&= \left[\left(-i\hbar\frac{\partial}{\partial y}\right)\left(-i\hbar\frac{\partial}{\partial z}\right) - \left(-i\hbar\frac{\partial}{\partial z}\right)\left(-i\hbar\frac{\partial}{\partial y}\right)\right]\hat{x} + \\
&+ \left[\left(-i\hbar\frac{\partial}{\partial z}\right)\left(-i\hbar\frac{\partial}{\partial x}\right) - \left(-i\hbar\frac{\partial}{\partial x}\right)\left(-i\hbar\frac{\partial}{\partial z}\right)\right]\hat{y} + \\
&+ \left[\left(-i\hbar\frac{\partial}{\partial x}\right)\left(-i\hbar\frac{\partial}{\partial y}\right) - \left(-i\hbar\frac{\partial}{\partial y}\right)\left(-i\hbar\frac{\partial}{\partial x}\right)\right]\hat{z} = \\
&= -\hbar^2\left[\left(\cancel{\frac{\partial^2}{\partial y\partial z}} - \cancel{\frac{\partial^2}{\partial z\partial y}}\right)^{0}\hat{x} + \left(\cancel{\frac{\partial^2}{\partial z\partial x}} - \cancel{\frac{\partial^2}{\partial x\partial z}}\right)^{0}\hat{y} + \left(\cancel{\frac{\partial^2}{\partial x\partial y}} - \cancel{\frac{\partial^2}{\partial y\partial x}}\right)^{0}\hat{z}\right] = \\
&= -\hbar^2\left(0\hat{x} + 0\hat{y} + 0\hat{z}\right) = 0
\end{aligned} \tag{A.1}$$

we conclude, from basic vector property, that

$$\hat{p}\times\hat{p} = 0. \tag{A.2}$$

Another relation from vector products, is that if $\vec{u}\times\vec{v}$ for $\vec{u}=\vec{v}$, the outcome is always zero. In other words, vectors in the same direction has null vector product, leading to the following conclusion

$$\vec{A}\times\vec{A} = 0. \tag{A.3}$$

These statements might seem a little bit too obvious, but the obvious must be presented. We should remember that what may seem trivial for someone may not be so for someone else. We are talking about quantum operators, showing that they respect the classical operations is an important demonstration.

This next step is the demonstration of the product of two scalar products. This will be used to implement the minimum coupling in the Hamiltonian we are working to demonstrate Dirac's Equations.

Note the following relation between the products of vectors:

$$
\begin{aligned}
(\vec{\sigma}\cdot\vec{a})(\vec{\sigma}\cdot\vec{b}) = &= [(\sigma_x\hat{x}+\sigma_y\hat{y}+\sigma_z\hat{z})\cdot(a_x\hat{x}+a_y\hat{y}+a_z\hat{z})] \\
&\quad \cdot[(\sigma_x\hat{x}+\sigma_y\hat{y}+\sigma_z\hat{z})\cdot(b_x\hat{x}+b_y\hat{y}+b_z\hat{z})] \\
&= (\sigma_x a_x+\sigma_y a_y+\sigma_z a_z)(\sigma_x b_x+\sigma_y b_y+\sigma_z b_z) \\
&= \sigma_x\sigma_x a_x b_x+\sigma_x\sigma_y a_x b_y+\sigma_x\sigma_z a_x b_z \\
&+ \sigma_y\sigma_x a_y b_x+\sigma_y\sigma_y a_y b_y+\sigma_y\sigma_z a_y b_z+ \\
&+ \sigma_z\sigma_x a_z b_x+\sigma_z\sigma_y a_z b_y+\sigma_z\sigma_z a_z b_z \\
&= a_x b_x\hat{\mathbb{1}}+a_y b_y\hat{\mathbb{1}}+a_z b_z\hat{\mathbb{1}}+ \\
&+ (i\sigma_z)a_x b_y+(-i\sigma_y)a_x b_z+(-i\sigma_z)a_y b_x+ \\
&+ (i\sigma_x)a_y b_z+(i\sigma_y)a_z b_x+(-i\sigma_x)a_z b_y
\end{aligned}
\tag{A.4}
$$

where we rearranged the terms in the last relation and used the fact that equal Pauli matrices products results in identity matrices, as proven bellow:

$$
\sigma_x\sigma_x = \begin{pmatrix} 0 & 1 \\ 1 & 0 \end{pmatrix}\cdot\begin{pmatrix} 0 & 1 \\ 1 & 0 \end{pmatrix} = \begin{pmatrix} 1 & 0 \\ 0 & 1 \end{pmatrix} = \hat{\mathbb{1}} \tag{A.5}
$$

$$
\sigma_y\sigma_y = \begin{pmatrix} 0 & -i \\ i & 0 \end{pmatrix}\cdot\begin{pmatrix} 0 & -i \\ i & 0 \end{pmatrix} = \begin{pmatrix} 1 & 0 \\ 0 & 1 \end{pmatrix} = \hat{\mathbb{1}} \tag{A.6}
$$

$$
\sigma_z\sigma_z = \begin{pmatrix} 1 & 0 \\ 0 & -1 \end{pmatrix}\cdot\begin{pmatrix} 1 & 0 \\ 0 & -1 \end{pmatrix} = \begin{pmatrix} 1 & 0 \\ 0 & 1 \end{pmatrix} = \hat{\mathbb{1}} \tag{A.7}
$$

We conclude that $\sigma_i\sigma_j = i\epsilon_{ij}\sigma_k$, where ϵ_{ij} is the Levi-Civita Tensor, in this case a two dimensional tensor defined as

$$
\epsilon_{ij} = \begin{cases} +1 & \text{if } (i,j) = (x,y) \\ -1 & \text{if } (i,j) = (y,x) \\ 0 & \text{if } i = j \end{cases} \tag{A.8}
$$

Moreover, $\sigma_x\sigma_y = i\sigma_z$, $\sigma_y\sigma_x = -i\sigma_z$, $\sigma_x\sigma_z = -i\sigma_y$, $\sigma_z\sigma_x = i\sigma_y$, $\sigma_y\sigma_z = i\sigma_x$ and $\sigma_z\sigma_y = -i\sigma_x$. We use Eq. (A.4) to write these expressions as

$$
\begin{aligned}
(\vec{\sigma}\cdot\vec{a})(\vec{\sigma}\cdot\vec{b}) &= a_x b_x\hat{\mathbb{1}} + a_y b_y\hat{\mathbb{1}} + a_z b_z\hat{\mathbb{1}} + \\
&+ (i\sigma_z)a_x b_y + (-i\sigma_y)a_x b_z + (-i\sigma_z)a_y b_x + \\
&+ (i\sigma_x)a_y b_z + (i\sigma_y)a_z b_x + (-i\sigma_x)a_z b_y \\
&= a_x b_x\hat{\mathbb{1}} + a_y b_y\hat{\mathbb{1}} + a_z b_z\hat{\mathbb{1}} + \\
&+ i\sigma_z(a_x b_y - a_y b_x) + i\sigma_x(a_y b_z - a_z b_y) + i\sigma_y(a_z - a_x b_z) \\
&= (a_x b_x + a_y b_y + a_z b_z)\hat{\mathbb{1}} + \\
&+ i\sigma_z(a_x b_y - a_y b_x) + i\sigma_x(a_y b_z - a_z b_y) + i\sigma_y(a_z - a_x b_z) \\
&= (\vec{a}\cdot\vec{b})\hat{\mathbb{1}} + \\
&+ i\vec{\sigma}\cdot[(a_x b_y - a_y b_x)\hat{z}] + i\vec{\sigma}\cdot[(a_y b_z - a_z b_y)\hat{x}] + i\vec{\sigma}\cdot[(a_z b_x - a_x b_z)\hat{y}] \\
&= (\vec{a}\cdot\vec{b})\hat{\mathbb{1}} + \\
&+ i\vec{\sigma}\cdot[(a_y b_z - a_z b_y)\hat{x} + (a_z b_x - a_x b_z)\hat{y} + (a_x b_y - a_y b_x)\hat{z}] \\
&= (\vec{a}\cdot\vec{b})\hat{\mathbb{1}} + i\vec{\sigma}\cdot(\vec{a}\times\vec{b}). \qquad \text{(A.9)}
\end{aligned}
$$

We conclude that

$$(\vec{\sigma}\cdot\vec{a})(\vec{\sigma}\cdot\vec{b}) = (\vec{a}\cdot\vec{b})\hat{\mathbb{1}} + i\vec{\sigma}\cdot(\vec{a}\times\vec{b}). \qquad \text{(A.10)}$$

We show the anti-commutation relations between Dirac's Equation fourth dimensional tensors. The proof can be demonstrated as follows:

$$\{\gamma_\mu;\ \gamma_\nu\} = \gamma_\mu\gamma_\nu + \gamma_\nu\gamma_\mu. \qquad \text{(A.11)}$$

Proof,

If $\mu = \nu$, we have,

$$\begin{pmatrix} \mathbb{1} & 0 \\ 0 & -\mathbb{1} \end{pmatrix}\begin{pmatrix} \mathbb{1} & 0 \\ 0 & -\mathbb{1} \end{pmatrix} = \begin{pmatrix} \mathbb{1} & 0 \\ 0 & \mathbb{1} \end{pmatrix} = \mathbb{1}_{4\times4} \qquad \text{(A.12)}$$

$$\begin{pmatrix} 0 & -i\sigma_k \\ i\sigma_k & 0 \end{pmatrix}\begin{pmatrix} 0 & -i\sigma_k \\ i\sigma_k & 0 \end{pmatrix} = \begin{pmatrix} \sigma_k^2 & 0 \\ 0 & \sigma_k^2 \end{pmatrix} = \mathbb{1}_{4\times4} \qquad \text{(A.13)}$$

$$\begin{pmatrix} 0 & -i\sigma_k \\ i\sigma_k & 0 \end{pmatrix}\begin{pmatrix} 0 & -i\sigma_j \\ i\sigma_j & 0 \end{pmatrix} = \begin{pmatrix} \sigma_k\sigma_j & 0 \\ 0 & \sigma_k\sigma_j \end{pmatrix} \qquad \text{(A.14)}$$

$$\sigma_k\sigma_j + \sigma_j\sigma_k = 0, \qquad \forall\ k, j \mid k \neq j \qquad \text{(A.15)}$$

$$\sigma_k\sigma_j - \sigma_j\sigma_k = 0. \qquad \text{(A.16)}$$

Therefore, anti-commutation is given by,

$$\{\gamma_\mu,\ \gamma_\nu\} = \gamma_\mu\gamma_\nu + \gamma_\nu\gamma_\mu = 2\delta_{\mu\nu}. \qquad \text{(A.17)}$$